NORTHWESTERN UNIVERSITY

Deciding Under Duress: Motor Decisions of Larval Zebrafish Under Attack

A DISSERTATION

SUBMITTED TO THE GRADUATE SCHOOL
IN PARTIAL FULFILLMENT OF THE REQUIREMENTS

for the degree

DOCTOR OF PHILOSOPHY

Field of Biomedical Engineering

By

Kiran Bhattacharyya

EVANSTON, ILLINOIS

June 2019

ABSTRACT

Deciding Under Duress: Motor Decisions of Larval Zebrafish Under Attack

Kiran Bhattacharyya

We perform many movements every day without much deliberation. However, moving can be seen as a form of decision-making since one of many possible movements must be selected and executed. The decision-making processes that underlie movements are influenced by various factors, including sensory perception, energetics, time, perceived rates of failure along with uncertainty in the accuracy of sensory information and the movements themselves. The computations needed to evaluate these factors and make motor decisions are known to occur within the nervous system but the processes of movement selection and execution are still not well understood. Simpler organisms, such as fish at early developmental stages, are important model systems to investigate the neurobiology of motor decisions.

Specifically, the escape responses of larval fish can be mapped to a finite number of neurons that are identifiable under microscopy, allowing for an analysis of the neural substrate underlying the behavior. Moreover, selecting and executing the appropriate escape movement is critical for survival. Therefore, escape behaviors are simple models of decision-making where the biomechanics of locomotion and the associated neural circuitry are under

severe evolutionary pressure. This thesis investigates both the kinematics and the neurobiology of the movements made by larval zebrafish during escape behaviors initiated in response to real and simulated predators.

Through this work, I aim to answer four main questions about the evaluations and motor decisions relevant to the escape maneuvers of larval zebrafish:

(1) Do larval zebrafish perform a graded assessment of the threat posed by a predatory attack?

(2) How is the assessed threat used to make motor decisions about deploying specific escape movements or strategies as a response?

(3) What are the utilities of specific escape movements and their associated neural activations in producing maneuvers that successfully evade predators?

(4) Since escape behaviors must be optimally timed while being resistant to false negatives and false positives, how are the recruitment of escape circuits influenced by noise or uncertainty in sensory information?

By showing larval zebrafish visual stimuli of virtual predators approaching at different speeds, I interrogated how larval fish evaluate threat. Through these experiments, I found that the fish performed a graded assessment of threat and responded by deploying escape maneuvers with characteristic patterns of neural activation.

To understand the utility of specific escape maneuvers in producing successful evasive responses, I studied the escape responses of larval zebrafish from the attacks of a natural predator, the dragonfly nymph. By combining extensive analysis of the predator-prey interaction with computational methods, I found that the intersection of the reachable spaces of predator and prey plays a crucial role in determining escape success.

Lastly, I studied how noise in the visual percept of an approaching predator influenced the recruitment of escape circuits and the resulting escape behavior. Through a computational framework, I demonstrate that the sources of sensory noise and the methods of compensating for them may interact to serve functional roles in producing the resulting behavior.

Overall, these results draw a continuous thread through the sub-processes relevant to making escape decisions. The findings provide insight into sensory reception, sensory evaluation, neural recruitment, and movement generation in larval zebrafish under attack. While the four main questions presented above are an atomistic deconstruction of escape behavior, the investigation traverse scales of analysis—from the neural, to the organismal and the ecological.

Acknowledgments

I would like to acknowledge my advisor, Malcolm MacIver, who has been integral in my development as a scientist and researcher. I have always appreciated the breadth of his interests and his unique approach to research questions. Malcolm provided the combination of intellectual freedom and guidance that was right for me.

I would also like to acknowledge David McLean. Since the beginning I've also felt like a member of Dave's lab and have really benefited from his perspective. I've learned a lot from Dave's strong sense of narrative and design when presenting a scientific finding. Both Malcolm and Dave were very supportive of all my endeavors, including those beyond academia and research.

I would also like to thank Matthew Green, who I worked with very closely the first few years of my PhD. He introduced me to the details of working with larval zebrafish and developed the initial versions of techniques I expanded over the course of my doctoral work. Many thanks to the members of my PhD committee including Matt Tresch, Neelesh Patankar, and Todd Murphey. Their feedback was greatly appreciated.

Of course, I must thank the members of the MacIver lab. Specifically, Izaak, Yang, Chen, Ugurcan, and Sandra with whom I lived the daily grind and celebrated research wins. I also must thank the members of the McLean Lab and will remember the McLean lab holiday parties fondly where we discussed many things not research related. Cindy, Sandeep, and Mike also provided plenty of guidance with larval zebrafish experiments.

In the interest of space, I will end by thanking all my friends and family without whom I would not have survived. I can't imagine how much harder it would've been if I had to do it alone.

Finally, I must thank all of the larval zebrafish.

Preface

The work contained in this thesis was supported by NSF Graduate Research Fellowship, NSF-IOS 1456830, and NIH R01-NS067299. Malcolm MacIver and David McLean provided guidance with experimental design, data analysis, data visualization, and manuscript revision. The remainder of the work, including hardware development, software development, data collection, data analysis, manuscript preperation, etc., were performed by the author of the thesis.

Chapter 2 was published in *Current Biology* as a research article. Chapter 3 contains a manuscript that is in the submission stage for publication. Chapter 4 contains a prepared manuscript that is ready for submission.

Table of Contents

List of Figures

CHAPTER 1

Introduction

1.1. Evolving to escape

The rise of predation among mobile animals may have been the central mechanism driving the Cambrian radiation—an event 540 million years ago when most major animal phyla appeared in the fossil record Sperling et al. (2013). This suggests that the selection pressure on predator-prey interactions has played a significant role in shaping the morphology, biomechanical performance, and neural circuitry of animals Sillar et al. (2016). Specifically for prey—for whom the cost of failure is death—the ability to execute the appropriate escape maneuver to a given attack is a vital determinant of fitness. Therefore, escape responses of animals can be studied to understand how severe selection pressure shaped the sensorimotor performance and neural execution of movements.

Historically, studies of escape behaviors were guided by the command-neuron hypothesis where the escape response was considered a fast, stereotyped behavior initiated by a single or small group of neurons Carew (2000). This is supported by the existence of large diameter command-like neurons in many animals devoted to producing the shortest latency escapes with the fastest speeds Tanouye and Wyman (1980); Will (1991); Libersat (1994); Edwards et al. (1999); Korn and Faber (2005). Recruitment of these giant neurons alone is generally sufficient to produce an escape maneuver Edwards et al. (1999); Korn and Faber (2005).

1.2. The Mauthner neuron

The Mauthner neuron (M-cell), found in mirror-symmetric pairs in the hindbrain of teleost fish, tadpoles and some adult anurans, is a widely known example of a giant command-like neuron which is involved in shortest latency escapes to hydrodynamic and tactile stimuli Gahtan and Baier (2004); Kohashi and Oda (2008). Each M-cell projects an axon to the contralateral side of the body down the length of the spinal cord while synapsing onto primary motoneurons and descending interneurons Fetcho (1991); Eaton et al. (2001). A single spike of the M-cell is able to rapidly and massively excite musculature on one side of the body which creates a forceful bend of the tail in fish and starts the escape maneuver Eaton et al. (1981) .

This initial bend orients the fish in a new heading direction and is followed by propulsive swimming Korn and Faber (2005); Nair et al. (2015). Unidirectional connections from the M-cell to other reticulospinal neurons suggests that M-cell activation constitutes the recruitment of an escape circuit in the hindbrain Neki et al. (2014). Studies have shown that the heading direction change initiated by an M-cell mediated escape response can be tuned through the parallel activation of other motor programs as well Eaton et al. (1988, 1991); Eaton and Emberley (1991). However, this tunable directionality may still be predictable since the tentacled snake is innately able to predict the trajectory of an escaping fish by using a feint, a hydrodynamic stimulus, to startle fish into it's approaching jaws Catania (2009, 2010).

1.3. Escape as a decision

The fast, short latency escape responses to behaviorally urgent stimuli may be sufficiently stereotyped to be predictable due to the biomechanical constraints on high accelerations and velocities Hitchcock et al. (2015). However, the hypothesis of protean defence, grounded in the occurrence of variable and non-stereotyped escapes observed across many animals in their natural environment, argues that a variable escape response diminishes a predator's ability to predict the position of the prey—conferring a selective advantage Driver and Humphries (1970). Moreover, animals with giant command-like neurons can also generate escape responses that do not require the recruitment of the giant neuron Eaton et al. (1984); Edwards et al. (1999); von Reyn et al. (2014). These escapes that are not mediated by the giant neuron tend to be more variable in timing and kinematics Edwards et al. (1999); Domenici et al. (2011a); Eaton and Emberley (1991); Gahtan and Baier (2004); von Reyn et al. (2014). Additionally, instead of moving in response to an attack, many animals are also known to freeze which may help evade detection or feign death subsequently causing the predator to lose interest Edut and Eilam (2004); Chelini et al. (2009); Herberholz and Marquart (2012); Misslin (2003).

Therefore, animals can deploy a variety of evasive strategies based on the context of the predator-prey interaction. This suggests that animals must determine whether, when, and how to perform an escape movement and if they should do so with or without giant neuron recruitment. However, it is unclear how these decisions are made and what the utility of a specific escape movement is in producing a successful evasive maneuver.

1.4. The larval zebrafish as a vertebrate model

In this thesis, I study the sensory evaluations and motor decisions relevant to the escape responses of larval zebrafish. Just 3 days after hatching, larval zebrafish are about 4 mm long and have a complex motor repertoire including goal-directed behaviors, like the ability to capture small prey and escape from predators Budick and O'Malley (2000). Both prey-capture and predator-evasion require complex sensorimotor transformations where the animal must perform either fine and graded movements to orient towards an appetitive stimulus Patterson et al. (2013); Trivedi and Bollmann (2013) or large and fast movements away from an aversive stimulus O'Malley et al. (1996). Additionally, the larval zebrafish is a vertebrate with brain regions and structures analogous to humans while having a nervous system with a similar number of neurons as Drosophila's (~100,000) Lieschke and Currie (2007); Ahrens et al. (2012). This combination of reduced complexity but conserved anatomy makes the larval zebrafish a powerful model animal.

The larval zebrafish has about 200 reticulospinal neurons which mediate all motor behaviors —including escape responses—and are identifiable under microscopy after retrograde labeling with dye Metcalfe et al. (1986); Gahtan and O'Malley (2003); Orger et al. (2008). There is evidence of functional modularity in the reticulopsinal neurons and other descending neurons of larval zebrafish since specific nuclei have been implicated in producing turns or steering as opposed to propulsive swimming Orger et al. (2008); Huang et al. (2013); Severi et al. (2014); Wang and McLean (2014). Moreover, previous *in vivo* calcium imaging of neural activity indicates that a subset of these brainstem neurons, including the M-cell, tend to be active during the escape response Liu and Fetcho (1999); Gahtan et al. (2002). While the role of the M-cell in the escape maneuver has been studied, it is not clear how the activity of the other reticulospinal cells correlate to each other or contribute to the kinematics of the escape response.

Studies have shown that fast and slow swimming movements of the larval zebrafish are mediated by different subsets of spinal interneurons and motoneurons McLean et al. (2008); McLean and Fetcho (2009); Kishore et al. (2014). Moreover, others have shown that even different types of muscles are recruited for different swimming speeds in larval zebrafish Buss and Drapeau (2002). These functional groups in the reticulospinal neurons, spinal neurons, and even the musculature of larval zebrafish have implications about the neural substrate underlying the selection and execution of different escape movements and strategies.

1.5. Contribution

Here, I investigate how larval zebrafish evaluate the threat posed by an attacking predator in order to make escape decisions. I demonstrate how escape timing, direction, speed and the recruitment of the M-cell depend upon parameters of the predatory attack. Furthermore, I analyze the escape responses of larval zebrafish from the attacks of a natural predator to understand how specific escape movements and recruitment of the M-cell contributes to survival. Using these results, I propose a computational approach that can estimate the utility of specific movements in predator-prey interactions. Finally, to better understand the role of uncertainty in escape decisions, I look at how recruitment of the M-cell may be influenced by noise in the sensory percept of the threat.

In the Chapter 2, I show larval zebrafish visual stimuli of virtual predators approaching at different speeds while simultaneously monitoring the escape behavior of larval fish and the recruitment of neurons in their hindbrain. Through innovative high-speed volumetric neural activity imaging techniques in conjunction with behavioral experiments, I demonstrate that larval zebrafish perform a graded assessment of threat for different predator approach rates. The results demonstrate how larval fish stochastically deployed specific escape strategies requiring differential recruitment of the M-cell and other reticulospinal neurons as a function of the predator approach rate.

In Chapter 3, I study the escape maneuvers of larval zebrafish in response to attacks of dragonfly nymphs to assess the utility of specific escape maneuvers in producing successful evasive responses. An analysis of this interaction reveals that the intersection of the reachable spaces of the dragonfly nymph and the larval fish within the duration of the predatory strike is crucial in determining the likelihood of survival. Using this finding, I perform computational experiments to estimate the change in survival probability due to the changes in the reachable space of larval zebrafish from the recruitment of the M-cell.

In Chapter 4, I study how noise in the sensory percept of a threat influences the recruitment of escape circuits and the resulting escape behavior. I use computational methods to gain insight into how larval zebrafish may estimate relevant stimulus parameters from a sequence of noisy sensory data in real-time. By combining these findings with existing models of sensory processing and excitatory drive to motor circuits, I propose a mechanism that explains the variability in the timing of escape responses and the probabilistic recruitment of escape circuits in response to an approaching predator.

Collectively, the findings shed light on 1) how animals evaluate threat to deploy specific escape maneuvers that require characteristic patterns of neural recruitment, 2) how these escape movements and recruitment of circuits contribute to survival by shaping the reachable space of the animal and 3) how uncertainty in sensory information might influence neural recruitment and, subsequently, the escape behavior. More broadly, this thesis explores the mechanisms of sensory processing, movement selection and movement generation while investigating the selection pressure on that sensorimotor performance. All of these individual principles constitute different aspects of how motor decisions are made by the animal and shaped by its ecology. Not only do these principles apply to larval zebrafish but may extend to other vertebrates who share an underlying structural and functional patterning of the nervous system and axial morphology Kinkhabwala et al. (2011); Burke et al. (1995).

CHAPTER 2

Visual threat assessment and reticulospinal encoding of calibrated responses in larval zebrafish

2.1. Overview

All visual animals must decide whether approaching objects are a threat. Our current understanding of this process has identified a proximity-based mechanism where an evasive maneuver is triggered when a looming stimulus passes a subtended visual angle threshold. However, some escape strategies are more costly than others, and so it would be beneficial to additionally encode the level of threat conveyed by the predator's approach rate to select the most appropriate response. Here, using naturalistic rates of looming visual stimuli while simultaneously monitoring escape behavior and the recruitment of multiple reticulospinal neurons, we find that larval zebrafish do indeed perform a calibrated assessment of threat. While all fish generate evasive maneuvers at the same subtended visual angle, lower approach rates evoke slower, more kinematically variable escape responses with relatively long latencies as well as the unilateral recruitment of ventral spinal projecting nuclei (vSPNs) implicated in turning. In contrast, higher approach rates evoke faster, more kinematically stereotyped responses with relatively short latencies, as well as bilateral recruitment of vSPNs and unilateral recruitment of giant fiber neurons in fish and amphibians called Mauthner cells. In addition to the higher proportion of more costly, shorter-latency Mauthner-active responses to greater perceived threats, we observe a higher incidence of freezing behavior at higher approach rates. Our results provide a new framework to understand how behavioral flexibility is grounded in the appropriate balancing of trade-offs between fast and slow movements when deciding to respond to a visually perceived threat.

2.2. Introduction

When an animal perceives an oncoming predator, it is critical to correctly choose whether, when, and how to move to survive the impending attack. Looming visual stimuli, simulating an approaching predator, provide an opportunity to investigate the underlying mechanism of threat assessment involved in this set of decisions Fotowat and Gabbiani (2011); Card (2012). The current consensus across avariety of vertebrate and invertebrate organisms is that an approaching predator triggers a ballistic escape response once it reaches a certain subtended angle threshold Fotowat and Gabbiani (2007); Oliva et al. (2007); de Vries and Clandinin (2012); Yamamoto et al. (2003); Dunn et al. (2016).Given the constraints on predator size, this angle threshold is equivalent to a proximity threshold.

Within vertebrates, this theory of a proximity-based response aligns well with findings from a bilateral pair of giant fiber interneurons in the brainstem of fish, called Mauthner cells Medan and Preuss (2014); Korn and Faber (2005). Mauthner cells collect sensory information from one side of the body and transmit it to the other side via a large caliber axon Fetcho (1991); Faber et al. (1989), resulting in a strong contraction of body muscles opposite to the stimulus that generates a short-latency evasive turn. Mauthner cells respond to visual, tactile, vestibular, auditory, lateral-line and electric field stimuli Tabor et al. (2014); Zottoli (1977); Casagrand et al. (1999); Mirjany et al. (2011); Kohashi and Oda (2008); O'Malley et al. (1996); Eaton et al. (1981); Preuss et al. (2006); Chang et al. (1987) and are difficult to excite Nakayama and Oda (2004); Hatta and Korn (1998); Fukami et al. (1965); Furshpan and Furukawa (1962). The conclusion from these studies across various modalities is that the decision to escape is a result of reaching the Mauthner cell firing threshold due to strong sensory input, as would arise from an approaching predator that has traversed the proximity threshold.

However, with a proximity mechanism there is no way to distinguish between an object that passes the proximity threshold rapidly versus slowly, corresponding to threats of differing urgency. Moreover, while Mauthner cells expedite signal propagation and ensure quick reflexes, the power and relatively stereotyped reactions they produce can exact energetic costs and be exploited by predators Domenici et al. (2011a); Ydenberg and Dill (1986); Catania (2009). It would therefore be beneficial to encode speed of approach as an additional means to decide whether to engage the giant fiber escape systems or alternate, less costly strategies, such as no response or a less rapid, more flexible response. Currently it is unknown whether animals use approach rate to inform the trade-off between short-latency, ballistic movements and long-latency, more variable movements.

Here, we test the hypothesis that approach rate modulates escape behavior by using virtual looming stimuli with naturalistic sizes and approach rates, combined with high-speed kinematic analysis and in vivo calcium imaging of Mauthner cells, their homologs, and other reticulospinal nuclei in larval zebrafish. While zebrafish larvae did evade looming stimuli at a fixed subtended angle and distance, markedly different behaviors occurred as a function of approach rate. Lower approach rates were more likely to elicit a non-Mauthner, more kinematically variable escape response with longer latency. Surprisingly, evasive maneuvers were more reliably elicited by slowly approaching objects than by rapidly approaching objects, which we interpret as evidence of a freezing response to rapid predators. Even though fast approaches produced fewer evasive movements, these were much more likely to be Mauthner-active evasions. Between Mauthner-active and Mauthner-silent responses, we found a drop in recruitment probabilities of reticulospinal nuclei known to be involved in turning. However, specific changes in recruitment of MiD3, RoV3, MiV1, and MiR2 nuclei suggest circuit level differences in their involvement in generating the kinematics of these two distinct maneuvers. Critically, when Mauthners were recruited, escapes occurred with shorter latency than non-Mauthner escapes—regardless of approach rate—and were more stereotyped.

Collectively, our findings support a graded assessment of threat based on approach rate in addition to the previously described threshold based on the subtended angle of the approaching object. In this threat assessment logic, the approach rate (proportional to threat urgency) sets the probability of movement, its latency, speed, and variability, while the subtended angle threshold determines the timing of the movement. We discuss the implications of our findings for the neural processing of threat, how threat level is conveyed to the motor system, and the evolution of escape behavior.

2.3. Results

2.3.1. Timing and kinematics of looming evoked responses

Larval fish (3.5–5 mm, $N_{\text{fish}} = 21$) at 5–7 days post fertilization (dpf) were placed in a smaller dish within a larger dish (Fig. 2.1A) and shown looming stimuli projected onto diffusive paper around the edges of the larger dish. The virtual looming stimulus was a black square expanding on a blue background of stationary, low contrast rectangles Trivedi and Bollmann (2013) (Fig. 2.1B_2).

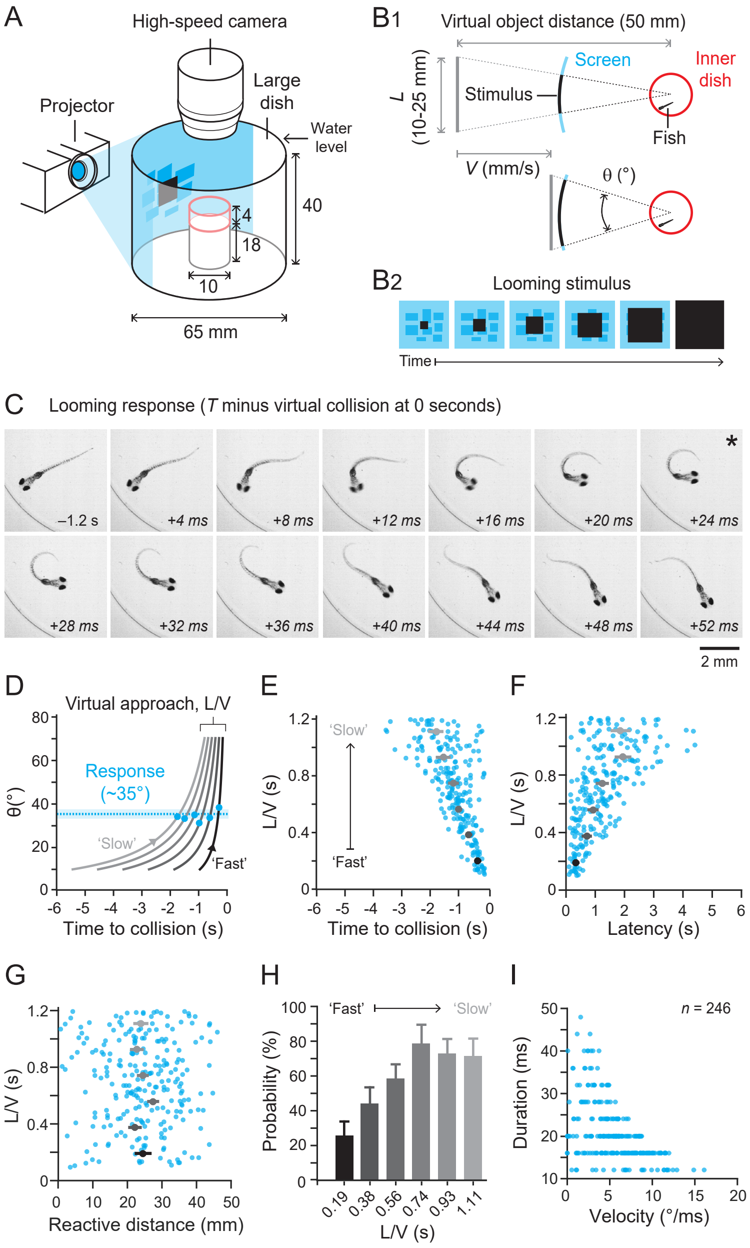

Figure 2.1. Timing and kinematics of looming evoked responses.

Figure 2.1 details: A) Larval zebrafish ($N_{\text{fish}} = 21$) were placed in a smaller dish (shown in red) within a larger dish and presented virtual looming stimuli projected onto the larger dish as shown. Responses were recorded with high speed videography at 250 fps from above. B_1) Virtual looming stimuli were defined by L, the size of the square, V, the velocity, and the apparent distance covered by the object (50 mm in this study). The time-varying subtended angle θ is determined by the parameter L/V. The azimuth of the stimulus with respect to the fish's head depends on the orientation of the fish, and therefore ranged from ±180°, with left being negative and right being positive. B_2) The stimulus was a black square expanding over time on a stationary blue background of low contrast rectangles. C) A representative looming evoked response with the time of response defined by time being negative before virtual collision at 0 seconds. This response is typical in that the largest directional change happened by the end of the initial bend—marked with asterisk—followed by undulatory swimming. D) Fish respond at a specific subtended angle of the looming object regardless of looming rate. By binning time of responses according to particular constant values of L/V, corresponding to specific curves of θ versus time, and marking the mean response time relative to time of virtual collision for each group (blue dots) we find that fish responded on average when $\theta = 35° \pm 15°$ (std, $N_{\text{trials}} = 246$). E) The average onset time of the looming evoked response increased with increasing L/V as found with other model animals, with larger L/Vs having more variable response times. F) The response latency from stimulus onset and the variability of the latency also increased with increasing L/V. G) The virtual distance from the looming stimulus at the time of fish response did not change with L/V. H) Fish ($N_{\text{fish}} = 21$) were more likely to respond to slow looming stimuli (higher L/Vs) than fast looming stimuli (low L/Vs). I) Fish manipulated both the duration of the initial bend and the yaw velocity of the initial bend to control the total head yaw achieved by the end of the initial bend. Horizontal bands are due to the 4 ms interval between video frames.

The looming stimulus (Fig. 2.1B) is defined by the size of the approaching object of equal width and height (L), the approach velocity (V), and the apparent distance covered (d), with the subtended angle θ to the snout being determined by these parameters (Fig. 2.1B_1).

The combined term L/V is an indicator of the expansion of θ with time and is used as a stimulus parameter as it allows comparison to looming-evoked responses in other animals quantified with the same parameter Card (2012); Oliva et al. (2007); Santer (2013). The L/V term was psuedorandomly selected with uniform probability between 0.1–1.2 seconds (s), since prior studies have shown this to be naturalistic Stewart et al. (2013). L was psuedorandomly selected with uniform probability between 10–25 mm (also naturalistic: Stewart et al. (2013)), with the apparent starting distance of the stimulus d held constant at 50 mm. The relative azimuthal angle of the stimulus depended on the freely swimming fish position, but varied between ±180° (left negative, right positive) and sampling was verified to be uniform (see Appendix A.1 for details).

High speed videography at 250 frames-per-second (fps) was used to record the looming-evoked response from above. Figure 2.1C depicts a representative looming evoked response to a looming stimulus with $L/V = 0.4$ s and azimuth 43°. The response starts at –1.2 s since time is negative before the virtual collision at 0 s. During the looming evoked response, the fish re-oriented with an initial bend (Fig. 2.1C, end of initial bend marked with asterisk) and swam away with undulatory swimming during a propulsive stage.

Figure 2.1D plots 6 curves of different expansions of θ with time which correspond to 6 different values of L/V. These 6 L/V values are the centers of 6 equally-spaced bins in the range of L/Vs tested (0.1–1.2 s) in this study (Bin 1: center $L/V = 0.19$ s, $\mathrm{N}_{\mathrm{trials}} = 29$, Bin 2: center $L/V = 0.38$ s, $\mathrm{N}_{\mathrm{trials}} = 34$, Bin 3: center $L/V = 0.56$ s, $\mathrm{N}_{\mathrm{trials}} = 45$, Bin 4: center $L/V = 0.74$ s, $\mathrm{N}_{\mathrm{trials}}\mathrm{n} = 49$, Bin 5: center $L/V = 0.93$ s, $\mathrm{N}_{\mathrm{trials}} = 44$, Bin 6: center $L/V = 1.11$ s, $\mathrm{N}_{\mathrm{trials}} = 44$,). The curve drawn with the darkest line represents the smallest L/V bin center—a fast looming stimulus—and the lightest curve represents the largest L/V bin center—a slow looming stimulus. When all of the responses are grouped into the 6 equally spaced bins and the average response time for each bin is plotted on the curves describing the expansion of θ with time, we found that the fish respond at approximately $\theta = 35°$ (Fig. 2.1E), for different values of L/V. The dashed line is the average θ (35° ± 15°, µ±std, $N_{\text{fish}} = 21$, $N_{\text{trials}} = 246$) at the time of response for all recorded responses for the continuum of L/Vs tested. The similarity between the population average and the average of each bin demonstrates that the average θ at the time of response deviated little for different L/Vs or looming rates, as has been recorded for looming evoked responses from other model animals Fotowat and Gabbiani (2007); Oliva et al. (2007); Card (2012); Santer (2013).

The existence of this critical subtended angle influenced both the timing of the fish response and the apparent distance from the virtual object when the fish responded. The length of time to collision from the onset of the fish's response increased with increasing L/V (Fig. 2.1E), also found to be true for larval zebrafish by other researchers Dunn et al. (2016); Temizer et al. (2015). The response latency increased with increasing L/V (Fig. 2.1F). However, the mean reactive distance—the apparent distance from the virtual object at the time of fish response—did not change with L/V, suggesting the existence of a critical reactive distance of ~25 mm.

While Fig. 2.1D and G indicate that the fish were performing looming evoked responses at some angular or distance threshold, Fig. 2.1H shows that fish were much more likely to respond to larger L/Vs—slow looming stimuli—than smaller ones—fast stimuli, demonstrating that response probability is modulated by the approach rate of the stimulus. When analyzing the kinematics of the initial bend, we found that fish used the duration of the initial bend and the head yaw velocity during the initial bend to produce different total changes in orientation for all of recorded responses (Fig. 2.1I, $N_{\text{fish}} = 21$, $N_{\text{trials}} = 246$).

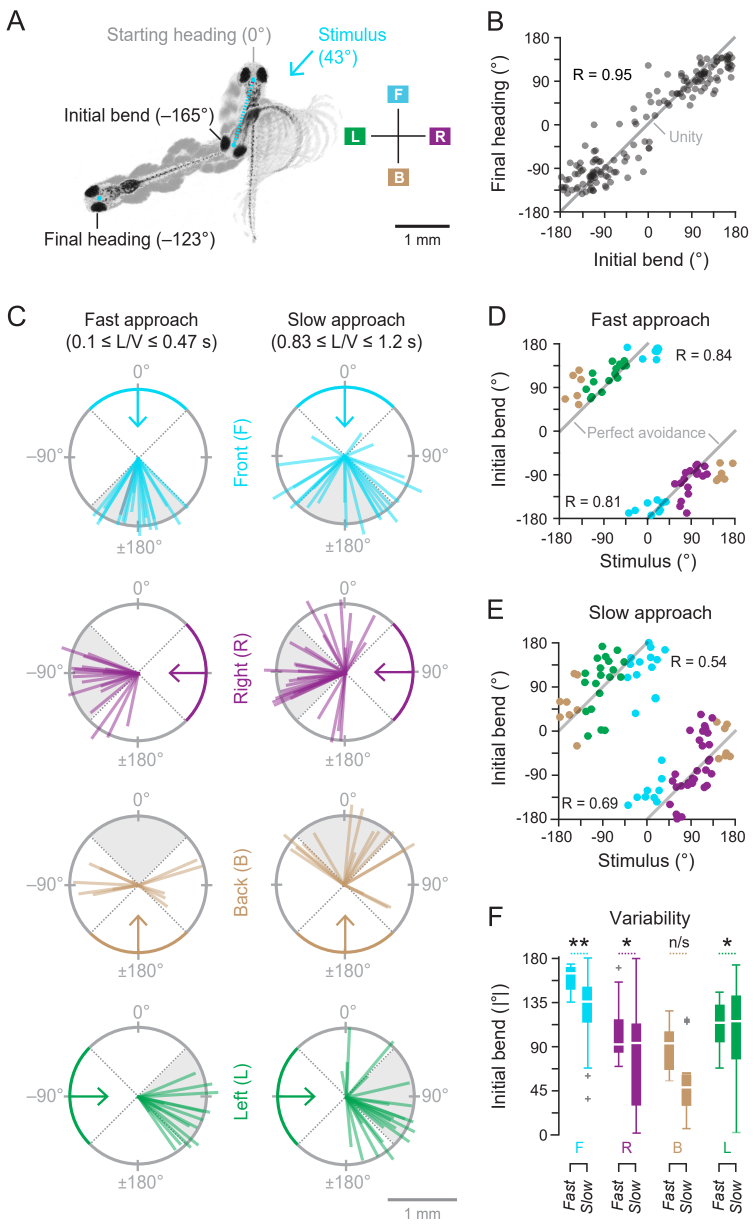

Figure 2.2. Directionality of looming evoked responses.

2.3.2. Directionality of looming evoked responses

An analysis of the kinematics of each looming evoked response was performed to investigate their relationship to the approach rate of the stimulus. In order to quantify the escape trajectory, we measured the initial bend angle for all responses (defined as in Fig. 2.2A, $N_{\text{fish}} = 21$, $N_{\text{trials}} = 246$). We also measured the final heading angle (Fig. 2.2A) in the same manner for a subset of responses ($N_{\text{fish}} = 21$, $N_{\text{trials}} = 149$) where the entire looming evoked response was not obstructed by the wall of the smaller dish. Figure 2.2B shows that the initial bend angle was a good predictor of the final heading angle. Therefore, the initial bend angle was used as an indirect measure of the final heading angle. Changes in elevation were not measured since the dish was only 4 mm deep (Fig. 2.1A).

Figure 2.2 details: A) The initial bend angle was measured for all responses ($N_{\text{fish}} = 21$, $N_{\text{trials}} = 246$) and the final heading angle was measured for a subset of responses ($N_{\text{fish}} = 21$, $N_{\text{trials}} = 149$) where the looming evoked response was not obstructed by the wall of the smaller dish. B) The initial bend angle was a strong predictor of the final heading angle and largely determined the escape direction, as evidenced by $R = 0.95$. C) The direction and translation of the head after the initial bend of responses grouped by the quadrant of the looming stimulus azimuth and by fast (small L/Vs) or slow looming (large L/Vs) stimuli showed stimulus dependent response patterns – front-fast looming: $N_{\text{trials}} = 19$, front-slow looming: 22, right-fast: 18, right-slow: 32, back-fast: 12, back-slow: 16, left-fast: 16, left-slow: 22. D) The stimulus azimuth and the initial bend angle for fast looming stimuli ($N_{\text{trials}} = 65$) were highly correlated with the lines of ‘perfect avoidance’ which correspond to a turn which directs the fish exactly 180° away from the stimulus. E) The stimulus azimuth and the initial bend angle for slow looming stimuli ($N_{\text{trials}} = 92$) were modestly correlated with the lines of ‘perfect avoidance’ due to increased variance. F) The boxplots of the absolute value of the initial bend angle for responses grouped according to azimuthal angle of the stimulus and slow or fast stimuli show a significant increase in variability of the initial bend angle when fast and slow looming stimuli were compared. This was true within each quadrant of looming stimulus azimuth, except for stimuli approaching from the back. Bottom and top of each box indicate the 25th and 75th percentiles, respectively; white line is median, whiskers extend to the last point that is not an outlier (an outlier is defined as more than 1.5 times the interquartile range beyond the median). Asterisks signify the p-value range for statistical tests. $*$: $0.01 < p \leq 0.05$, $**$: $0.001 < p \leq 0.01$, $***$: $p \leq 0.0001$

Figure 2.2C shows the vector from the center of the eyes in the starting frame to the center of the eyes at the end of the initial bend for a subset of responses grouped by small L/Vs—fast stimuli ($0.1 \leq L/V \leq 0.47$)—and large L/Vs—slow stimuli ($0.83 \leq L/V \leq 1.2$). The boundaries for the small and large L/V groups were determined by using the smallest one-third and the largest one-third of the range of L/Vs tested in this study. Additionally, the responses are also grouped into four quadrants representing the azimuthal angle of the looming stimulus: Front (–45° – 45°], Right (45° – 135°], Back (135° – 180° and –180° – –135°], and Left (–135° – –45°]. Directionality differences in the initial bend between fast and slow stimuli are immediately evident.

Figure 2.2D shows the initial bend angles of responses to fast looming stimuli plotted against the azimuthal angle of the stimulus with each response color-coded to correspond to the grouping in Fig. 2.2C. The initial bend angles were highly correlated with lines of ‘perfect avoidance’ – a turn which directs the fish’s head 180° away from the stimulus. The fish tended to head away from the aversive approaching visual stimulus. The initial bend angles to slow looming stimuli were modestly correlated with ‘perfect avoidance’ which indicates that the fish still tended to head away from the approaching stimulus but with increased variability (Fig. 2.2E).

Figure 2.2F demonstrates that there was a significant increase in the variability of the initial bend angle when comparing responses to fast looming stimuli with those to slow looming stimuli, except for cases where the stimuli approached from the back. (Levene's test, Front: $\mathrm{N}_{\text{trials, fast}} = 19$, $\mathrm{N}_{\text{trials, slow}} = 22$, $p = 0.007$, Right: $\mathrm{N}_{\text{fast}} = 18$, $\mathrm{N}_{\text{slow}} = 32$, $p = 0.011$, Back: $\mathrm{N}_{\text{fast}} = 12$, $\mathrm{N}_{\text{slow}} = 16$, $p = 0.372$, Left: $\mathrm{N}_{\text{fast}} = 16$, $\mathrm{N}_{\text{slow}} = 22$, $p = 0.021$). The absolute value of the initial bend angle was used to compute statistical significance of the variance since the discontinuity between +180° and –180° could introduce erroneously large values for variance. The results in Fig. 2.2F indicate that angle of escape to slow stimuli (large L/V) is more variable than the angle of escape to fast stimuli (small L/V), suggesting that the variability in the direction of evasive response involves an assessment of the approach rate of the threat.

2.3.3. Tail kinematics of partially restrained looming evoked responses

Further experiments were performed in a partially restrained preparation (Fig. 2.3A) since it permitted strict control over the environment, made detailed automated tracking of tail kinematics during the initial bend possible, and enabled calcium imaging at single neuron resolution during behavior. These experiments were also motivated by the need to investigate the kinematic underpinnings of the increase in the variability of the initial bend angle when comparing fast and slow looming stimuli.

Figure 2.3 details: A) Fish ($\mathrm{N}_{\text{fish}} = 18$) were partially-restrained in agar with their tails free to move and positioned to view virtual looming stimuli projected onto a screen and approaching from the front. High speed videography was used to record tail movement at 1000 fps. B) The entire tail was tracked and the tail

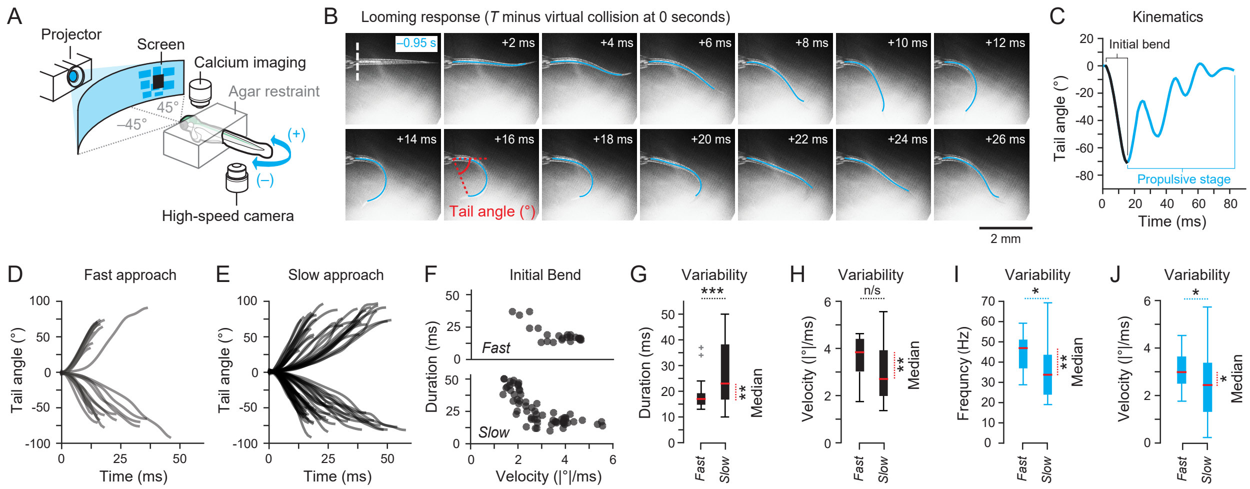

Figure 2.3. Tail kinematics of partially-restrained looming evoked responses.

angle was computed for all responses to quantify the looming evoked response. The agar restraint stopped at the end of the swim bladder marked with a dashed white line. C) Tail kinematics during the initial bend (in black) and the propulsive stage (in cyan) were extracted from the responses. D) The progression of the tail angle during the initial bend grouped by responses to fast stimuli (small L/Vs, $N_{\text{trials}} = 25$) and E) slow stimuli (large L/Vs, $N_{\text{trials}} = 63$) showed qualitative differences. F) Fish controlled absolute tail angle velocity and initial bend duration differently under each stimulus paradigm. G) Responses to fast stimuli had a shorter and less variable initial bend duration but H) a faster and equally variable tail angle velocity when compared to responses to slow stimuli. I) Responses to fast stimuli also had a higher and less variable frequency of swimming with J) higher and less variable average absolute tail angle velocities during the propulsive stage.

Individual larvae ($N_{\text{fish}} = 18$) at 5–7 dpf were partially restrained in agarose (Fig. 2.3A) and positioned to view looming stimulus projections on a diffusive screen. Looming stimuli were psuedorandomly selected from the same range of L/Vs used previously (0.1–1.2 s) but the azimuthal angle of the stimulus varied uniformly between –45° and +45°. Stimuli were restricted within this azimuthal range since responses to stimuli approaching from the front provided the highest confidence (smallest p-value) in their being a difference between responses to fast and slow stimuli (Fig. 2.2F). High speed videography at 1000 fps was used to capture body movements through a 4X objective below the transparent dish in which the fish was placed. The shape of the body from the caudal swim bladder to the end of the tail was tracked with a custom Matlab program (Fig. 2.3B). The tail angle, which is the angle between the heading vector and a vector from the caudal edge of the swim bladder to the end of the tail (Fig. 2.3B), was quantified over the course of a swim bout (Fig. 2.3C). The initial bend is easily identified (drawn in black, Fig. 2.3C) in the progression of the tail angle over time during the first unilateral contraction of the tail with the propulsive stage (drawn in cyan, Fig. 2.3C) directly following.

Figures 2.3D and E show the tail angle for all recorded responses during the initial bend grouped by fast (small L/Vs, $N_{\text{fish}} = 18$, $N_{\text{trials}} = 25$) and slow stimuli (large L/Vs, $N_{\text{fish}} = 18$, $N_{\text{trials}} = 63$) where the same L/V boundaries as in the free swimming experiments were used for grouping. The differences of the tail angles between the two groups visible in Figs. 2.3D and E is quantified in Fig. 2.3F. This shows that the fish controlled the duration of the initial bend and the absolute average tail angle velocity during the initial bend differently across stimulus paradigms. The absolute value was used to group right and left turns together as was done in the free swimming case (Fig. 2.1D and Fig. 2.2F). The initial bend duration and the tail angle velocity together allow for inferences about the initial bend angle because the tail angle velocity of free swimming fish were strongly correlated with the head yaw velocity during the initial bend (refer to Appendix A.1).

The data in Fig. 2.3F is further analyzed in Figs. 2.3G and H which demonstrate that the responses to slow stimuli had initial bend durations which were significantly longer (Mann-Whitney U test, $p = 0.005$) and more variable (Levene's test, $p < 0.001$) than those to fast stimuli. Moreover, the absolute tail angle velocities of responses to slow stimuli were lower (Mann-Whitney U test, $p = 0.002$) but had a non-significant difference in variability (Levene's test, $p = 0.177$) from responses to fast stimuli. The results in Fig. 2.3G and H together show that the looming-evoked response kinematics vary with L/V and the increase in variability of the duration is the largest contributor to variability in the initial bend.

Although both fast and slow stimuli had on average 3 tail cycles in the propulsive stage (Fig. 2.3C) there were significant differences in the kinematics during the propulsive stage for the two stimulus paradigms (Fig. 2.3I and J). Responses to slow stimuli had average tail cycle frequencies (Fig. 2.3I) in the propulsive stage which were lower (Mann-Whitney U test, $p = 0.002$) and more variable (Levene's test, $p = 0.034$). Additionally, the average absolute tail angle velocity of responses to slow stimuli during the propulsive stage was lower (Mann-Whitney U test, $p = 0.021$) and more variable (Levene's test, $p = 0.032$). These results together demonstrate significant stimulus dependent changes in the kinematics of the looming evoked response based on the looming rate—the threat posed by the stimulus.

Figure 2.4 details: A) Partially restrained fish ($N_{\text{fish}} = 15$) were shown a fast ($L/V = 0.4$ s) and a slow ($L/V = 1.0$ s) looming stimulus at an azimuth of –30°, which consistently produced rightward looming evoked turns. B) The M-cell (within yellow square) is in the larval zebrafish hindbrain with contralateral axonal projections (yellow arrow) known to mediate rightward turns. Calcium imaging of the left M-cell was performed in all fish at 30 fps. High speed videography of the tail movement was simultaneously performed

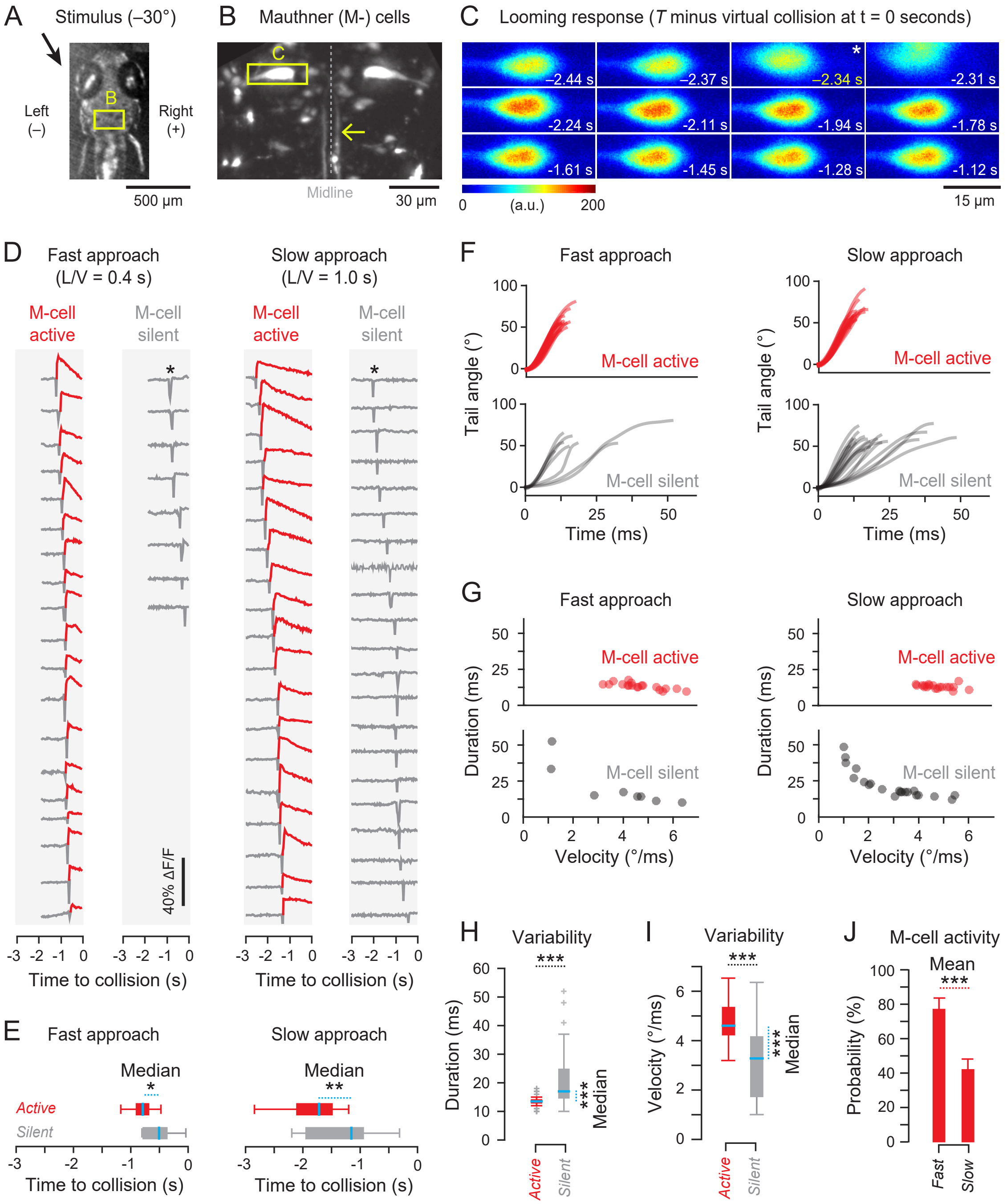

Figure 2.4. Mauthner cell activity to varying approach rates.

at 1000 fps. C) A representative M-cell active response with the frame corresponding to the start of the looming evoked response marked with a star and a motion artifact immediately following. This montage demonstrates the increase in fluorescence during neuronal activity and the quality of signals acquired with the imaging assay. D) Calcium imaging fluorescence traces for all responses ordered by response time and grouped by fast looming M-cell active ($N_{\text{trials}} = 19$) and silent ($N_{\text{trials}} = 8$) or slow looming M-cell active ($N_{\text{trials}} = 19$) and silent ($N_{\text{trials}} = 21$). M-cell activity was determined by a threshold of $\Delta F/F = 5\%$. E) In both stimulus paradigms, M-cell active responses occurred significantly earlier (more negative time) than M-cell silent responses with mean ± std as follows: $\text{Fast}_{\text{M-cell active}}$: –0.80 ± 0.17 s, $\text{Fast}_{\text{M-cell silent}}$: –0.52 ± 0.27 s, $\text{Slow}_{\text{M-cell active}}$: –1.80 ± 0.44 s, $\text{Slow}_{\text{M-cell silent}}$: –1.27 ± 0.59 s. F) The progression of the tail angle during the initial bend of responses to fast and slow stimuli grouped by M-cell active or silent showed immediate differences. G) M-cell active responses under different stimuli had similar initial bend durations and tail angle velocities but were different from M-cell silent responses. H) M-cell active responses had a shorter and less variable distribution of initial bend durations than M-cell silent responses. I) M-cell active responses had a higher and less variable distribution of tail angle velocities during the initial bend than M-cell silent responses. J) Fish ($N_{\text{fish}} = 15$) were much more likely to produce an M-cell active response to a fast stimulus than to a slow stimulus.

2.3.4. Mauthner cell activity to varying approach rates

To investigate how the approach rate of looming stimuli influenced the likelihood of Mauthner cell (M-cell) activation, calcium imaging was performed while larval fish responded to looming stimuli. A previously established protocol was used to backfill the reticulospinal network neurons of anesthetized 4 dpf zebrafish with Calcium Green dextran Liu and Fetcho

(1999). In the partially restrained looming stimulus assay, we simultaneously measured neural activity in the M-cell from above with a 40X objective and body kinematics from below with a 4X objective (Fig. 2.3A). Fish were shown a slow stimulus (L = 11 mm, V = 11 $\frac{\text{mm}}{\text{sec}}$, $L/V = 1.0$, d = 50 mm) and a fast stimulus (L = 11 mm, V = 27.5 $\frac{\text{mm}}{\text{sec}}$, $L/V = 0.4$, d = 50 mm), both at an azimuth of 30° from the left (Fig. 2.4A). Only these two approach rates were used rather than the full set because investigating the variability of Mauthner recruitment to a fixed stimulus requires a large sample size; thus surveying the full set of approach rates is impractical.

Fig. 2.4B shows a representative maximum-intensity z-projection fluorescent image (collected with an epiflourescent microscope) of a portion of the reticulospinal network with the left M-cell inscribed within a green rectangle. The left M-cell has one commissural axon (green arrow) which is known to mediate escape turns to the right Gahtan and Baier (2004). Since z-stacking was too slow in this case for neural activity imaging during behavior, the M-cell was imaged at 30 fps in a single plane in a small region that just encompassed the neuron (Fig. 2.4C).

Figure 2.4C shows a montage of fluorescence images from a single trial where the fish performed an M-cell active looming evoked response. The looming evoked response occurs at −2.34 s and is immediately followed by a motion artifact in the imaging due to the vigorous nature of the aversive response. This is followed by increased flourescence due to neural activity.

Figure 2.4D shows all of the fluorescence traces from all recorded responses grouped by fast ($\text{N}_{\text{fish}} = 15$, $\text{N}_{\text{trials, active}} = 19$, $\text{N}_{\text{trials, silent}} = 8$) and slow ($\text{N}_{\text{fish}} = 15$, $\text{N}_{\text{trials, active}} = 19$, $\text{N}_{\text{trials, silent}} = 21$) stimuli. Fluorescence traces from the M-cells of fish performing looming evoked responses were compiled into M-cell active and silent groups based on a decision threshold at $\Delta F/F = 5\%$ (justified in Appendix A.3). All fluorescence traces show a sharp drop at the time of response due to the motion artifact (Fig. 2.4C) in fluorescence imaging.

M-cell active responses happened significantly earlier (more negative response times) than M-cell silent responses for both fast (Mann-Whitney U test, $p = 0.014$, 284 ms difference in medians) and slow (Mann-Whitney U test, $p = 0.006$, 563 ms difference in medians) stimuli (Fig. 2.4E). The mean ± std responses times for the groups were the following: $\text{Fast}_{\text{M-cell active}}$: -0.80 ± 0.17 s, $\text{Fast}_{\text{M-cell silent}}$: -0.52 ± 0.27 s, $\text{Slow}_{\text{M-cell active}}$: -1.80 ± 0.44 s, $\text{Slow}_{\text{M-cell silent}}$: -1.27 ± 0.59 s. The tail angle during the initial bend of M-cell active and silent responses grouped by the fast and slow stimuli also showed differences (Fig. 2.4F). These differences are further quantified in Fig. 2.4G which demonstrate that the M-cell active responses had different initial bend durations and tail angle velocities from M-cell silent responses for the both fast and slow looming stimuli. Figure 2.4H shows that the initial bend duration for M-cell active responses were significantly smaller (Mann-Whitney U test, $p \lll 0.001$) and less variable (Levene's test, $p \lll 0.001$) than M-cell silent responses. The tail angle velocity during the initial bend for M-cell active responses was also significantly higher (Fig. 2.4I, Mann-Whitney U test, $p < 0.001$) and less variable (Levene's test, $p < 0.001$) than M-cell silent responses. The proportion of M-cell active responses is far higher for fast stimuli than for slow stimuli (Fig. 2.4J). These results together indicate that the approach rate of the looming stimuli modulates the probability of M-cell recruitment, which is correlated with specific kinematic outcomes.

2.3.5. Reticulospinal recruitment during Mauthner active and silent responses

To study recruitment differences in the reticulospinal network between Mauthner cell active and silent looming-evoked responses, volumetric calcium imaging was performed on a subset

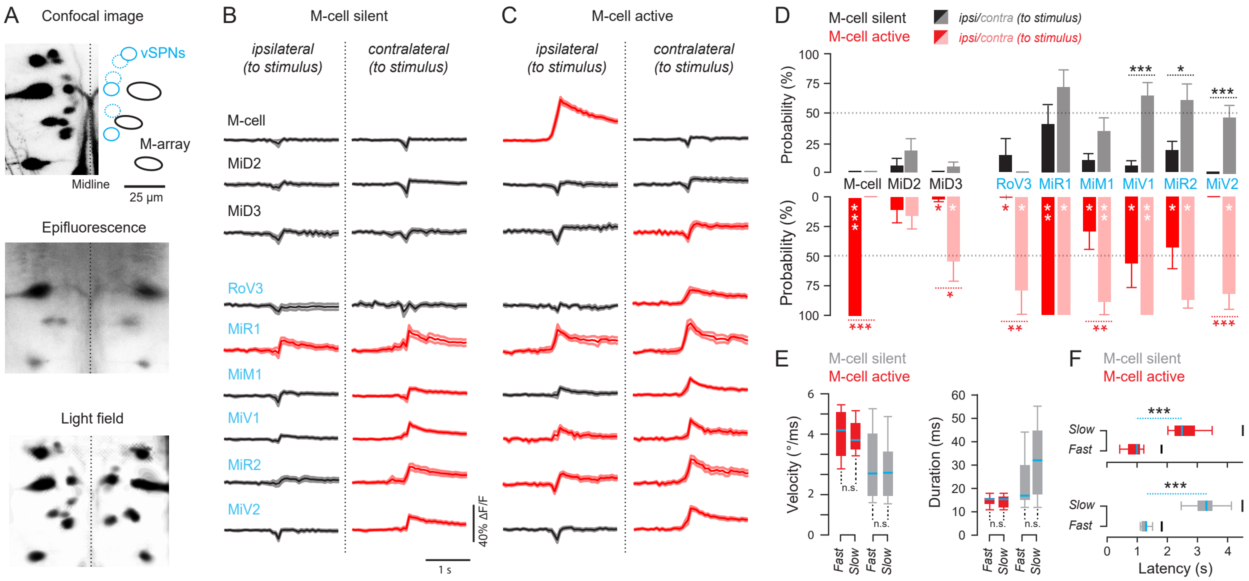

Figure 2.5. Reticulospinal recruitment during Mauthner silent and active responses.

of the reticulospinal neurons in conjunction with high-speed behavior imaging while larval zebrafish responded to the same fast or slow looming stimuli described above. Light field microscopy was used to acquire volumetric calcium fluorescence data (70 µm × 100 µm × 100 µm) at 15 fps from the Mauthner cells (M-cells) and its homologs, MiD2 and MiD3, along with other ventral spinal projecting neurons (vSPNs) that have been identified in previous literature to be involved in turning behavior Orger et al. (2008). These vSPNs include RoV3, MiR1, MiM1, MiV1, MiR2, and MiV2, listed here in rostro-caudal order of anatomical occurrence (Fig. 2.5A).

Figure 2.5 details: A) Compares the maximum intensity z-projection of a volume acquired with confocal microscopy (top, acquisition time: 10 mins) with a single plane from epifluorescence microscopy within the same volume (middle, acquisition time: 50 ms) and a max intensity z-projection of the same volume reconstructed from a light field image (bottom, acquisition time: 50 ms) demonstrating the utility of light field imaging as a fast volumetric imaging system able to resolve the neurons of interest. In this study, we specifically focused on the Mauthner cell and its homologs (M-array, top, in black) along with the ventral spinal projecting neurons (vSPNs, top, in blue). B) Plots show the average calcium signals with upper and lower SEM boundaries from each nucleus during M-cell silent looming-evoked responses across all trials ($25 \leq N_{\text{trials}} \leq 35$, for exact values please refer to Appendix A.4) and C) The same is shown for M-cell active looming evoked responses ($34 \leq N_{\text{trials}} \leq 50$). Nuclei names are color-coded in black or blue in accordance with their membership in either the M-array or the vSPNs. Red traces denote nuclei for which the mean of the calcium signal reached above the $\Delta F/F$ threshold (5%) for activation. D) Shows the average ±SEM recruitment probability of nuclei for M-cell active and silent cases grouped by fish ($5 \leq N_{\text{fish}} \leq 17$). E) Demonstrates the similarity of angular velocity and bend duration distributions within M-cell active and M-cell silent cases regardless of approach rate (M-cell active: $N_{\text{Fast}} = 24$, $N_{\text{Slow}} = 26$, M-cell silent: $N_{\text{Fast}} = 11$, $N_{\text{Slow}} = 24$). F) Shows the differences in latency of M-cell active and M-cell silent responses from the onset of the stimulus for each approach rate. The latency of the responses from stimulus onset are the following: M-cell $\text{Active}_{\text{fast}}$: 0.99 ± 0.17 s, M-cell $\text{Active}_{\text{slow}}$: 2.47 ± 0.38 s, M-cell $\text{Silent}_{\text{fast}}$: 1.3 ± 0.25, M-cell $\text{Silent}_{\text{slow}}$: 3.31 ± 0.51.Short black bars at 1.82 s and 4.54 s mark the latency at which each stimulus would collide with the fish.

Light field imaging was ~10,000 times faster than confocal imaging (confocal image example Fig. 2.5A top) for acquiring the volume of interest. A standard epifluorescence image at a single plane (Fig. 2.5A, middle) is insufficient to reconstruct the entire volume. However, a modified epifluorescence scope with a microlens array provides a light field with sufficient information to reconstruct the volume (Fig. 2.5A, bottom)Broxton et al. (2013). After post-processing, segmenting, and anatomically labeling volumes reconstructed from light field microscopy (refer to Appendix A.4), time-varying calcium signals were extracted from volumes acquired during looming-evoked escapes and grouped into M-cell silent or M-cell active response categories. The signals from these bilaterally symmetric nuclei were also grouped according to their relative location to the stimulus, either on the same side as the stimulus (ipsilateral), or on the opposite side of the stimulus (contralateral). All turns from looming stimuli were away from the stimulus direction; thus the contralateral nuclei are on the same side that the fish turns toward.

The average calcium signals from all trials for each nucleus (Fig. 2.5B and C) show immediate differences in recruitment between M-cell active ($34 \leq N_{\text{trials}} \leq 50$) and silent ($25 \leq N_{\text{trials}} \leq 35$, for exact values please refer to Appendix A.4) responses. Red traces denote nuclei for which the mean of the calcium signal reached above the $\Delta F/F$ threshold (5%) for activation. These recruitment patterns are further explored in Figure 2.5D which plots the average probability ± SEM of recruitment grouped by fish for each of the reticulospinal nuclei investigated ($5 \leq N_{\text{fish}} \leq 17$). The statistical results demonstrate significant differences in the mean recruitment probability between bilaterally symmetric nuclei pairs within and across M-cell active and silent responses (Student's two-tailed t-test).

The MiD3 Mauthner homolog and the RoV3 nuclei contralateral to the stimulus were frequently recruited (MiD3: 55 ± 15% recruitment probability, RoV3: 77 ± 18% recruitment probability) during M-cell active responses but were rarely or never active during M-cell silent ones. Other nuclei such as MiV1, MiR2, and MiM1 showed prominent changes in the symmetry of bilateral recruitment. While the M-cell silent responses had significant recruitment of MiV1 and MiR2 nuclei contralateral to the stimulus (Fig. 2.5B and D, $p_{\text{MiV1}} = 0.0006$, $p_{\text{MiR2}} = 0.023$), M-cell active responses had increased recruitment of both nuclei but no significant difference in recruitment of bilateral pairs (Fig. 2.5C and D). However, M-cell active responses had significant unilateral recruitment of the MiM1 nuclei contralateral to the stimulus ($p = 0.003$) while M-cell silent responses show a reduced recruitment of MiM1 nuclei but non-significant differences between recruitment of bilateral pairs. Some nuclei, like MiR1 and MiV2 have an overall drop in recruitment probability when comparing M-cell active to silent but no changes in symmetry or asymmetry of activation in the bilateral pairs.

Figure 2.5E demonstrates that angular velocity and bend duration distributions of Stage 1 were not significantly different within M-cell active responses for each approach rate or within M-cell silent responses for each approach rate (M-cell active: $\mathrm{N_{Fast}} = 24$, $\mathrm{N_{Slow}} = 26$, M-cell silent: $\mathrm{N_{Fast}} = 11$, $\mathrm{N_{Slow}} = 24$). These results suggest that M-cell active responses and M-cell silent responses are two different behavioral responses that are consistent in their kinematics regardless of the stimulus parameters. Despite the similarity of kinematics of M-cell active responses across both stimuli and M-cell silent responses across both stimuli, there are significant differences in the latency from stimulus onset of the responses ranging from 1.5–2.5 s between the two approach rates (Fig. 2.5F). The latency of the responses for the groups are the following: M-cell $\mathrm{Active_{fast}}$: 0.99 ± 0.17 s, M-cell $\mathrm{Active_{slow}}$: 2.47 ± 0.38 s, M-cell $\mathrm{Silent_{fast}}$: 1.3 ± 0.25, M-cell $\mathrm{Silent_{slow}}$: 3.31 ± 0.51. The same behaviors in response to different stimuli are being activated at very different time scales. Nonetheless, M-cell active responses still precede M-cell silent ones for a given stimulus, as also seen in Figure 2.4E.

2.4. Discussion

Our goal here was to evaluate how larval zebrafish assess threat of looming predators to determine the utility of short latency, ballistic responses over longer latency, more variable and less energetically costly behaviors. While previous literature suggested a proximity mechanism of threat assessment which is insensitive to varying levels of threat, we found that fish perform a graded assessment of threat where the approach rate of the looming stimulus modifies the likelihood of an evasive maneuver, its kinematics, and the proportion of evasive responses that involve Mauthner cell activation (Fig. 2.6).

Mauthner-mediated escapes are both energetically costly, as they rapidly engage muscles along the entire body Fetcho (1991), and behaviorally costly, as they produce predictable escape responses Catania (2009); Eaton et al. (1991). Therefore, we hypothesized that Mauthner cell recruitment would be reserved for the more urgent threats. This hypothesis was supported by our kinematic analysis combined with *in vivo* imaging of Mauthner cell recruitment which confirmed that Mauthner-active responses are the most powerful and stereotyped, and were more likely to occur in response to faster looming stimuli (Fig. 2.6).

Figure 2.6 details: The looming-evoked response of a larval zebrafish is modulated by the approach rate of the looming stimulus. As a predator nears the critical subtended angle threshold, fish decide to either move or freeze in a probabilistic manner based on the approach rate. If the fish moves, it must decide between Mauthner active and Mauthner silent responses—the probability of which is also determined by the approach rate. Mauthner active and Mauthner silent circuitry have different neural recruitment patterns and produce kinematically distinct behaviors. Mauthner active responses recruit the Mauthner cell along with Mauthner homologs, and other ventral spinal projection neurons to produce a short latency, more stereotyped maneuver, which is generally directed 180° away from the stimulus approach direction (in black). Meanwhile, Mauthner silent responses almost exclusively recruit the ventral spinal projecting neurons to produce longer latency responses with more variable kinematics and escape directions (in blue).

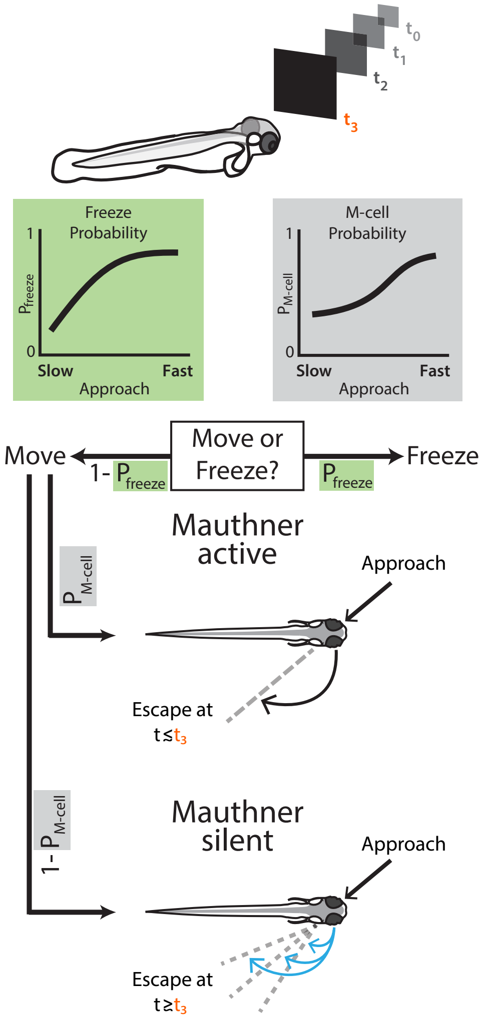

Figure 2.6. The looming-evoked response of a larval zebrafish.

However, our findings also indicate that the decision to recruit Mauthner neurons is occurring in parallel with another decision: whether to move at all (Fig. 2.6). We observed more responses to slowly expanding stimuli than rapidly expanding stimuli. A possible explanation for this difference in response probability is that the faster visual stimulus is too rapid to be perceived. However, we find that fish were able respond to the shortest duration stimuli presented in this study, suggesting that the duration of the stimulus was sufficient to drive visually guided responses for all approach rates. It is therefore more likely that this lack of response is evidence of ‘freezing’ behavior, a common reaction to highly threatening visual stimuli in a variety of species Blanchard and Blanchard (1988); Chelini et al. (2009); Herberholz and Marquart (2012), including zebrafish Egan et al. (2009). Others have suggested that freezing can reduce vibrational and visual cues that a predator may rely on, loosing interest if such stimulation ceases Misslin (2003). Here we argue that the choice between freezing or escaping in larval zebrafish is modulated by the approach rate of a looming stimulus.

Slower approach rates were more likely to produce Mauthner-silent escapes which are more delayed and more variable in their kinematics than Mauthner-active responses (Fig. 2.6). The behavioral utility of more variability in response to slowly approaching objects is supported by modeling studies, which suggest that slower predators allow for a wider range of escape directions that maximize distance Soto et al. (2015). In addition, more variable escape trajectories are arguably less predictable, which would be advantageous when responding to slower and more maneuverable predators MacIver et al. (2004); Bandyopadhyay et al. (1997).

While there are clear differences in the timing and variability of escape turns to slow and fast looming stimuli, almost all responses were evasive, in that zebrafish made a ~180° turn away from the perceived threat. One notable exception was responses to fast approaching objects from the rear, in which case larvae did not move forward, but rather turned ~90° to the left or right. Although we did not monitor Mauthner cell recruitment in this situation, the deviation from the expected escape direction is most likely due to the higher probability of Mauthner cell firing, which guarantees a turning maneuver. Indeed, electrical stimulation of the Mauthner cell alone yields a stereotyped tail bend that can reach 85° Nissanov et al.

(1990). In this specific case, the commensurate neurobiological and biomechanical constraints may actually be beneficial, since the optimal strategy is to dart to the side when escaping predators which are much faster than prey and rapidly approaching from behind Weihs and Webb (1984); Corcoran and Conner (2016).

Notwithstanding this observation, for all other looming evoked responses, zebrafish move directly away from the perceived threat. This necessitates a means of directional coding. Our work suggests variations in escape trajectory can be explained largely by the duration of the initial bend, and to a lesser extent by tail angle velocity. This observation is congruent with studies in the spinal cord that have revealed a mechanism of turn angle encoding through modulating the number of spikes in participating excitatory premotor interneurons and motor neurons Bhatt et al. (2007). Such a mechanism could manipulate changes in duration by modulating firing frequency of the interneurons and motor neurons. Given that Mauthner cells typically fire only once during the initial bend Korn and Faber (2005), the modulation of spike rate and bend duration necessary for direction control must arise elsewhere. The most likely sources for modulation of spike rate and bend duration are other identified reticulospinal neurons, which have been implicated in directional coding of more abrupt sensory stimuli Eaton et al. (1988); Gahtan et al. (2002) along with routine turning Orger et al. (2008); Huang et al. (2013).

Moreover, differences in the recruitment of these nuclei during Mauthner-active and Mauthner-silent responses may speak to their roles in these kinematically distinct behaviors. Specifically, the frequent recruitment during Mauthner-active responses of the MiD3 nucleus and the RoV3 nucleus contralateral the stimulus—on the opposite side of the active Mauthner cell—suggests they play a critical role in this evasive maneuver. The recruitment of the MiD3 nucleus on the opposite side of the active Mauthner cell aligns well with findings from other researchers Neki et al. (2014). Moreover, both the MiD3 and RoV3 nuclei may be providing excitatory input in conjunction with the Mauthner cell during Stage 1 since studies have suggested that ipsilaterally projecting MiD3 cells are excitatory Kinkhabwala et al. (2011); Kimura et al. (2013) and the RoV3 nucleus is integral for turning behaviors Orger et al. (2008); Huang et al. (2013).

This rationale also applies to the MiM1 nuclei which had strong unilateral recruitment during Mauthner-active responses. This finding aligns with previous results which demonstrate that the activation of one Mauthner cell leads to the recruitment of the MiM1 nucleus on the opposite side Neki et al. (2014). Our results further support the hypothesis that the MiM1 nucleus may be contributing to the lateralized activation of the spinal neurons during Stage 1 of the escape maneuver.

Meanwhile, the MiV1 and MiR2 nuclei largely undergo changes in the symmetry of recruitment between the bilateral pairs when comparing Mauther-active and Mauther-silent responses. Others have reported that there are two functional groups of neurons within the MiV1 nucleus: one group with strong directional turning that is only active during turns, and a second group with weak directional turning that is more active during turns but also active during forward swimming behaviors Huang et al. (2013). This suggests that the more bilateral recruitment of MiV1 nuclei during Mauther-active responses tend to activate both functional groups while the unilateral recruitment during Mauther-silent responses may only activate the group with strong directional tuning. The similar trend in the symmetry of recruitment seen in the MiR2 nuclei could potentially be explained by a congruent mechanism of recruiting different functional groups. Previous literature suggests that there are MiR2 neurons active during forward swimming Orger et al. (2008), but the strong unilateral recruitment of one of the bilateral pairs during Mauther-silent responses in our findings indicates involvement of this nucleus in turning behaviors as well.

The MiR1 and MiV2 nuclei undergo a drop in recruitment probability when comparing Mauthner-active and Mauthner-silent responses but do not have changes in the symmetry of recruitment between bilateral pairs. There is some evidence that the MiR1 nucleus is active during forward swimming Orger et al. (2008) which is further corroborated in this study by the bilateral recruitment seen in both Mauther-active and Mauthner-silent responses. The significant unilateral recruitment of MiV2 nuclei aligns well with previous findings which show that they have strong directional tuning Orger et al. (2008); Huang et al. (2013).

The consistent differences in the kinematics of the Mauther-active and Mauthner-silent responses across approach rates suggests that these clear changes in the recruitment of nuclei are correlated to the distinct changes in the motor aspects of these behaviors. Overall, our results indicate that during Mauthner-active responses MiD3, RoV3, MiM1, and MiV2 nuclei have input into the turning portion of an evasive maneuver—Stage 1. Meanwhile, MiV1 and MiR2 nuclei have input both into the turning portion and forward swimming—the propulsive stage. However, during Mauthner-silent responses, only a subset of these, namely MiM1, MiV1, MiR2, and MiV2 are still involved in turning. The reduced probability of recruitment for these nuclei could explain the longer Stage 1 duration and lower median tail angle velocity during Stage 1, since this would translate into weaker, presumably less synchronous drive to the spinal interneurons and motor neurons responsible for escapes, as described above.

In both types of responses, the bilateral activation of MiR1 implicates its involvement in forward swimming. Our kinematic analysis suggests that forward swimming during the propulsive stage of the responses to rapidly expanding stimuli are produced at higher frequencies and tail angle velocities, and are less variable. This may be due to the increased recruitment of MiR1 nuclei along with the recruitment of functional subgroups responsible for forward swimming within the MiV1 and, potentially, MiR2 nuclei. Studies of spinal networks in the larval zebrafish suggest that premotor excitatory interneurons active at lower frequencies of swimming—which comprise longer, more variable bend durations—are inhibited as those active at higher frequencies of swimming are engaged Kishore et al. (2014). It is unclear whether the reticulospinal neurons responsible for higher swimming frequencies are organized hierarchically according to speed as in the spinal cord. One interpretation of our results is that the MiR1 nuclei provide excitatory drive for forward swimming while the functional subgroups for forward swimming within MiV1 and MiR2 select for spinal networks mediating higher frequency swimming.

The mechanisms responsible for recruiting Mauthner versus non-Mauthner escape circuits are still unclear, but presumably arises from a combination of their integrative properties and the nature of input from upstream visual processing centers Wang and McLean (2014). One possibility is that visual inputs are evenly distributed among spinal projecting neurons. In this case rapidly expanding objects resulting in strong, coincident activation of a shared source visual drive would favor recruitment of large Mauthner cells, while weaker stimuli provided by slowly expanding objects would be more likely to recruit only smaller non-Mauthner circuitry. This aligns with our finding of probabilistic Mauthner cell recruitment with respect to approach rate. A coincidence detection mechanism would also predict that the protracted summation of stimuli from more slowly approaching predators would lead to a more delayed activation of Mauthner neurons, which is what we observe for responses to slow looming stimuli.

However, the changes in symmetry of recruitment of the bilateral pairs of MiV1 and MiR2 nuclei between Mauthner-active and Mauthner-silent responses are more difficult to explain with an even distribution of visual input. In this case, the Mauthner cell, once activated, could be providing additional excitatory drive to other reticulospinal cells, which is consistent with previous studies Neki et al. (2014). Moreover, the excitatory visual input to the ventral spinal projecting neurons may also be biased to the nuclei contralateral to the stimulus. In addition, functional subgroups of neurons which recruit spinal circuits for faster swimming within reticulospinal nuclei may have higher activation thresholds. The combination of contralateral bias and heterogenous activation thresholds in nuclei could also explain circuit level differences in Mauthner-active and Mauthner-silent escapes.

Another potential argument against an even distribution of visual input to reticulospinal neurons is provided by our observation that responses involving Mauthner neurons occur consistently earlier than non-Mauthner responses, by as much as half a second for slowly looming objects (Fig. 2.4E). The delay of the non-Mauthner response in these cases cannot be explained by differences in reticulospinal conduction velocity alone and instead suggests the existence of a lower threshold, biased source of visual input to Mauthner neurons. This would be consistent with studies of auditory escape reflexes, where the early recruitment of Mauthner neurons is ensured by stronger drive from XIIIth nerve afferents Curti and Pereda (2004). Nonetheless, the large differences in latency from stimulus onset for Mauthner-active responses when comparing fast and slow looming stimuli suggests that the critical subtended angle threshold is modulating the timing of this biased input to the Mauthner neurons.

Furthermore, the reduced responsiveness—freezing response—we observe with increasing probability as speed of approach increases could be evidence of an independent network. However, the descending control of freezing behavior in larval zebrafish is not well understood. While the sources of input to the reticulospinal cells likely include looming responsive neurons in the optic tectum and/or extratectal areas Temizer et al. (2015); Dunn et al.

(2016), future work examining differences in the response of visual processing centers and their output with changing looming rate will help distinguish between these possibilities.

Our results illustrate that larval zebrafish performed a graded assessment of threat when responding to aversive stimuli, producing differing behavioral outcomes based on the threat posed by the stimulus. More broadly, the story of the role of Mauthner versus non-Mauthner mediated behavior is a microcosm of a larger logic at play. That logic offers a trade-off between deciding to execute fast and relatively stereotyped responses or slower and more flexible responses. While the Mauthner cell and other giant-fiber pathways are a window into this decision-making process, the balance between fast and slow responses to stimuli is maintained by the relationship between the sensory range of the animal, the reaction time of animal, and the speed of the approaching object. Limited sensory range—due to sensory modality, like mechanosensation, and ecology, like murky water—or very rapidly approaching predators would tip the balance in the favor of fast, inflexible responses. Conversely, slowly moving predators or increased sensory range—as would have happened starting around 385 million years ago when certain fish evolved into land animals and were able to see targets from a far greater distance MacIver et al. (2017)—may tip the balance in favor of slower and more flexible responses, as these are more likely to challenge the predator by their lack of predictability. This influence of increased sensory range on reducing the benefit of short latency responses is further supported by the fact that Mauthner cells are only known to be present in vertebrates up through amphibians, including frogs Bierman et al. (2009). While our study investigates this trade-off and the decision-making process involving a giant-fiber system in a relatively simple aquatic vertebrate, similar mechanisms may be at play in higher vertebrates with their increased luxury of time and more numerous behavioral options afforded by larger sensing range.

CHAPTER 3

Intersection of motor volumes determines outcome of predator-prey interactions

3.1. Overview

In predator-prey interactions, the escape maneuvers of prey animals are crucial in determining their chances of survival. Therefore, these maneuvers and the neural circuits that execute them are shaped by stiff selection pressure. Our current understanding suggests that a number of escape maneuver parameters contribute to survival, including response latency, escape speed, and direction. However, existing studies present contradictory evidence about the impact of these parameters on escape success. Specifically, the value of rapid responses and fast speeds in producing successful escapes has been disputed, even while many animals have specialized circuits devoted to producing the shortest latency and fastest escapes. These contradictions obscure an understanding of the selection pressure on escape maneuvers and the functional benefit of specialized escape circuits. To clarify these issues, we have investigated the determinants of successful escape maneuvers by studying the responses of larval zebrafish to the ballistic attacks of a natural predator, the dragonfly nymph. We found that the strongest predictor of outcome was the time needed for the nymph to reach the fish after the fish had initiated an escape. We show how this result is a consequence of the intersection of the volume containing all possible escape trajectories of the fish and the swept volume of the nymph's attack. By analyzing the interaction of these volumes, we estimated the survival benefit conferred to larval zebrafish by recruiting the Mauthner cell, the giant neuron in fish devoted to producing escapes. Our approach provides a new perspective on the selection pressure on movements during predation by presenting a general framework that unifies the influence of many escape maneuver parameters in shaping the motor volumes of predator and prey.

3.2. Introduction

An escalating “arms race" in predator-prey interactions is considered a major driving force behind the evolution of nervous systems Sperling et al. (2013). Within these interactions, the escape maneuvers of prey are under significant selection pressure since they directly affect survival. The evolutionary pressure shaping escape maneuvers selects for those parameters of the maneuver and the underlying neural circuitry that contribute to evasion success Sillar et al. (2016). Studies have suggested that response latency, speed, and direction of an escape maneuver are all relevant contributors to success Howland (1974); Dangles et al. (2006); Stewart et al. (2013). However, different studies have produced contradictory results about the influence of these parameters on the outcome.

Opposing parameters, like the optimality of a single escape direction for increasing distance Weihs and Webb (1984); Eaton et al. (1991); Domenici (2002) and the unpredictability of variable escape directions Driver and Humphries (1970); Edut and Eilam (2004); Domenici et al. (2011b), are both hypothesized to increase escape success. Moreover, in many animals, escapes can be initiated with or without the activation of large diameter command neurons devoted to generating the shortest latency escapes with the fastest speeds Edwards et al. (1999); Korn and Faber (2005); Card (2012). In fishes and amphibians, these giant neurons, called the Mauthner cells, are found as a bilateral pair in the brainstem Korn and Faber (2005). However, the utility of fast speeds for increasing evasion success in fish have been both disputed and supported by existing results Webb (1986); Katzir (1993); Walker et al. (2005); Fuiman et al. (2006); Soto et al. (2015); Nair et al. (2017), obscuring the role of recruiting the Mauthner cells. Therefore, it is unclear how the recruitment of specialized escape circuits or the selection of specific motor parameters for an escape maneuver increase chances of escape success.

To better understand the determinants of successful escapes, we have studied the predation of larval zebrafish (*Danio rerio*) by one of their known ambush predators, the dragonfly nymph (*Sympetrum vicinum*). Dragonfly nymphs hunt by remaining motionless and waiting for prey to come within ambush distance Snodgrass (1954); Pritchard (1965) (Fig. 3.1). Once in striking range, the nymphs attack prey with their hydraulically-powered prehensile labial masks Olesen (1972); Tanaka and Hisada (1980); Parry (1983); Busse and Gorb (2018) which extend outward to grasp the prey with palps and confine them in a spoon-shaped bowl Olesen (1978); Blanke et al. (2015), hereafter referred to as a mask. Studying responses to an ambush predator better explicates the impact of escape maneuver parameters on the outcome than a similar analysis with a pursuit predator. This is because responses to pursuit predation involves a series of movements where it is difficult to determine which parameter ultimately led to successful escape. Conversely, ambush predation, which involves sudden strikes by predators on unsuspecting prey deVries et al. (2012), does not provide time for a series of movements. Consequently, we focused on single escape responses of larval fish to the ballistic strikes of dragonfly nymphs to find the parameters most predictive of the outcome.

Using the time needed to extend the mask to a position in space, we created a model of the mask motor volume—the volume swept by the appendage over a given amount of time Snyder et al. (2007). The fluid perturbations caused by the extending mask modulated timing and kinematics of the fish escape response. Upon analysis of various parameters defining the escape response, we found that the time remaining for the mask to reach the fish position from the initiation of the fish's escape response was most predictive of escape success. Ultimately, our findings are a consequence of the intersection of the swept volume of the mask and the volume containing all possible trajectories of the fish within the time remaining to mask arrival—the fish's motor volume Snyder et al. (2007). We show how the interaction between the prey motor volume and the predator swept volume accounts for the influence of various escape maneuver parameters and provides a new approach to analyze the utility of specific escape movements. Additionally, we use the analysis of motor volumes to computationally estimate the survival benefit of recruiting the Mauthner cell for the escape maneuver since there are known differences in kinematics for Mauthner and non-Mauthner mediated escapes Liu and Fetcho (1999); Burgess and Granato (2007); Kohashi and Oda (2008); Bhattacharyya et al. (2017). We discuss how our conclusions generalize to other predator-prey interactions and extend the existing understanding of the selection pressure on escape responses along with their neural execution.

3.3. Results

3.3.1. Dragonfly nymph prehensile mask motor volume and attack outcome

To evaluate predator-prey interactions, we filmed strikes of dragonfly nymphs upon 5–7 day old larval zebrafish using high-speed videography at 250 frames per second (fps) with top and side view perspectives (Figure 3.1A).

Figure 3.1 details: A) Top and side view of a strike. Scale bar: 2.5 mm. B) Top, front, and side view orthographic projections of prehensile mask strike positions colored to represent the time duration of the

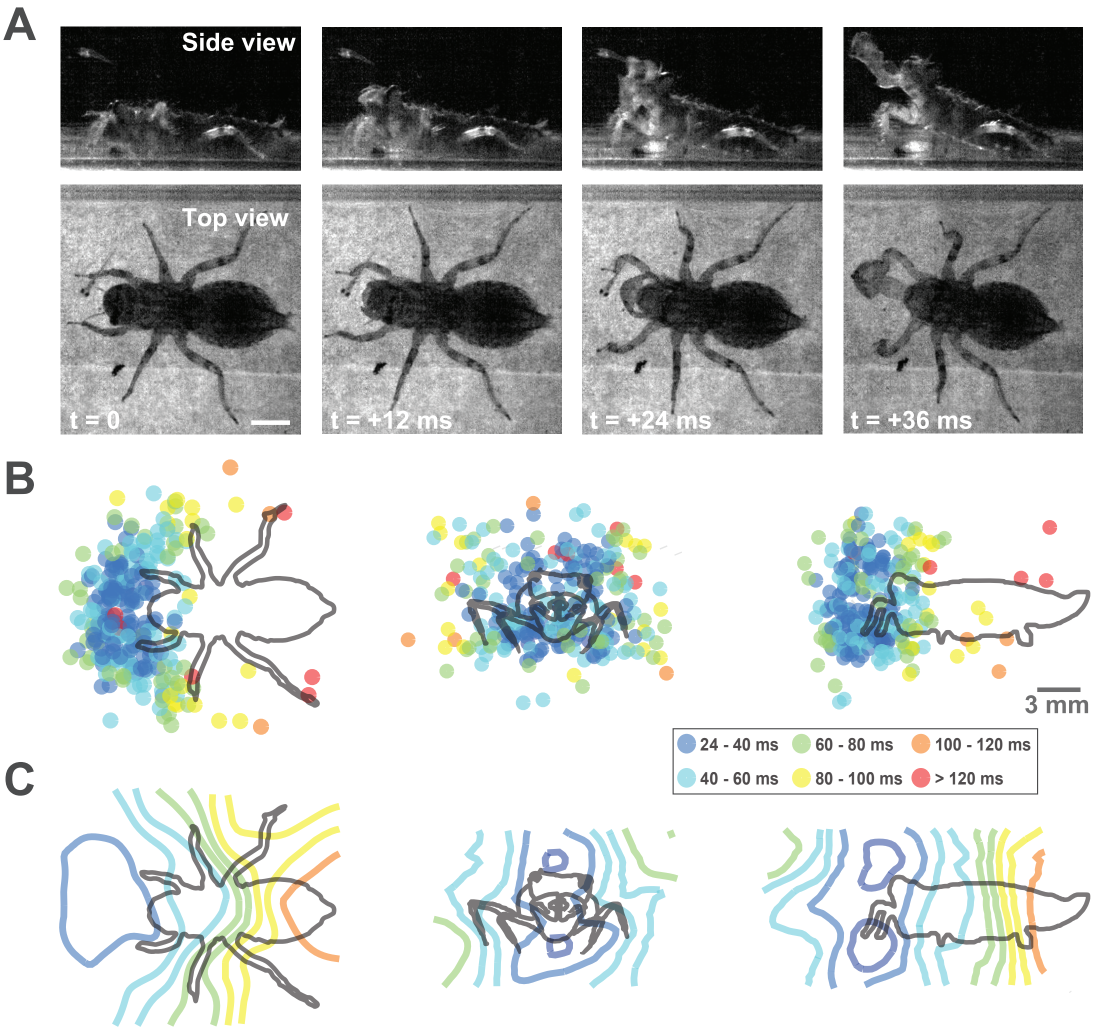

Figure 3.1. Dragonfly nymph prehensile mask motor volume.

strike. (Number of nymphs = 5, nymph body length mean ± std = 14.5 ± 1.3 mm, number of attacks = 159). C) Top, front, and side view cross-sections of surfaces representing isochrones for the duration of the strike from the time of initial movement detected thru high-speed videography. The 3-dimensional isochronic surfaces define the prehensile mask motor volume.

First, to quantify the biomechanical performance of the attack, we studied the duration of the predatory strike with respect to the furthest point reached by the prehensile mask in 3-dimensional (3D) space. The mask extension times ranged from 24–176 ms depending upon the location of the strike. The time needed for the mask to reach specific positions in space (Figure 3.1B) was well described by a k-nearest neighbor (k-NN) model ($R^2 = 0.7$, Figure 3.1C, see also Appendix) which served as a representation of the motor volume of the mask—the volume swept by the appendage over all strikes within a given amount of time Snyder et al. (2007). As seen in the cross-sections of the isochronic surfaces of the motor volume (Figure 3.1C), strikes directed towards lateral and caudal positions took more time than strikes directed medially and rostrally. This model represented the maneuverability of the mask, providing insight about the time-scale and directional bias of predatory strikes.

Next, to see how the outcome of the attack was influenced by aspects of the predatory encounter, we categorized the interactions. Successful and failed captures had distinct spatial distributions of the position of the fish before the attack (Figure 3.2A), where nymphs were more likely to capture larvae in closer proximity. Upon further examination, we found different kinds of failed and successful captures (Figure 3.2B). A failed capture could occur either due to an error in the predatory attack or an effective escape executed by the fish. A successful capture occurred either due to a fish not responding or an ineffective escape attempt by the fish. A formalization of these scenarios is illustrated as a process diagram of the predatory encounter in Figure 3.2B, which depicts the occurrence of these specific events that either terminate the process or lead to other events.

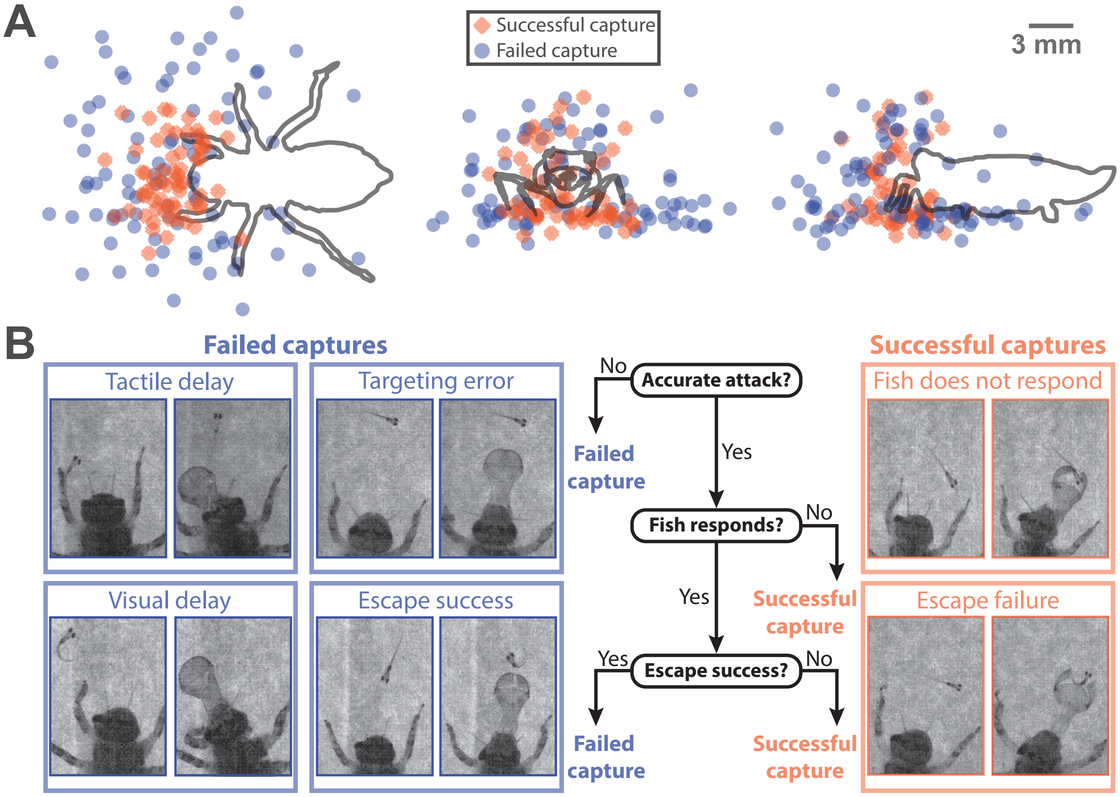

Figure 3.2. Causes of successful or failed captures by the nymph.

Figure 3.2 details: A) Top (x-y), front (y-z), and side (x-z) view orthographic projections of 3D initial fish positions before the start of the nymph's strike with points colored to represent the outcome of a successful or failed capture by the nymph. B) Process diagram demonstrating the sequence of events and causes of a successful or failed capture by the nymph with representative examples of each branching event in the process.

The first of these events is the attacking strike by the nymph. This can lead to a failed capture when the strike is inaccurate. This happened in some instances when the fish performed spontaneous swimming movements before the start of a predatory strike. In these cases, the dragonfly nymph would strike at positions where the fish was no longer

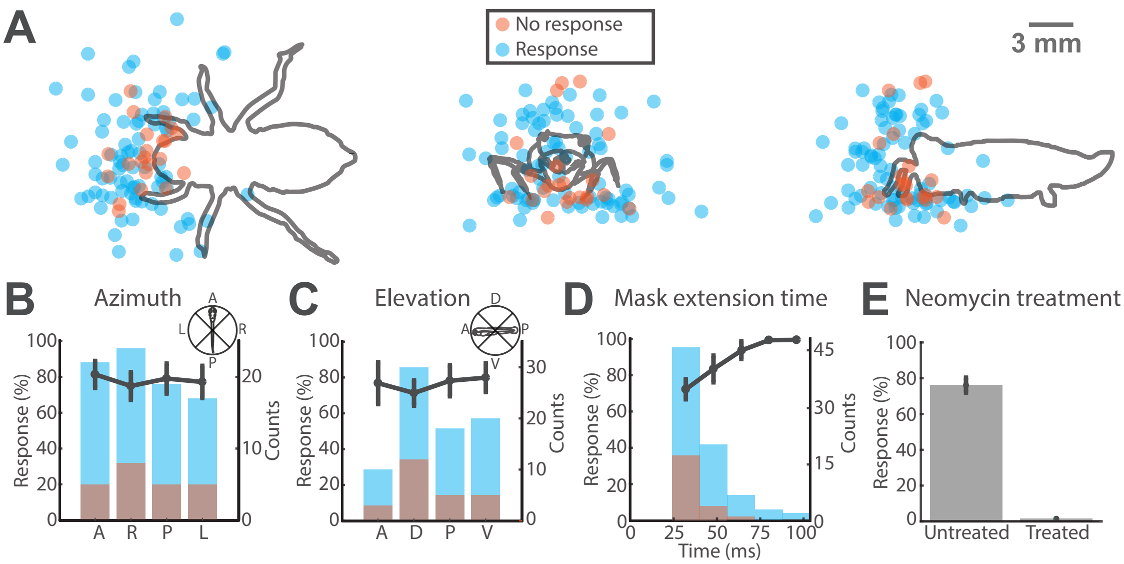

Figure 3.3. Likelihood of larval zebrafish response to an accurate strike.

present (Figure 3.2B, Tactile delay, Visual delay). This suggests that the nymph is not ballistically intercepting the prey by predicting its future location, but rather striking at the position of the prey before the attack began. Sometimes, the nymph also made targeting errors where the fish was stationary through the entire strike but the strike was aimed inaccurately (Figure 3.2B, Targeting error). While attack errors provide information about the sensorimotor limitations of the dragonfly nymph, they cannot help determine the relevant escape decisions of the fish that confer success. Thus, we focused the remainder of our analysis on the instances where the mask was correctly aimed at the position of the fish prior at the initiation of the attack.

3.3.2. Likelihood of a response from zebrafish larvae to accurate strikes

To investigate the sensorimotor performance of the fish in this predatory context, we studied the likelihood of a fish initiating an escape response given an accurate strike.

Figure 3.3 details: A) Top (x-y), front (y-z), and side (x-z) view orthographic projections of 3D initial fish positions before the start of an accurate strike with points colored to represent whether the fish responded. B–D) Heights of each bar represent the count of strikes within that bin (right y-axis) and the color represents whether the fish responded or not. The line plot shows the mean ± sem fish response probability for each bin (left y-axis, number of nymphs = 5 for all points with error bars). B) Fish response probability based on the azimuthal position of the nymph head with respect to the fish. There are no significant differences between response probabilities for each azimuthal quadrant (One-way anova, $p = 0.94$). C) Fish response probability based on the elevation of the nymph head with respect to the fish. There are no significant differences between response probabilities for each elevation quadrant (One-way anova, $p = 0.75$). D) Fish response probability based on the mask extension time to the fish position. The fish is significantly more likely to respond for longer extension times (One-way anova, $p = 0.01$). E) Compares overall response probability of neomycin treated fish with untreated fish (untreated fish: number of trials = 109, untreated fish: number of nymphs = 5, treated fish: number of trails = 61, treated fish: number of nymphs = 4). Neomycin treated fish are far less likely to respond to a strike than untreated fish (Mann-Whitney U test, $p = 0.003$).

The spatial distributions of the fish positions before the start of the predatory strike were different for scenarios where the fish responded or did not respond (Figure 3.3A). Fish with initial positions closer to the nymph mouth were less likely to produce a response (Figure 3.3A). The azimuthal or elevation position of the nymph mouth with respect to the fish had little or no influence over the response probability of the fish (Figure 3.3B and C). However, the fish was more likely to respond given longer mask extension times (Figure 3.3D). The reduced likelihood of responding to short extension times may be because fish were captured before the initiation of a response could begin. Regardless, since the response probability is consistently above 50%, fish were always more likely to respond than not respond.

To understand whether the larval fish were initiating escape responses only on the basis of flow stimuli or a combination of visual and flow stimuli, we tested the role of flow sensing by compromising the lateral line in a group of larvae with exposure to neomycin sulphate (see Appendix). This technique induces cell death in lateral line hair cells while leaving inner ear hair cells intact Harris et al. (2003); McHenry et al. (2009). To ensure recovery of larval zebrafish, we waited for 3 hours after neomycin treatment. Additionally, we monitored larvae to confirm that they performed spontaneous swimming movements and responded with escape maneuvers to touch stimuli before placing them in the arena with the nymph. All neomycin treated fish (n = 61) failed to respond to any strikes and were eventually successfully captured by accurate strikes (Figure 3.3E). These data suggest that fish generate escapes in this scenario largely on the basis of flow sensing and do so with high likelihood regardless of relative orientation and position with respect to the nymph.

To better understand how the perturbed fluid movement due to the strike influenced the larval zebrafish response (Figure 3.4A), we next tracked the 3D position of the mask for all strikes that produced an escape response in fish. The perturbed fluid velocity in water around a moving body, such as a sphere, is a function of the velocity of the body and the distance from the body (Figure 3.4B, see Appendix). To account for both velocity and distance when estimating the fluid flow experienced by fish, we used the mask velocity (Figure 3.4C) to estimate the perturbed fluid velocity over time at the initial fish position (Figure 3.4D). Since the distance to the initial fish position from the mask reduced over time as it extended, the perturbed fluid velocity at the initial fish position approached the velocity of the mask (Figure 3.4D).

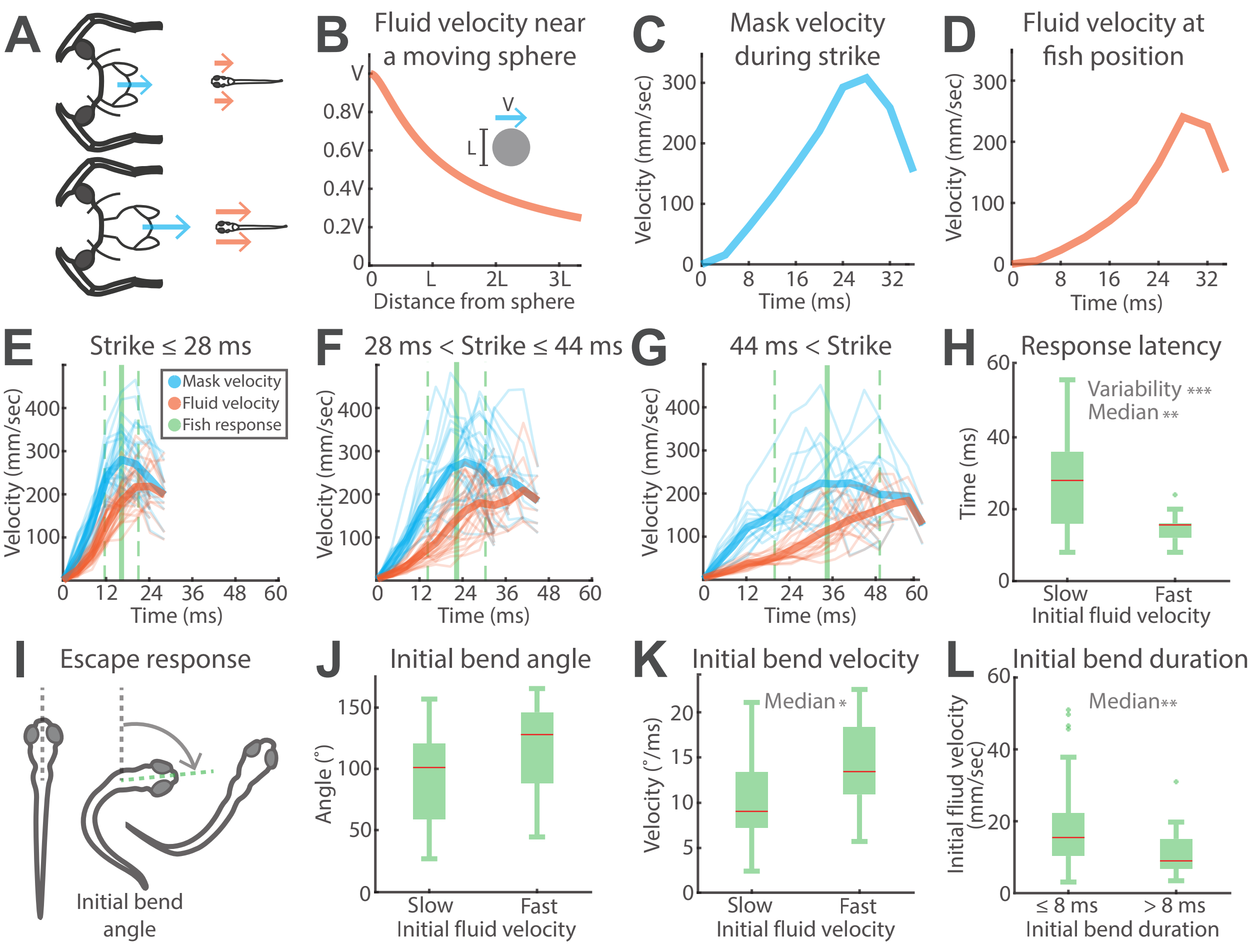

Figure 3.4. Larval zebrafish responding to fluid movement from the strike.

Figure 3.4 details: A) The mask velocity (in cyan) and the perturbed fluid velocity at the fish position (in orange) both change over the duration the strike. B) The perturbed fluid velocity at some distance from the edge of a sphere with diameter L moving at velocity V was estimated with the analytical solution for potential flow around a sphere. The fluid velocity at the fish position depends on both the mask velocity and the distance from the mask. C) A representative example of mask velocity during an accurate strike. D) The corresponding estimated fluid velocity at the initial fish position computed from the measured mask velocity and the potential flow approximation. E–G) Mask (cyan) and fluid velocity (orange) profiles of different strikes grouped by the mask extension time with the mean ± std of larval zebrafish response times (green). Lighter lines represent individual velocity profiles while bold lines represent the mean for each group. The bold green line is the mean response latency of larval zebrafish while the dashed green lines are one standard deviation above and below the mean (Strike $\leq$ 28 ms n = 27, 28 ms < Strike $\leq$ 44 ms n = 24, 44 ms < Strike n = 15). H) Larval zebrafish response latencies grouped by slow (first quartile) and fast (fourth quartile) fluid velocities at the fish position 0–4 ms after onset of the attack (n = 18 for both groups). Slow initial fluid velocities produced escape responses with significantly longer latencies (Mann-Whitney U test, $p = 0.002$) and more variable latencies (Levene's test, p = 0.0003). I) During the escape response, the fish changed heading direction with an initial bend and then swam away with propulsive swimming. The initial bend angle is the angle between the heading vector of the fish before the start of the escape response and the heading vector at the end of the initial bend. Responses where it was unclear whether the fish completed the initial bend before being captured were excluded from analysis of initial bend parameters. J) Initial bend angles of responses grouped by slow (first quartile) and fast (fourth quartile) fluid velocities at the fish position 0–4 ms after onset of the attack (n = 15 for both groups). There is no significant difference between the two groups (Mann-Whitney U test and Levene's test, all $p > 0.3$). K) The initial bend velocity of responses grouped by slow (first quartile) and fast (fourth quartile) fluid velocities at the fish position 0–4 ms after onset of the attack (n = 15 for both groups). Initial bend velocities of responses to fast fluid velocities are significantly higher than those to slow fluid velocities (Mann-Whitney U test, $p = 0.02$). L) Fluid velocity at the fish position 0–4 ms after onset of the attack grouped by initial bend durations $\leq$ 8 ms and > 8 ms ($\leq$ 8 ms n = 33, > 8 ms n = 24). Initial bend durations $\leq$ 8 ms occur in response to significantly higher initial fluid velocities at the fish (Mann-Whitney U test, $p = 0.008$).

Different mask extension times had different velocity and associated fluid velocity profiles (Figure 3.4E–G). The mean response latency of the fish and the variance of response latency both increased with increasing mask extension times (Figure 3.4E–G). We further investigated how larval zebrafish escape responses differed in response to the earliest fluid perturbations caused by the prehensile mask. Fish responded with shorter and less variable response latencies to the fastest quartile of fluid velocities computed between 0–4 ms after the onset of the attack (Figure 3.4H), hereafter referred to as the initial fluid velocity.

During the escape response, the fish changed heading direction with an initial bend and then swam away with propulsive swimming. To test whether the initial fluid velocities experienced by the fish influenced the kinematics of the escape response, we measured the bend angle (Figure 3.4I) for all responses where the fish clearly finished the initial bend. The bend angle was not significantly different between the fastest and slowest quartile of initial fluid velocities (Figure 3.4J). However, the fastest initial fluid velocities did produce responses with significantly faster bend velocities (Figure 3.4K). Since we recorded video at 250 fps (4 ms resolution), all initial bend durations recorded fell between 4–8 ms ($n = 33$), 8–12 ms ($n = 22$), or 12–16 ms ($n = 2$) after the onset of the escape. Escapes with shorter bend durations (≤ 8 ms) tended to be in response to significantly higher initial fluid velocities (Figure 3.4L). These data suggest that fish modulate their escape responses by deploying maneuvers with different latencies and kinematics based on the magnitude of the preturbed fluid velocity.

3.3.3. Larval zebrafish position, orientation, and escape direction

We next examined how the position and orientation of the fish at the start of the attack, along with its escape direction, influenced escape success. The spatial distribution of the

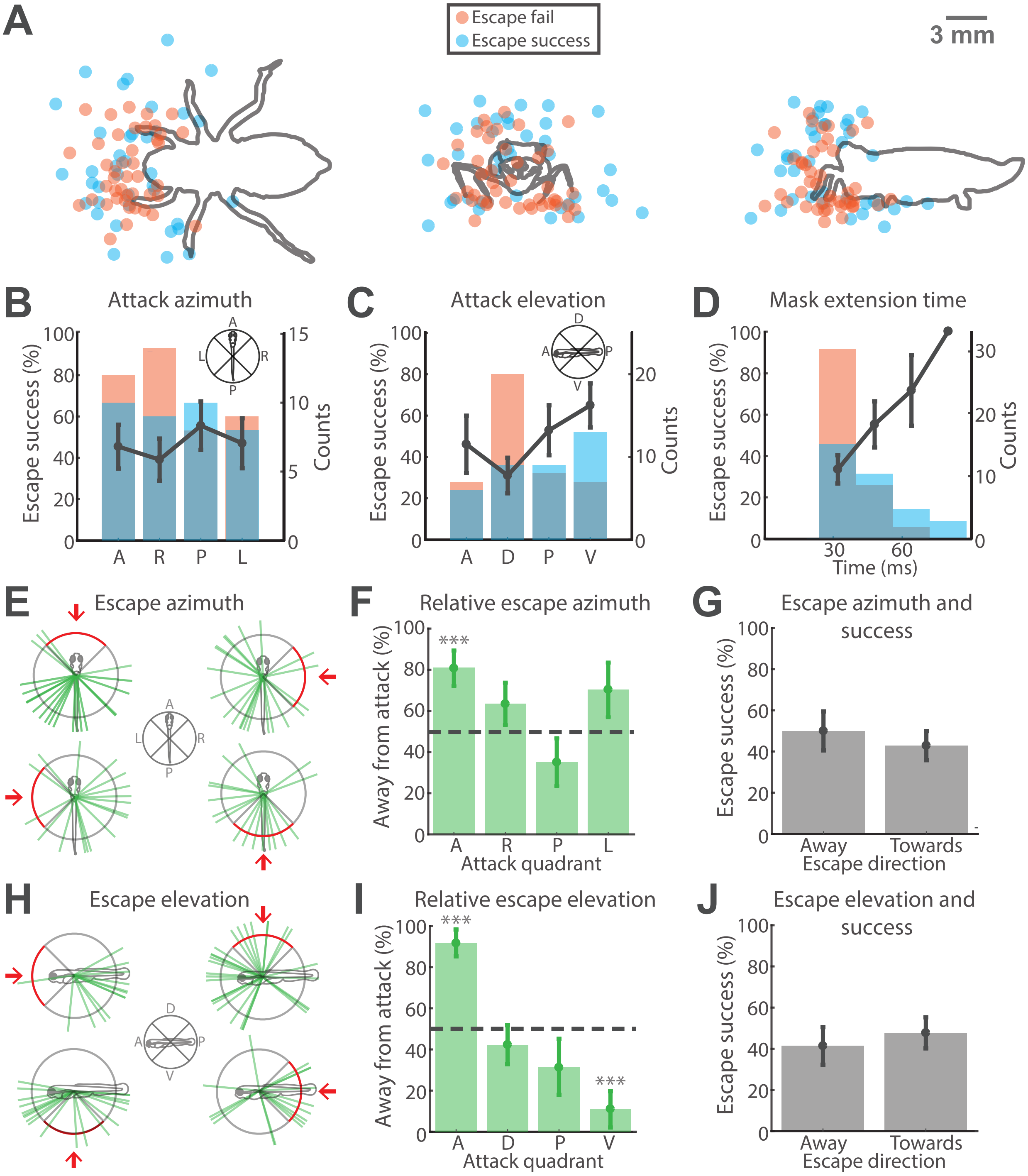

Figure 3.5. Larval zebrafish position, orientation, and escape direction.

fish positions before the start of the predatory strike for successful and failed escapes largely overlapped but failed escapes tended to happen closer to the nymph (Figure 3.5A). The azimuthal quadrant of the attack with respect to the fish had no significant influence on escape success probability (Figure 3.5B). However, fish were significantly more likely to execute successful escapes when responding to attacks from below (ventral, V) than from above (dorsal, D, Figure 3.5C). Moreover, fish were more likely to execute successful escape maneuvers in response to longer mask extension times (Figure 3.5D), which is consistent with the higher probability of escaping at further distances or with more time.

Figure 3.5 details: A) Top (x-y), front (y-z), and side (x-z) view orthographic projections of 3D initial fish positions before the start of an accurate strike with points colored to represent whether the fish escape response failed or succeeded in evading capture. B–D) Heights of each bar represent the count of strikes within that bin (right y-axis) and the color represents whether the fish escape failed or succeeded. The line plot shows the mean ± sem fish escape success probability for each bin (left y-axis, number of nymphs = 5 for all points with error bars). B) Fish escape success probability based on the azimuthal quadrant of the strike with respect to the fish. There are no significant differences in escape success probability with respect to attack azimuth. C) Fish escape success probability based on the elevation quadrant of the strike with respect to the fish. Fish escapes are significantly more likely to succeed when responding to attacks from quadrant V than from quadrant D (One-way anova, p = 0.001, Mann-Whitney U test, p = 0.005). D) Histogram demonstrating the fish escape success probability based on the mask extension time to the fish position. Fish escapes are more likely to succeed as mask extension times increase (One-way anova, p < 0.001). E) The azimuthal direction of fish escape represented by green lines and grouped by the azimuthal quadrant of the strike. F) Escape azimuth of fish relative to the azimuthal quadrant of the attack. The height of the bars represent the mean ± sem probability of fish escaping away to the opposite azimuthal hemisphere from the attack quadrant (number of nymphs = 5 for all groups). Asterisks represent significant difference from 50% (dashed line). G) The azimuthal direction of fish escapes grouped by whether the response was directed towards the opposite azimuthal hemisphere or towards the same azimuthal hemisphere containing the azimuthal quadrant of attack (mean ± sem, number of nymphs = 5 for both groups). There is no significant difference in escape success between responses with azimuthal directions towards or away from the strike azimuth (Mann-Whitney U Test, $p = 0.5$). H) The elevation direction of fish escape represented by green lines and grouped by the elevation quadrant of the strike. I) Escape elevation of fish relative to the elevation quadrant of the attack (number of nymphs = 5 for all groups). Asterisks represent significant difference from 50% (dashed line). J) The elevation of fish escapes grouped by whether the response was directed away from or towards the elevation direction of the strike (mean ± sem, number of nymphs = 5 for both groups). There is no significant difference in escape success between responses with elevation directions towards or away from the strike (Mann-Whitney U Test, $p = 0.73$).

We then analyzed escape direction with respect to the attack to determine whether fish escaped away from the attack and how it influenced escape success. Escape directions in the opposite hemisphere of the attack quadrant were considered to be away from the attack. When escape directions were grouped by the azimuthal or elevation attack quadrants (Figure 3.5E, H), fish did not consistently move away from the attacks. Escapes in response to attacks from the right (R), posterior (P), and left (L) azimuthal quadrants were not significantly biased away from the attack (Figure 3.5F). Similarly, escape directions in response to attacks from the dorsal (D) and posterior (P) elevation quadrants were not significantly biased away from the attack (Figure 3.5I). While fish did significantly bias their escape directions away from attacks in the anterior (A) azimuthal and elevation quadrants, this could be because escape movements typically involve a turn Bhattacharyya et al. (2017), especially those in response to attacks directed at the head O'Malley et al. (1996). The lack of consistent directional control was also illustrated by the fact that larvae would often escape in the direction of attacks occurring in the ventral (V) elevation quadrant (Figure 3.5I). Critically, whether fish escaped away or towards the attack had no significant influence on escape success probability (Figure 3.5G, J). However, escape trajectories toward the attack can occur along pitch or yaw angles that take the fish around the mask, thereby keeping the fish out of the capture zone.

Together these data suggest that the attack azimuth and the escape direction relative to the attack direction were not significantly related to escape success probability and, in some cases, escapes toward the attack were successful. Thus it seems more important that zebrafish move quickly rather than in the opposite direction.

3.3.4. Importance of time remaining at escape

Having found that the escape direction of the larval fish had no discernible influence on escape success, we next explored how the fish's response latency may have influenced the escape outcome. Surprisingly, the response latencies of successful and failed attacks were not significantly different (Figure 3.6A). To investigate how this discrepancy might be explained, we examined in more detail how response latency may interact with mask extension time. To do so, we defined the time left from the initiation of the fish escape response until the mask reaches the initial position of the fish as the time remaining at escape (Figure 3.6B). The time remaining at escape was dramatically different for successful and failed escapes

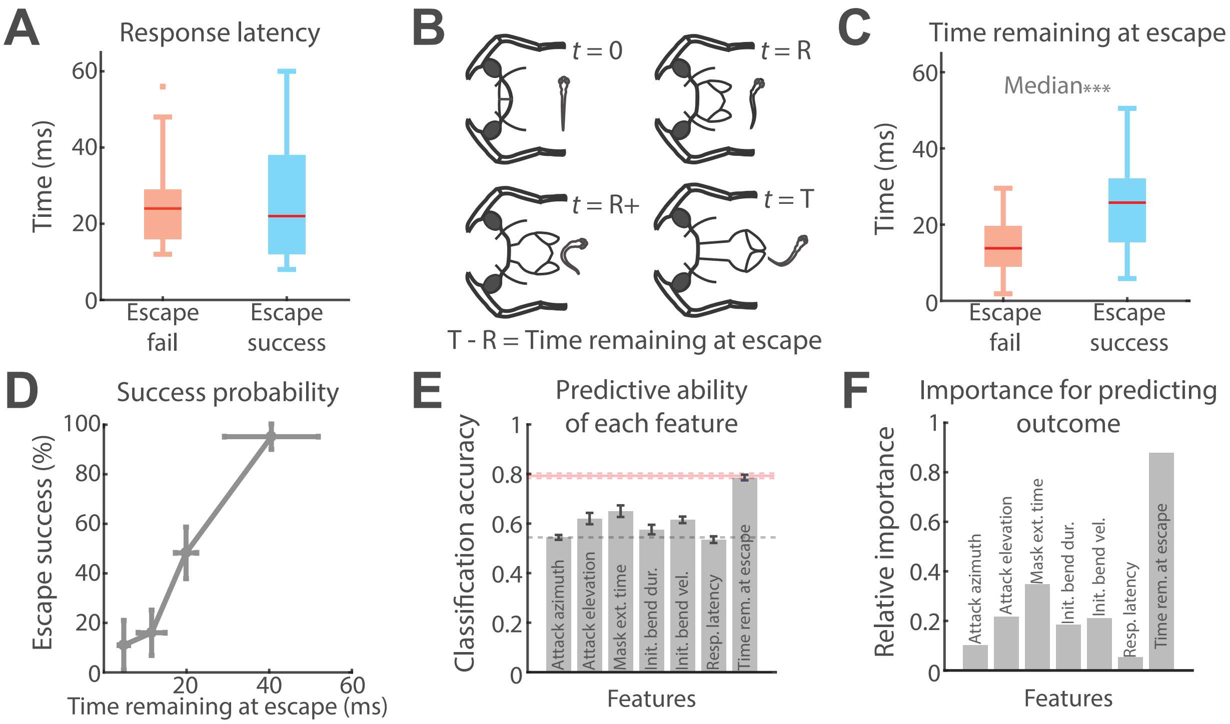

Figure 3.6. Importance of time remaining at escape.

(Figure 3.6C). Additionally, the escape success probability increased with increasing time remaining at escape (Figure 3.6D).

Figure 3.6 details: A) There is no significant difference between response latencies of failed and successful fish escapes (Escape fail n = 43, Escape success n = 37, Mann-Whitney U test, Levene's test, all $p > 0.8$). B) The time remaining at escape is the time at the start of the fish escape response (t = R) subtracted from the mask extension time (t = T). C) The time remaining at escape is significantly longer for successful escapes than for failed escapes (Escape fail n = 43, Escape success n = 37, Mann-Whitney U test, $p \lll 0.0001$). D) Escape success probability as a function of time remaining at escape binned into quartiles (mean ± std). Escape success probability increases with time remaining at escape (One-way anova, $p \lll 0.001$). E) Classification accuracy (mean ± sem) of random forest classifiers in predicting escape outcome when trained on only one parameter with 10-fold cross validation. The gray dashed line is the naive classification accuracy of 0.55 and the pink dashed line at 0.79 is classification accuracy of a random forest classifier trained on all of the parameters to predict the escape outcome. The classifier using only time remaining at escape significantly outperformed classifiers trained on any of the other parameters (pairwise Mann-Whitney U tests with Bonferroni correction, all $p < 0.005$) and is not significantly different from a classifier trained on all of the parameters together (Mann-Whitney U test, $p = 0.4$). F) The relative importance of parameters in a random forest classifier trained to predict escape outcomes using all parameters. Time remaining at escape is dramatically more important than other parameters.

To further investigate the interaction of escape maneuver parameters and which single parameter, if any, had the most influence on the outcome we trained different random forest classifiers with each parameter to predict escape success or failure (see Appendix). The parameters were the following: 1) attack azimuth; 2) attack elevation; 3) mask extension time; 4) bend duration; 5) bend velocity; 6) response latency; 7) time remaining at escape. Parameters known not to be related to escape outcome (attack azimuth and response latency) were included as controls along with kinematic parameters (bend duration and bend velocity) which had not yet been tested. Ten different classifiers were trained for each parameter by selecting 85% of the dataset (n = 68) each time for training and testing accuracy with the remaining 15% of the dataset (n = 12). This allowed for an estimate of the mean ± sem of accuracy for a classifier trained on each parameter.

A naive estimator which predicted that all escapes failed had a classification accuracy of 0.55 (grey dashed line Figure 3.6E). Any classifier trained on one of these parameters with a significantly higher classification accuracy suggested that the parameter had some influence on the outcome. The classifiers trained on attack elevation, mask extension time, bend velocity, and time remaining at escape had classification accuracies significantly different from the naive estimate. However, the classifier trained on time remaining at escape dramatically outperformed all other classifiers and was not significantly different from a classifier trained on all of the parameters together (pink dashed line Figure 3.6E). As a further test, a random forest classifier trained on all of the parameters together was used to determine which parameter was the most important in determining the model prediction (see Appendix). The importance of time remaining at escape as a parameter was dramatically higher than all other parameters in determining the model prediction (Figure 3.6E).

These data suggest that even though various parameters were correlated with escape outcome, the time remaining at escape was the best and most important predictor of the escape outcome (Figure 3.6E and F). Consistent with our real observations, in both models escape response latency had no discernible influence on escape outcome in this predatory interaction.

3.3.5. Fish motor volume in the time remaining

The time remaining at escape limits the volume of space that contains all possible trajectories of the fish (Figure 3.7A) before the mask reaches the initial position of the fish. This is the time-limited fish motor volume that quantifies the maneuverability of the fish Snyder et al. (2007). The visualization of the fish motor volume in Figure 3.7A was generated computationally (see Appendix) using the average bend velocity measured in this study (14°/ms) during the initial bend and the average swimming velocity during propulsion (0.12 $\frac{\text{mm}}{\text{ms}}$) measured in this study of and confirmed by others Budick and O'Malley (2000); Dunn et al. (2016). Using this model, we visualized the portions of the fish motor volume not engulfed

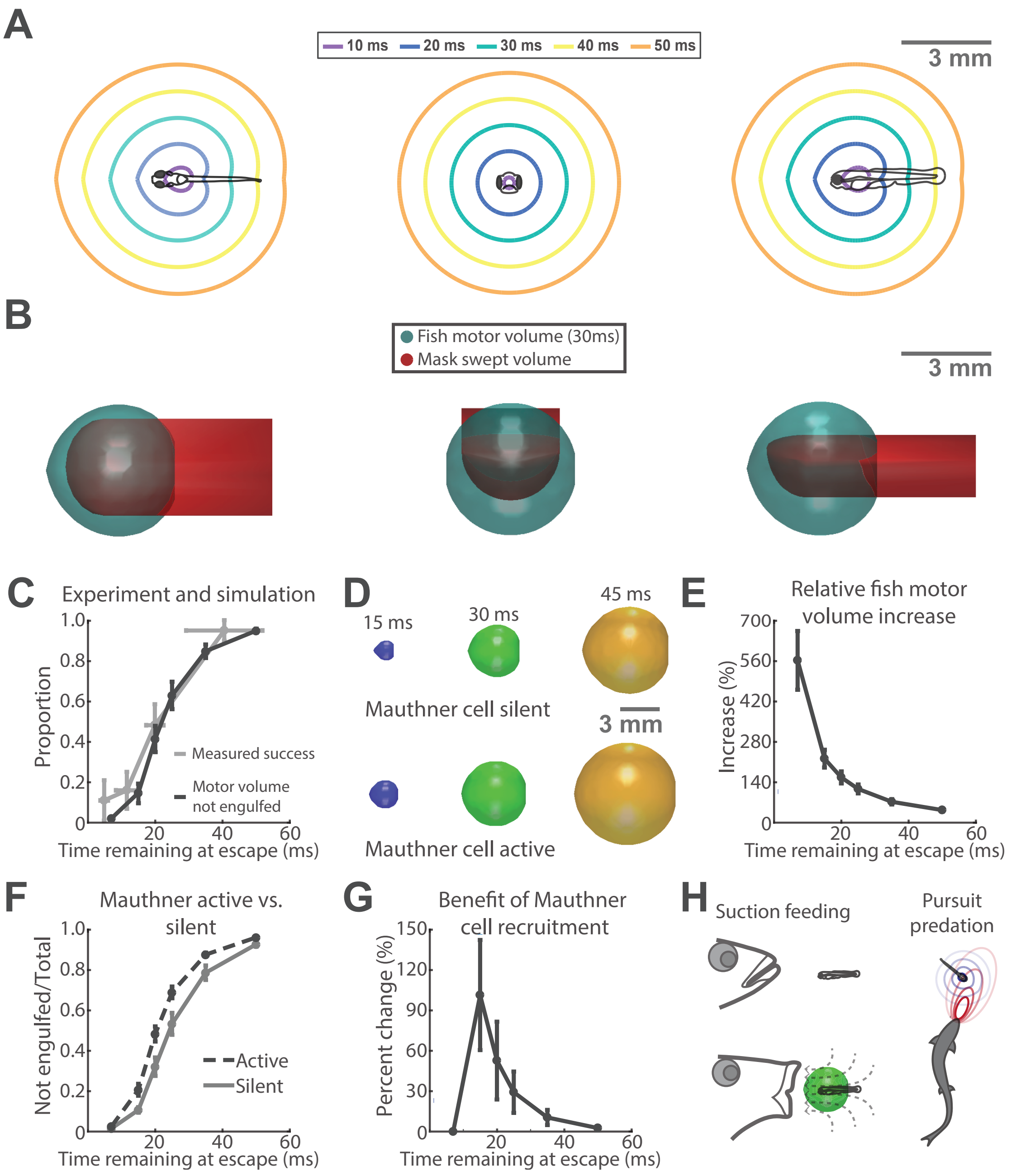

Figure 3.7. Fish motor volume in the time remaining.

by the swept volume of the mask (Figure 3.7B). The non-engulfed fraction of the fish motor volume represents the regions of space visited during a successful escape. We hypothesized that the importance of the time remaining at escape in determining the outcome was due to its direct influence on the fish motor volume and its intersection with the mask swept volume.

Figure 3.7 details: A) Top, front, and side view cross sections of surface isochrones of the larval zebrafish motor volume for times within the range of values for time remaining at escape. This larval zebrafish volume was computationally generated using the average initial bend velocity (14°/ms) in this study and a propulsive velocity of 0.12 $\frac{\text{mm}}{\text{ms}}$. B) Top, front, and side view perspectives visualizing the intersection of the mask swept volume with the larval zebrafish motor volume for the time remaining at escape of 30 ms. C) The darker line represents the proportion of the larval zebrafish motor volume not engulfed by the mask swept volume for different values of time remaining at escape (mean ± std). The lighter line represents the proportion of successful escape responses as a function of time remaining at escape binned into quartiles (mean ± std). The non-engulfed fraction of the motor volume increases with time remaining at escape (One-way anova, $p \lll 0.001$). An analysis of covariance test did not find a significant difference between the proportion of the motor volume not engulfed and the proportion of successful escape responses (slope $p = 0.4$, intercept $p = 0.2$). D) Visualization of the estimated larval zebrafish motor volume at different times remaining at escape for the Mauthner-silent and Mauthner-active responses. The initial bend velocity used to generate the motor volumes were different for Mauthner silent (10 $\frac{\circ}{\text{ms}}$) and active (18 $\frac{\circ}{\text{ms}}$) responses but the same propulsive velocity (0.12 $\frac{\text{mm}}{\text{ms}}$) was used for both. E) The relative increase in motor volume for different values of time remaining at escape when comparing Mauthner-silent to Mauthner-active volumes (mean ± sem). Larval zebrafish motor volumes were generated by pseudo-randomly sampling different initial bend velocities with uniform likelihood for Mauthner silent (10 ± 5 $\frac{\circ}{\text{ms}}$) and active (18 ± 5 $\frac{\circ}{\text{ms}}$) responses with 0.12 $\frac{\text{mm}}{\text{ms}}$ propulsive velocity for both. The increase in volume is greatest for shorter values of time remaining at escape. F) The proportion of the larval zebrafish motor volume not engulfed by the mask swept volume for different values of time remaining at escape for Mauthner silent and active responses (mean ± std). There is a significant difference in the proportion of the fish motor volume not engulfed for Mauthner active responses (Two-way anova, Mauthner recruitment $p < 0.001$, Time remaining at escape $p < 0.001$, Interaction = 0.2). G) The percent change in the proportion of the fish motor volume not engulfed when comparing Mauthner silent to active responses. The most dramatic increases are seen for mid-range values of time remaining at escape. H) Suction feeding: larval fish motor volume and predator ingested volume interaction during suction feeding. The ingested volume is similar to mask capture volume. Pursuit predation: predator and prey motor volume interaction during pursuit predation.

We used simulations to investigate how the fraction of the fish motor volume not engulfed by the mask volume corresponded to the escape success probability (Figure 3.6D). Fifty virtual larval zebrafish motor volumes were generated by pseudo-randomly sampling initial bend velocities measured in this study and using a propulsive velocity of 0.12 $\frac{\text{mm}}{\text{ms}}$ for values of time remaining at escape from 7–50 ms. These virtual motor volumes were intersected with virtual mask swept volumes attacking from different directions with respect to the fish to measure the proportion of the motor volume not engulfed by the mask (see Appendix). The increase in the proportion of the fish motor volume not engulfed with increasing time remaining at escape corresponded well to the increase in the measured escape success probability (Figure 3.7C). Moreover, an analysis of covariance demonstrated that the fraction of the motor volume not engulfed and the proportion of successful escape responses as a function of the time remaining at escape were not significantly different (slope p = 0.4, intercept p = 0.2).

We used the proportion of the fish motor volume not engulfed to computationally investigate the utility of recruiting the Mauthner cell in generating a response. Since the recruitment of the Mauthner cell is known to produce the fastest bend velocities Liu and Fetcho (1999); Burgess and Granato (2007); Bhattacharyya et al. (2017), we generated virtual Mauthner-active and Mauthner-silent fish motor volumes using different ranges of initial bend velocities but the same propulsive velocity, as used earlier (Appendix). The virtual Mauthner-active motor volumes were consistently larger than the virtual Mauthner-silent motor volumes for all times remaining at escape (Figure 3.7D). The greatest difference between the Mauthner-active and Mauthner-silent motor volumes were seen for the shortest times remaining at escape (Figure 3.7E). This is because the parameters for the Mauthner-active motor volume allowed the virtual fish to finish the initial bend earlier and start propelling away, which more rapidly increases the size of the motor volume.

Mauthner-active and Mauthner-silent motor volumes were also intersected with the swept volume of the nymph mask to compute the proportion of the fish motor volume not engulfed (Figure 3.7F, refer Appendix). The proportion of the Mauthner-active fish motor volume not engulfed was significantly different from the proportion of the Mauthner-silent motor volume not engulfed (Two-way anova, Mauthner recruitment $p < 0.001$, Time remaining at escape $p < 0.001$, Interaction $p = 0.2$).

To quantify the benefit of Mauthner cell recruitment at different times remaining at escape, we calculated the percent change in the proportion of the motor volume not engulfed from Mauthner-silent to Mauthner-active volumes (Figure 3.7G). Our simulations showed that Mauthner activation increased the proportion of the fish motor volume not engulfed by the mask by 30–100% on average for times remaining at escape of 15–25 ms. Times remaining at escape longer than 40 ms showed a reduced benefit of Mauthner cell recruitment since slower escapes would be equally effective in evading the mask's swept volume. Moreover, times remaining at escape shorter than 7 ms also had reduced benefit from recruiting the Mauthner cell since that amount of time is inadequate for the fish to move out of the mask swept volume.

This analysis demonstrates how simulations of prey motor volume and predator swept volume can be used to estimate the utility of recruiting specialized escape circuits in response to an attack. Moreover, the intersection of these volumes provides insight into how the time remaining at escape shapes the outcome of the predatory interaction. Also, it may clarify the lack of impact of response latency on escape success, since similar response latency values can be associated with different values of time remaining at escape.

3.4. Discussion

Our goal was to evaluate the determinants of successful escape maneuvers and the utility of recruiting the Mauthner neuron by analyzing the escape responses of larval zebrafish to attacks from dragonfly nymphs. We identify the time remaining for the dragonfly mask to reach the fish from the onset of the fish's escape response as the most predictive parameter for escape success. We call this parameter the time remaining at escape and explain its role in determining the volume of space that contains all possible trajectories of the fish—the fish motor volume. Using a computational approach, we estimate the fish motor volume for different times remaining at escape to quantify the fish's ability to evade the capture volume of the nymph—the volume swept by the mask. Additionally, we use this approach to calculate the utility of recruiting the Mauthner neuron for generating the escape by estimating the relative increase in escape success probability.

We argue that the time remaining at escape robustly determines the outcome since it serves as a limiting constraint on the possible trajectories of the fish, as visualized by the time-limited fish motor volume Snyder et al. (2007). This framework clarifies the influence of response latency, speed, and direction of an escape maneuver on evasion success. For the same time remaining at escape, faster escape speeds would increase the size of the fish motor volume and therefore, increase the proportion of the motor volume not engulfed by the capture volume of the predator. This explains the existing evidence in support of the benefit of fast speeds during escape Webb (1986); Walker et al. (2005). However, escape responses to slower predators that leave more time remaining at escape may not require fast escape speeds for successful evasion. This explains the evidence found in other studies against the need for fast escape speeds Fuiman et al. (2006); Soto et al. (2015); Nair et al. (2015).

Similarly, shorter escape response latencies for the same dragonfly mask extension times would increase the time remaining at escape. This would also increase the fish motor volume and thus, the non-engulfed fraction. Unexpectedly, we find that the response latency of larval fish was not significantly different for failed and successful escapes. We argue that this is due to the variability of dragonfly mask extension times where the same fish response latency can produce a successful escape in the case of longer extension time and a failed escape in the case of the shorter extension time. However, for scenarios where the duration of predatory strikes are more consistent, changes in the latency of escapes would produce measurable changes in evasion success, as seen in other studies Fuiman et al. (2006); Stewart et al. (2013); Nair et al. (2017).

Finally, specific escape directions that lead the fish out of the mask swept volume would lead to successful escapes. In our study, for longer times remaining at escape, we find that a number of directions in the nearly spherical motor volume of the fish led out of the capture volume of the dragonfly nymph. This result aligns with studies which find that successful escape trajectories are not required to follow a single optimal trajectory Domenici et al. (2011b). However, scenarios where the predator capture volume engulfs a large portion of the prey motor volume may leave only a subset of directions that successfully evade the attack. For such cases, the appropriate choice of escape direction would be vital to survival, as shown in modeling studies Howland (1974); Weihs and Webb (1984). In our data, when the mask engulfed a large portion of the fish motor volume for shorter times remaining at escape, fish had low survival rates possibly because their escapes were not directed away from the attacks.

Different predatory scenarios may change the relative importance of response latency, speed, direction, or even other parameters in producing successful escapes. However, here we unify the influence of these parameters on the escape outcome by clarifying their role in the generation of the critical non-overlapping regions of the predator and prey volumes.

We found that escapes were initiated in response to the flow stimulus of the mask extension as suggested by the dramatic reduction of response after neomycin treatment of fish. Even though the fluid flow caused by mask movement was critical in the initiation of the escape response, fish did not consistently escape away from the direction of the attack. The lack of correlation between the attack direction and escape direction aligns with existing findings of larval zebrafish escapes initiated by flow sensing Stewart et al. (2014).

However, our findings do indicate that the magnitude of the fluid perturbation influenced the escape response. Faster fluid velocities due to mask movement produced shorter latency escape responses, with faster initial bends, and shorter initial bend durations. These escape kinematics suggest that fish were more likely to recruit the Mauthner cell in response to higher magnitude fluid perturbations. The argument for differential Mauthner cell recruitment based on stimulus parameters is well supported by previous findings which show that fish perform a graded assessment of threat Bhattacharyya et al. (2017).

Using simulations of fish motor volume and mask swept volume intersections, we were also able to estimate the utility of recruiting the Mauthner cell for an escape maneuver. Since the recruitment of the Mauthner cell generates responses with the highest initial bend velocities Liu and Fetcho (1999); Burgess and Granato (2007); Bhattacharyya et al. (2017), we compared Mauthner-active with Mauthner-silent motor volumes generated with different bend velocities. Our simulations showed that Mauthner activation dramatically increased the proportion of the fish motor volume not engulfed by the mask for a specific range of times remaining at escape from 15–25 ms. Since this range composes a significant proportion of the experimentally observed range of times remaining at escape, there is a clear functional benefit of recruiting the Mauthner neuron in this predatory context.

However, our simulations also suggested a reduced benefit from recruiting the Mauthner cell for larger values of time remaining at escape because motor networks producing slower movements would be equally effective. This result aligns with existing findings which demonstrate that fish are less likely to deploy a Mauthner active escape in response to slower approaching predators that will take longer to reach the fish Eaton et al. (1984); Bhattacharyya et al. (2017). Surprisingly, there was also reduced benefit from recruiting the Mauthner cell for very small values of time remaining at escape since these values do not allow for enough time to maneuver out of the predator capture volume. This potentially explains freezing behavior in cases where there is not enough time to escape Chelini et al. (2009); Egan et al. (2009); Herberholz and Marquart (2012); Bhattacharyya et al. (2017).

Our results extend directly to aquatic suction feeding (Figure 3.7H) since the volume ingested by the predator is analogous to the mask swept volume. Moreover, the ingested volume changes in time Higham et al. (2006) creating a flow stimulus that initiates the escape response Stewart and McHenry (2010) and leaves some time remaining after escape until the total volume is ingested. The prevalence of suction feeding in a wide variety of fish Wainwright et al. (2007) indicates that the framework presented here fits a wide array of aquatic predatory interactions.

For prey, the time remaining at escape is related to the speed of the predatory attack at the moment the attack is sensed. Though it is unclear whether animals estimate this parameter for flow stimuli, studies using looming objects suggest that animals do estimate the time remaining to capture for visual stimuli Rind and Simmons (1999); Santer et al. (2006); Liu et al. (2011b). Conceivably, faster attacks that produce more intense sensory stimuli push the estimates of time remaining to lower values. These estimates of time remaining directly correspond to the utility of deploying different escape maneuvers. This aligns with existing evidence of more intense stimuli producing shorter latency and higher speed escape responses in other animals Edwards et al. (1999); von Reyn et al. (2014). Given the importance of time remaining in predicting the escape outcome, the evidence that prey estimate this parameter, and its ability to determine the utility of different escape responses, we expect that time remaining at escape is a major driver of decision-making and a source of significant selection pressure.

More generally, comparing predator and prey motor volumes provides a method to quantify the maneuverability of each agent through the predatory interaction. This also applies to pursuit predation (Figure 3.7H) where the motor volumes change over time as predator and prey attempt to outrun and out-maneuver each other Moore and Biewener (2015). The regions of the prey motor volume not intersecting with the predator engulfing volume denote the subset of movements and corresponding neural circuits that constitute successful evasive strategies. This subset has clear implications for decision-making during escape and the evolutionary pressure on the selection of appropriate maneuvers to increase survival. The approach presented here provides a unified vision of predatory interactions and the utility of specific maneuvers by connecting the interplay of many temporal and kinematic parameters to their influence in shaping the reachable spaces of predator and prey.

CHAPTER 4

The consequences of visual acuity on the looming-evoked response

4.1. Overview

An unpredictable environment, the resolution limits of sense organs, and the molecular mechanics of neural sensors make noise an inescapable part of the sensorimotor transformations animals use to choose appropriate behavioral responses. Since the selection pressures on choosing the appropriate response is severe when escaping from predators, investigating escape responses may provide important insight into the influence of noise on behavior. Here, we computationally investigated the consequences of the uncertainty introduced by the visual acuity limit on escape behaviors in response to looming predators. The principal thesis of the mechanism mediating looming-evoked responses specifies that animals use the angular size of the looming object on the eye and its expansion rate to compute a higher-order variable called η that approximates the excitatory drive to premotor circuits. Using the larval zebrafish as a model, we calculated η from the estimates of angular size and expansion rate computed from noisy measurements representing the limits of visual acuity for the larval fish. We demonstrate how considering the impact on η from the uncertainty due to visual acuity can include previously unexplained results of behavioral variability and graded responses in looming-evoked escapes. Furthermore, since η is hypothesized to approximate the excitatory drive to premotor regions, we used our calculations of η as the current injection to a computational model of the Mauthner cell, the specialized neuron in these fish devoted to producing escape responses. Through this approach, we found that we could replicate the experimentally observed timing and patterns of Mauthner cell recruitment to varying predator approach rates. Based on our findings, we argue that mechanistic models of animal behavior can be expanded by understanding of how ineliminable noise in the nervous system might serve a functional role in producing behavioral responses.

4.2. Introduction

Animals must frequently act on uncertain and noisy sensory data. Conceivably, the pressure to act is highest when responding to an attack. In many animals, the decision to escape from an attack can be attributed to the activation of large diameter command-like neurons devoted to producing the shortest latency escapes with the fastest speeds Tanouye and Wyman (1980); Will (1991); Libersat (1994); Edwards et al. (1999); Korn and Faber (2005). To generate successful escapes, the recruitment of these specialized neurons needs to be optimally timed, resistant to false positives, and false negatives Yager (2012). However, it is unclear how uncertainty and noise in the sensory percept of a threat influences the recruitment of these giant neurons and the resulting escape behavior.

Here we investigated this question using the looming stimulus—the expansion of an image simulating a predator approaching at a constant velocity Fotowat and Gabbiani (2011). Animals with giant neurons are known to recruit these neurons when escaping in response to the looming stimulus Santer et al. (2006); von Reyn et al. (2014); Bhattacharyya et al. (2017). Studies of looming-evoked responses have shown that animals initiate escapes when the looming object reaches a certain angular size on the eye regardless of the approach rate Rind and Simmons (1999); Yamamoto et al. (2003); Oliva et al. (2007); Card (2012). The current understanding of the mechanism driving this behavior is that the brains of animals use the angular size and expansion rate of the stimulus to compute a higher-order variable called η Hatsopoulos et al. (1995); Sun and Frost (1998); Gabbiani et al. (1999); Wu et al. (2005). This variable reaches its maximum at the same time with respect to the critical angular size at response regardless of the approach rate and approximates the excitatory drive to motor circuits when animals are presented with looming stimuli Sun and Frost (1998); Gabbiani et al. (1999); Preuss et al. (2006); de Vries and Clandinin (2012).

However, responses to looming stimuli have some results that cannot be explained under this paradigm. Repeated presentations of the same looming stimulus in controlled settings produces escape responses at different times Fotowat and Gabbiani (2007); von Reyn et al. (2014); Temizer et al. (2015); Dunn et al. (2016). This variability in the timing of responses increases for looming stimuli with slower approach rates von Reyn et al. (2014); Dunn et al. (2016); Bhattacharyya et al. (2017). Furthermore, the same looming stimulus can stochastically produce escape responses with or without the activation of giant neurons von Reyn et al. (2014); Bhattacharyya et al. (2017) resulting in escape maneuvers with distinct kinematics for each case. The probability of a giant neuron mediated escape is graded and decreases for escapes in response to slower looming stimuli von Reyn et al. (2014); Bhattacharyya et al. (2017). Moreover, in larval zebrafish, escapes with giant neuron activation tend to happen closer to the onset of the stimulus than escapes without giant neuron activation for repeated presentations of the same looming stimulus Bhattacharyya et al. (2017).

Here, we used computational methods to extend the calculation of η to include these unexplained results by taking into account the noise in the measurement of angular size. With the larval zebrafish as an example, we modeled the uncertainty in the measurement of angular size due to the visual acuity limit, as measured in a previous study Haug et al. (2010). We performed recursive Bayesian inference to estimate the angular size and expansion rate of looming stimuli from noisy measurements and used these estimates to compute

η. By only considering the impact on calculations of η from the uncertainty due to visual acuity limits, we computationally reproduced 1) the variability in the timing of responses to looming stimuli, 2) the changing probabilistic recruitment of the giant neurons in fish—called Mauthner cells—as a function of the looming rate and 3) the earlier recruitment of Mauthner cell mediated responses to the same looming stimulus. We found our computational results to be in good agreement with existing data on looming-evoked responses from larval zebrafish Bhattacharyya et al. (2017).

Surprisingly, we show that accounting for noise in the sensory input can resolve previously unexplained results of behavioral variability—a feature of behavior that is thought to contribute to fitness Driver and Humphries (1970); Riechert (1978); Edut and Eilam (2004); Domenici et al. (2011a); Jones et al. (2011); Hitchcock et al. (2015). Our findings provide suggest that the sources of noise and the methods of compensating for them might interact to serve functional roles in producing behavior Faisal et al. (2008). We discuss future experiments to test and extend our computational findings. Finally, we argue that inclusion of environmental noise and systemic noise in the sensorimotor transformations of the organism can expand neuro-ethological models.

4.3. Results

4.3.1. The parameters of the looming stimulus

Figure 4.1 details: A) The looming stimulus is the expansion of an object of length L and velocity V over time simulating an approaching predator. B) The angular size of the expanding object increases with time where the rate of expansion depends upon the length and velocity of the virtual object ($\frac{L}{V}$, Eq. 4.1). Animals are known to escape near a critical angular size (horizontal dashed line) which occurs at different

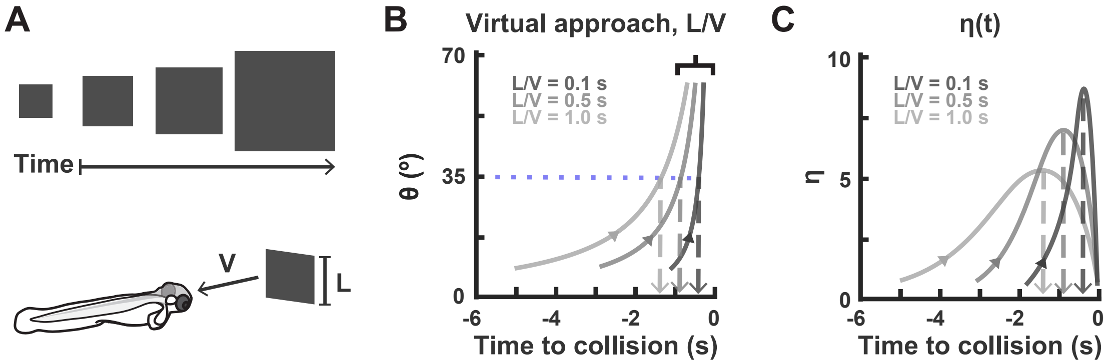

Figure 4.1. The looming stimulus.

times to collision (vertical dashed lines) for different expansion rates corresponding to $\frac{L}{V}$ values. C) The higher order variable $\eta(t)$ computed from the instantaneous angular size and the expansion rate (Eq. 4.2) reaches its maximum value for all expansion rates at the time when the object reaches the critical angular size.

Before understanding how a looming-evoked response may be changed by noisy sensory data, we must start by characterizing the parameters of the looming stimulus incident upon the sensory organs of the animal. The looming stimulus is an expanding image simulating an approaching object of size L and velocity V on a collision course with the animal (Fig. 4.1A) Hatsopoulos et al. (1995); Sun and Frost (1998). The angular size of the looming object on the eye increases with time as a function of the looming rate, $\frac{L}{V}$ (Eq. 4.1, Fig. 4.1B) Sun and Frost (1998); Gabbiani et al. (1999).

$$\theta(t) = 2 \times arctan(\frac{L}{V} \times -\frac{1}{2t}) \tag{4.1}$$

Under this paradigm, higher values of $\frac{L}{V}$ produce more gradual expansion rates with time $t = 0$ being the time of virtual collision (Fig. 4.1B). Studies have found that animals initiate escapes in response to looming stimuli when the object reaches a certain angular size on the eye (e.g. blue horizontal dashed line Fig. 4.1B) Rind and Simmons (1999); Yamamoto et al. (2003); Oliva et al. (2007); Card (2012). This critical angular size threshold corresponds to different times remaining to collision for each curve of angular expansion representing different values of $\frac{L}{V}$ (Fig. 4.1B).

The brains of animals are thought to compute a value named η that is calculated from the angular size $\theta(t)$ and expansion rate $\dot{\theta}(t)$ (Equation 4.2) Hatsopoulos et al. (1995); Sun and Frost (1998); Gabbiani et al. (1999).

$$\eta(t) = C \times \dot{\theta}(t) \times e^{-\alpha\theta(t)} \tag{4.2}$$

The maximum value of $\eta(t)$ is reached at the time corresponding to the same angular size for all looming rates $\frac{L}{V}$ (Fig. 4.1C) Gabbiani et al. (1999); Fotowat and Gabbiani (2011). The specific angular size of the looming stimulus at the maximum value of $\eta(t)$ is determined by the constant α (Fig. C.1). The other constant C has no influence over the timing of the maximum value but instead, serves to scale the entire function by a multiple. Hereafter, we will always have $C = 1$ for simplicity. Studies have found neural correlates of $\eta(t)$ Sun and Frost (1998); Fotowat and Gabbiani (2011); Dunn et al. (2016) which are thought to constitute the excitatory drive to premotor regions in animals presented with looming stimuli Gabbiani et al. (1999); Preuss et al. (2006); de Vries and Clandinin (2012). The framework and the equations provided above define the parameters of the looming stimulus relevant to the sensory processing and escape decisions of an animal.

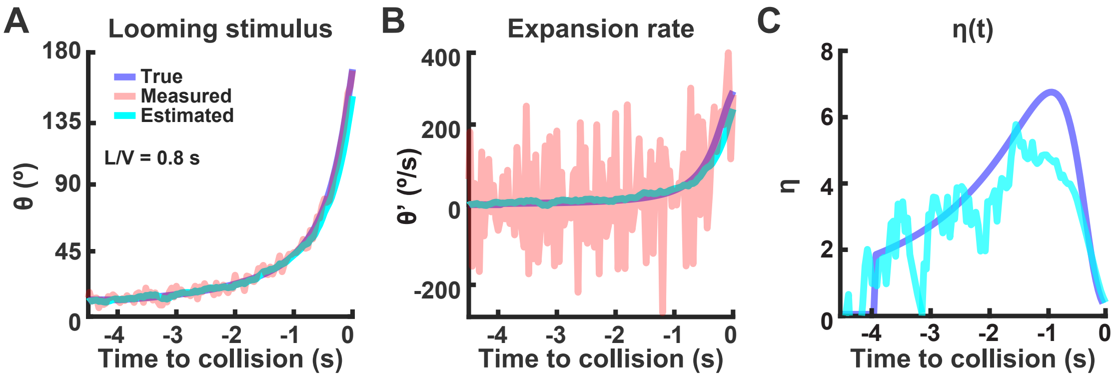

Figure 4.2. Estimating the looming stimulus properties.

4.3.2. Perceptual inference of looming stimulus parameters

Even though we have defined the parameters of the looming stimulus with mathematical accuracy, the perception of the changing angular size of the stimulus is mediated through the eye which has limits of spatial and temporal resolution. To account for this discrepancy between the analytical and measured signals, we used the angular visual acuity of the eye as a measure of the spatial resolution and the flicker fusion frequency as a measure of the temporal resolution. The eyes of the larval zebrafish at 5–7 days-post-fertilization (dpf) are known to have a visual acuity of 3.1° Haug et al. (2010) and a flicker fusion frequency of 25 Hz Seeliger et al. (2002). Therefore, we represented the angular size of the looming stimulus as measured by the eye of the larval zebrafish by sampling the true angular size (Eq. 4.1) at the flicker fusion frequency and added Gaussian noise with ±3.1° standard deviation (Fig. 4.2A). We call this the measured angular size and treated it as a representation of the sensory information available to the larval zebrafish. This computationally approximated the perception of the looming stimulus as a succession of noisy measurements of angular size (Appendix).

Figure 4.2 details: A) Comparison of the true angular size of an expanding object at $\frac{L}{V} = 0.8$ s with the measured angular size sampled at the flicker fusion frequency of larval zebrafish (25 Hz) with added noise (±3.1°) to represent limits of visual acuity. This noisy measured angular size is used to compute a less noisy estimate of angular size through Kalman filtering (Appendix). B) Comparison of the true expansion rate with the measured expansion rate computed by taking the difference of successive noisy measured angles and the estimated expansion rate through Kalman filtering. The Kalman-filtered expansion rate is far more stable than the measured expansion rate. C) Comparison of the true η(t) with the estimated η(t) computed with Kalman-filtered angular size and expansion rate. The calculation of η(t) with directly measured noisy values of angular size and expansion rate are not included due to the high level of noise (orders of magnitude in scale) in the resulting function.

Arguably, the nervous system of the larval zebrafish uses this stream of noisy sensory information to compute stable estimates of angular size and expansion rate in real-time. Though the neural implementation of this computation remains to be discovered, recursive Bayesian estimation provides the general mathematical framework for computing an estimate of the most likely value of a variable in real-time from a sequence of noisy incoming measurements Särkkä (2013). Furthermore, Bayesian estimation has been implicated and explored extensively within the context of sensorimotor decision-making Doya et al. (2007); Kording (2007). Specifically, we use a Kalman filter, which is a Bayes optimal estimator Kovvali et al. (2013), to compute estimates of the angular size and expansion rate in real-time (Appendix).

The Kalman-filtered estimate of angular size was far less noisy than the measured angular size and was in good agreement with the true angular size (Fig. 4.2A). The expansion rate computed with a forward difference between successive values of the noisy measured angular size was far too unstable to be useful is any downstream calculations (Fig. 4.2B). Conversely, the estimated expansion rate from Kalman filtering was a lot less noisy (Fig. 4.2B). We take this as further evidence for the need of recursive estimation to compute stable estimates of variables.

Nonetheless, the Kalman-filtered estimate of the angular size and the expansion rate did underestimate the true values for both measures (Fig. 4.2B). The underestimation of the expansion rate is due to the difficulties of numerically estimating derivatives from noisy signals, especially those of an infinitely differentiable function like that in Equation 4.1 Liu et al. (2011a) (Appendix). Underestimation of the expansion rate led to underestimation of the angular size as well.

To see how η was influenced by the recursive estimation from noisy data, we calculated $\eta(t)$ (Eq. 4.2) from the Kalman-filtered estimates of angular size and expansion rate. The value for the constant α—needed to compute $\eta(t)$—was fit using behavioral data from larval zebrafish Bhattacharyya et al. (2017) so that $\eta(t)$ reached its maximum value corresponding to the critical angular size when larval zebrafish initiated escape responses (Fig. C.1, Appendix). We compared the calculation of $\eta(t)$ from the Kalman-filtered estimates of angular size and expansion to the $\eta(t)$ calculated from the true angular size and expansion rate, hereafter referred to as the true $\eta(t)$. The calculation of $\eta(t)$ from the estimates reaches its maximum value at a different time but is in fair agreement with the true $\eta(t)$ (Fig. 4.2C). A calculation of $\eta(t)$ directly from the noisy measured angular size and expansion rate was not included in the figure since the resulting function was extremely unstable and agreed poorly with the true $\eta(t)$.

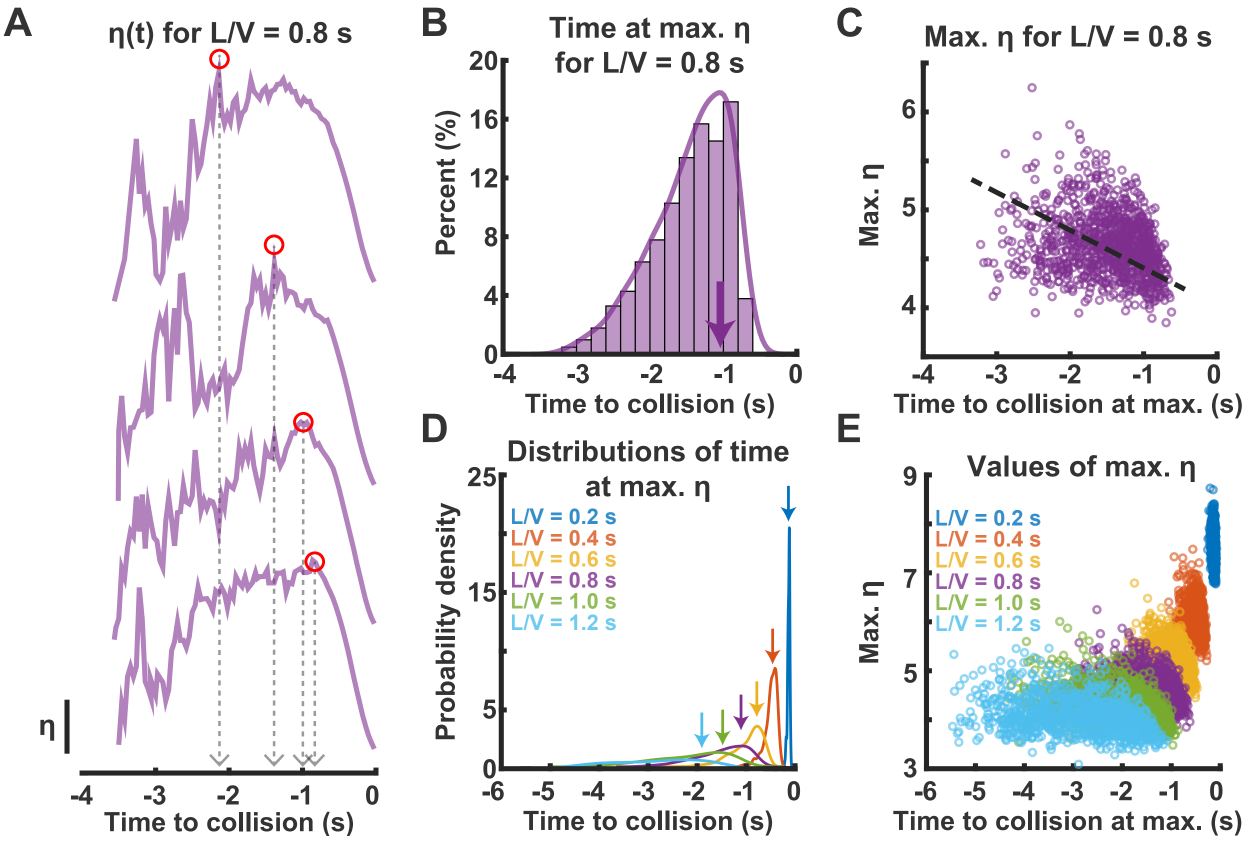

Figure 4.3. Maximum values of $\eta(t)$.

Overall, these results show how the noisy measured angular size can be used to compute far less noisy estimates of angular size and expansion rate in real-time. Moreover, the calculation of $\eta(t)$ from recursive estimates of angular size and expansion rate is in fair agreement with the true $\eta(t)$. Conversely, a calculation of $\eta(t)$ from the noisy measured values is not feasible due to the severe instability of the expansion rate computed directly from the measured angular size (Fig. 4.2B).

4.3.3. Time at maximum $\eta(t)$ and comparison to looming-evoked responses

Figure 4.3 details: A) Multiple simulated presentations of a looming stimulus with $\frac{L}{V}$ = 0.8 s produced estimates of $\eta(t)$ that reached their maximum value at different times to collision (vertical scale: = 1). B) One thousand simulated presentations of $\frac{L}{V}$ = 0.8 s provided the distribution of times to collision when the corresponding estimates of $\eta(t)$ reached their maxima. The times at maximum estimated η are distributed over the duration of the looming stimulus but the peak of the distribution coincides with the time of maximum for the true $\eta(t)$ (arrow) as expected from responses of larval zebrafish. C) Maximum values of η plotted against the time at maximum η. Maxima happening earlier in time tended to have higher maximum η values (Pearson's correlation, p-value < 0.0001, n = 1000) D) Multiple simulated presentations of a set of $\frac{L}{V}$ values provided the distribution of times at maxima η for each value. The variability in times at maximum η increased for increasing $\frac{L}{V}$ values but the peaks of the distributions coincided with the times of maximum for the true $\eta(t)$ for each $\frac{L}{V}$ value (arrows). E) The pattern of higher maximum η values occurring earlier from collision held true for all $\frac{L}{V}$ values except one (Pearson's correlation, $\frac{L}{V}$ = 0.2 s p-value = 0.21 , $\frac{L}{V}$ = 0.4 s p-value < 0.001 , $\frac{L}{V}$ = 0.6 s p-value < 0.001 , $\frac{L}{V}$ = 0.8 s p-value < 0.001 , $\frac{L}{V}$ = 1.0 s p-value < 0.001, $\frac{L}{V}$ = 1.2 s p-value < 0.001, n = 1000 for all $\frac{L}{V}$ values).

Since the time when $\eta(t)$ reaches its maximum value is thought to have a direct consequence on the timing of the looming-evoked response, we sought to understand how calculating $\eta(t)$ from estimates of $\theta(t)$ and $\dot{\theta}(t)$ would influence the time at maximum η. To this end, we used multiple simulated presentations of $\frac{L}{V}$ = 0.8 s as a representative looming rate to compute $\eta(t)$. For different presentations of the same looming rate, estimates of $\eta(t)$ reached their maximum values at different times (Fig. 4.3A). The histogram of times at which estimates of $\eta(t)$ reached their maxima ranged over the entire duration of the stimulus presentation (Fig. 4.3B). We estimated the density of the distribution using kernel density estimation (purple solid line, Appendix). Critically, the peak of the distribution coincided with the time when the true $\eta(t)$ reached the maximum value—the time at the critical angular size (arrow Fig. 4.3B). This suggests that the Kalman filtering process before computing $\eta(t)$ still produces maxima of η near the expected value.

To examine if there was a trend between the maximum value of η and the time when it reached that maximum value, we plotted the time at maximum η against the maximum value of η (Fig. 4.3C). The maximum value of η tended to be larger when $\eta(t)$ reached its maximum earlier from collision (Fig. 4.3C). Since $\eta(t)$ corresponds to the excitatory drive to premotor circuits, higher maxima occurring earlier from collision may have implications for the timing and recruitment of escape circuits.

We repeated these simulations over an ethologically relevant range of $\frac{L}{V}$ looming rates for larval zebrafish from 0.2–1.2 s Stewart et al. (2013); Dunn et al. (2016); Bhattacharyya et al. (2017) to test if we could observe similar patterns. The time at maximum had some variability for all $\frac{L}{V}$ values (Fig. 4.3D) but the peak of the distributions coincided with the time when the true $\eta(t)$ reached the maximum value for each $\frac{L}{V}$ looming rate (arrows Fig. 4.3D). The variability in the timing of maximum η increased for more slowly looming stimuli. Moreover, the pattern of higher maxima of η tending to happen earlier from collision held across all $\frac{L}{V}$ values except one—$\frac{L}{V} = 0.2$ s (Fig. 4.3E). Notably, lower $\frac{L}{V}$ value tended to reach larger maximum η values than higher $\frac{L}{V}$ values but there was a lot of overlap (Fig. 4.3E). These patterns of occurrence for higher maximum η may have implications for the recruitment of specialized escape circuits.

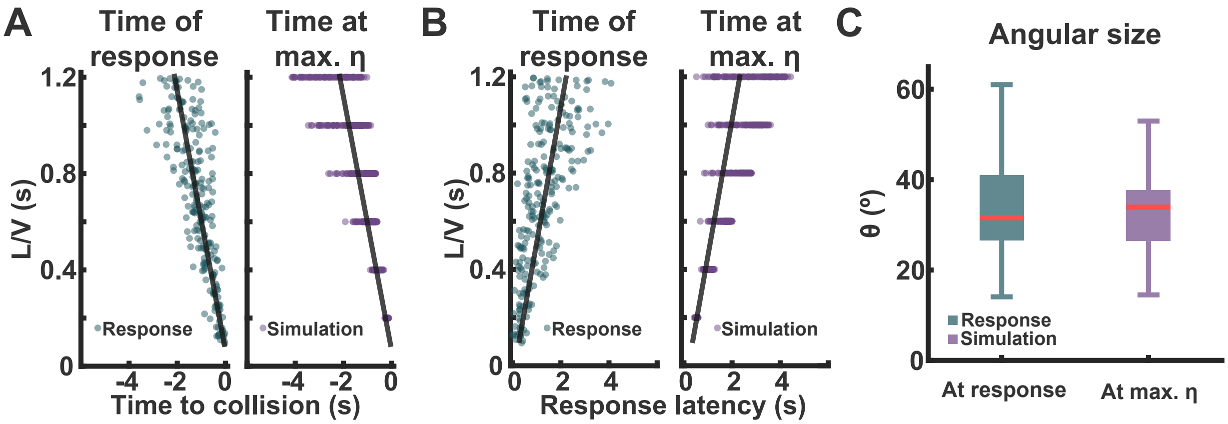

Figure 4.4. Comparison to real looming-evoked responses.

Figure 4.4 details: A) Timing of real looming-evoked responses of larval zebrafish compared to timing of maximum estimated $\eta(t)$ for a range of $\frac{L}{V}$ values. B) Response latencies of real looming-evoked responses of larval zebrafish compared to time of maximum estimated $\eta(t)$ after onset of looming. A–B) Lines of best fit for response and simulation are not significantly different for each pair (ANCOVA, Time to collision p-value = 0.92 , Response latency p-value = 0.91, Response n = 246, Simulation n = 6000). The residuals of each model describing the spread of points around the line are also not significantly different for real responses and simulations (F-test, Time to collision p-value = 0.75 , Response latency p-value = 0.82) . C) The distribution of angular size at the time of response and at the time of maximum η across all $\frac{L}{V}$ values are in good agreement (mean ± std, Response 35° ± 15°, Simulation 35° ± 11°).

Next, we compared the computed variability in the times of maximum η to the experimentally observed variability in the timing of the looming-evoked responses of larval zebrafish from behavioral data collected in a different study Bhattacharyya et al. (2017). We found that the time of looming-evoked responses and the time at maximum η with respect to collision were in good agreement (Fig. 4.4A). Specifically, the pattern of increasing variability with increasing $\frac{L}{V}$ values held for both simulation and behavioral data (Fig. 4.4A). Moreover, we found that this agreement extended to time of the looming-evoked responses and the time at maximum η from the onset of the stimulus, referred to as response latency (Fig. 4.4B). Finally, we compared the distributions of angular size of the object at the time of looming-evoked response and the angular size at the time of maximum η across all $\frac{L}{V}$ values to find that they were in good agreement as well (Fig. 4.4C).

Overall, these results demonstrate that the calculations of $\eta(t)$ from estimates of angular size and expansion rate have different distributions of times at maximum η for each $\frac{L}{V}$ value. Moreover, the variability in the times at maximum η increases with increasing $\frac{L}{V}$ values. For a given $\frac{L}{V}$ value, occurrences of maximum η further from collision tended to have higher η values than maxima occurring closer to collision. However, lower $\frac{L}{V}$ values tended to have higher maximum η values. Most importantly, the computational results regarding the distribution of times at maximum η and the distribution of angular sizes at maximum η align well with existing behavioral results for those values from looming-evoked responses in larval zebrafish.

4.3.4. Timing and probability of Mauthner cell recruitment

Larval zebrafish can escape from looming stimuli with or without the recruitment of the Mauthner cells—the giant fiber neurons responsible for the shortest latency and fastest escapes. Therefore, we next investigated how calculating $\eta(t)$ from estimates of angular size and expansion rate might influence the recruitment of the Mauthner cell (M-cell).

M-cells are found in a bilaterally symmetric pair in the hindbrain of larval zebrafish (Fig 4.5A) Korn and Faber (2005). Each M-cell projects an axon to the contralateral side of the body and with only one spike initiates an escape by recruiting downstream motoneurons and spinal interneurons Fetcho (1991). Since $\eta(t)$ is hypothesized to be the excitatory drive to premotor circuits, we scaled $\eta(t)$ by a constant and used it as the current injection, $I_e(t)$, to a leaky-integrate-and-fire model of the M-cell (Fig. 4.5B, Appendix) Koyama et al. (2016). Here we only model the recruitment of one M-cell since the pair of M-cells mutually inhibit one another and recruitment of either results in an escape Shimazaki et al. (2019). By numerically solving the neuron model, we computed $V_m(t)$ which represented the membrane voltage of the M-cell (Appendix).

To remain consistent with previous sections, we used multiple simulated presentations of $\frac{L}{V} = 0.8$ s as a representative looming rate to compute multiple estimates of $\eta(t)$. We multiplied each estimate of $\eta(t)$ by a constant β to compute $I_e(t)$ (Eq. 4.3) such that the M-cell model would spike during the looming stimulus for some $I_e(t)$ (Active cases, Fig. 4.5C) and not for others (Silent case, Fig. 4.5C, Appendix).

$$I_e(t) = \beta\eta(t) \tag{4.3}$$

Figure 4.5 details: A) The Mauthner cells (M-cells) exist as a bilaterally symmetric pair (shown in red) in the larval zebrafish hindbrain. Activation of one cell within the pair initiates an escape response to the contralateral side of the activated cell. B) A leaky integrate-and-fire model of the M-cell ($\mathrm{I_e}$: current input, $\mathrm{R_m}$: membrane resistance, $\mathrm{C_m}$: membrane capacitance, $\mathrm{V_m}$: membrane voltage) received linearly scaled $\eta(t)$ as excitatory current input, $\mathrm{I_e(t)}$, which drove the membrane voltage, $\mathrm{V_m(t)}$ (vertical scale bars, $\mathrm{I_e(t)}$: 0.2 nA, $\mathrm{V_m(t)}$: 10 mV). C) Multiple simulated excitatory current inputs from estimates of $\eta(t)$ for the same value of $\frac{L}{V} = 0.8$ s produced M-cell spikes at different times or no spike at all (vertical scale bar: 10 mV). D) The time of maximum current input, $\mathrm{I_e}$, for cases where the M-cell is recruited tend to occur earlier before

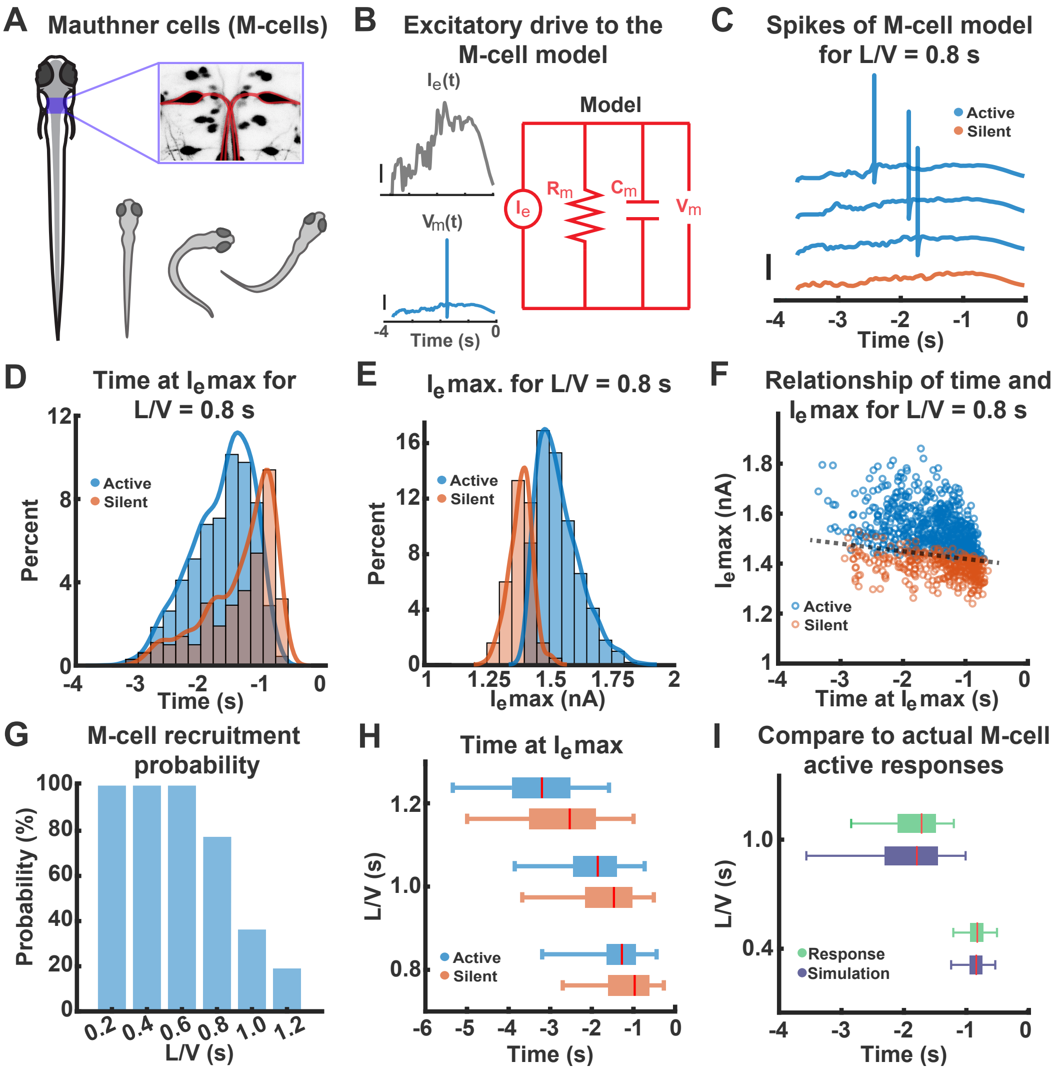

Figure 4.5. Timing and probability of Mauthner cell (M-cell) recruitment.

collision (Mann-Whitney U Test, p-value < 0.001, M-cell active $n = 745$, M-cell silent $n = 255$). E) The maximum current input, I_e, for cases where the M-cell is recruited is higher (Mann-Whitney U test, p-value < 0.001). F) The maximum current and time of maximum current for M-cell active and silent cases are separable by a boundary (dashed line) with a near-zero slope. G) The probability of recruiting the M-cell reduces with increasing $\frac{L}{V}$ values ($n = 1000$ for each $\frac{L}{V}$ value) . H) For $\frac{L}{V}$ values that produce both M-cell active and silent cases, the time of maximum current input for M-cell active cases tend to occur earlier from collision than those for silent cases for each $\frac{L}{V}$ (Mann Whitney U tests, all p-values < 0.001). I) Comparison of simulated M-cell spike times to $\frac{L}{V}$ values of 0.4 s and 1.0 s with actual M-cell responses to the same $\frac{L}{V}$ values shows a high degree of similarity (mean ± std, $\frac{L}{V} = 0.4$ s response: -0.8 ± 0.17 s, simulation: -0.81 ± 0.17 s, $\frac{L}{V} = 1.0$ s, response: -1.8 ± 0.44 s, simulation: -1.82 ± 0.5 s).

A range of β values stochastically produced spikes in the M-cell model for $I_e(t)$ calculated from $\frac{L}{V} = 0.8$ s (Fig. C.2, Appendix). Since this result computationally reproduced the probabilistic recruitment of M-cells to the same looming rate, we picked a single value of β (Fig. C.2, Appendix) and investigated further the differences in $I_e(t)$ for M-cell active and silent cases.

We compared the times at maximum I_e for M-cell silent and active cases to find that they were significantly different (Fig. 4.5D). M-cell active cases had maximum current values that occurred earlier from collision than M-cell silent cases (Fig. 4.5D). Moreover, the maximum values of the current input (I_e max.) for M-cell active and silent cases were also significantly different (Fig. 4.5E). As may be expected, M-cell active cases had higher maxima of current than M-cell silent cases (Fig. 4.5E).

When M-cell active and silent cases were plotted by their maximum value of I_e and the time of maximum I_e, the two groups were separable with high accuracy (>90%) by a linear boundary (dashed line Fig. 4.5F, Appendix). The near-zero slope of the boundary suggests that a threshold value of maximum I_e effectively separates the two groups. Since $I_e(t)$ is produced by multiplying $\eta(t)$ by a constant, the previous result regarding the occurrence of higher maximum values of η earlier from collision (Fig. 4.3C) also apply to maximum values of I_e. Thus, the likelihood of higher maximum I_e occurring earlier from collision and the association of higher maximum I_e with M-cell active cases is largely responsible for producing the difference in times between M-cell active and silent cases.

To test whether we could computationally reproduce the experimental result of the decreasing probability of M-cell recruitment with increasing $\frac{L}{V}$ Bhattacharyya et al. (2017), we repeated these simulations for a range of $\frac{L}{V}$ values using the same value of β. From 1000 simulations for each $\frac{L}{V}$ value, we found that the likelihood of producing an M-cell spike dropped with increasing $\frac{L}{V}$ (Fig. 4.5G). This decrease in the likelihood of M-cell active cases is due to the decreasing value of maximum η and, therefore, maximum I_e for higher $\frac{L}{V}$ values, as seen earlier (Fig. 4.3E). Since higher $\frac{L}{V}$ values produce lower maximum I_e, they are less likely to produce M-cell active cases.

Moreover, the time of maximum I_e for M-cell active cases was always earlier from collision than the time of maximum I_e for M-cell silent cases across all $\frac{L}{V}$ values that produced both cases (Fig. 4.5H). This aligns with experimental findings which show that M-cell active looming-evoked responses tend to occur earlier from collision than M-cell silent looming evoked responses for the same $\frac{L}{V}$ value Bhattacharyya et al. (2017). Critically, the constant multiplied to $\eta(t)$ to create $I_e(t)$ produced M-cell spikes to $\frac{L}{V} = 0.4$ s and $\frac{L}{V} = 1.0$ s that agreed very well with timing of M-cell active looming-evoked responses from larval zebrafish for the same $\frac{L}{V}$ values (Fig. 4.5I) Bhattacharyya et al. (2017).

These results show that when $\eta(t)$ is scaled by a constant and used as current input to a M-cell model, the model can stochastically produce M-cell spikes for the same $\frac{L}{V}$ value. M-cell active and silent cases were largely differentiated by the maximum value of I_e—the current input. M-cell active cases also tended to happen earlier than M-cell silent cases for the same $\frac{L}{V}$ value. Moreover, the probability of M-cell recruitment reduced with higher

$\frac{L}{V}$ values. The decreasing probability of M-cell spikes with increasing $\frac{L}{V}$ and the timing of simulated M-cell spikes both agreed well with experimentally observed data.

4.4. Discussion

Our goal was to account for previously unexplained behavioral results in looming-evoked responses by considering how noise in sensing the angular size of the looming object would influence the timing of escape behavior and the recruitment of specialized escape circuits. By taking the larval zebrafish as an example, we used the visual acuity as well as the flicker fusion frequency to approximate the percept of the looming stimulus as a sequence of noisy measurements of angular size. We used estimates of angular size and expansion rate inferred from the noisy measurements to compute $\eta(t)$ and showed how the variability in the time of maximum η corresponded to the variability in the timing of real looming-evoked responses in larval zebrafish. Furthermore, we scaled $\eta(t)$ by a constant and used it as the current injection to a computational model of the Mauthner neuron (M-cell) to demonstrate how the same looming stimulus could stochastically recruit the M-cell. Moreover, we computationally reproduced the timing of M-cell recruitment and the decreasing likelihood of M-cell recruitment in response to slower looming stimuli.

However, there are some discrepancies between our computational results and experimental data. For instance, our results suggest that the M-cell has a 100% likelihood of being recruited for fast looming stimuli—lower $\frac{L}{V}$ values. Conversely, experimental data from larval zebrafish shows that lower $\frac{L}{V}$ values do produce some escape responses that are not mediated by the M-cell Bhattacharyya et al. (2017). Moreover, researchers have found that some animals will freeze when responding to rapidly approaching predators Chelini et al. (2009); Herberholz and Marquart (2012); Misslin (2003); Bhattacharyya et al. (2017) which would suggest an inhibition of movement Shang et al. (2018). This discrepancy between experimental data and our computational results may be due to the calculation of other optical variables beyond $\eta(t)$, as seen in flies von Reyn et al. (2017); Ache et al. (2019) and pigeons Sun and Frost (1998). However, the calculation of these additional optical variables in other animals and their use in escape decisions is yet to be verified.

We propose that larval zebrafish use noisy measurements to produce more stable estimates of angular size and expansion rate for computing $\eta(t)$. We demonstrate how this can be done with a Kalman filter, a Bayes optimal recursive estimator. Bayesian estimation has provided a formalism for exploring and shaping important questions in neuroscience about sensory evaluation and motor behavior Doya et al. (2007); Kording (2007); Petzschner et al. (2015); Meyniel et al. (2015). While direct evidence of recursive Bayesian filtering has not been found in the nervous systems of animals, researchers have found experimental evidence that aligns with hypotheses of Bayesian predictive coding Aitchison and Lengyel (2017). Specifically, population coding in the brains of animals is hypothesized to represent the probability distributions necessary for recursive estimation Knill and Pouget (2004); Zemel et al. (1998). Relevant to this point, there is evidence that the optic tectum of larval zebrafish uses population coding to represent the looming rate of a looming stimulus Dunn et al. (2016). Moreover, the information processing in the tectum of larval zebrafish is necessary for producing looming-evoked responses Temizer et al. (2015). The Kalman filter computed estimates in our study serve as an analog of what may be achieved by the nervous system.

Our work shows how the visual acuity of larval zebrafish has consequences on the timing and recruitment of escape circuits for looming-evoked responses. The computational findings presented here can be tested and extended further by performing experiments with looming stimuli on adult zebrafish since they have approximately 3-fold better visual acuity (±1°) than their larval counterparts Tappeiner et al. (2012). This increase in visual acuity should produce far better estimates of the angular size and the expansion rate which would further improve the estimate of $\eta(t)$. When the estimates of $\eta(t)$ are in better agreement with the true $\eta(t)$, there would be lower variability in the timing of maximum η and, hence, the timing of looming-evoked responses to the same $\frac{L}{V}$ value. Furthermore, this change in the timing of maximum η would also influence the probability and variability of M-cell recruitment across $\frac{L}{V}$ values. An existing study on adult goldfish does suggest that there is differential excitatory drive to the M-cell based on looming stimulus parameters Preuss et al. (2006), but systematic differences in the variability of timing and probability of M-cell recruitment in adult fish responding to looming stimuli are not known.

Beyond experiments with adult fish, changing the parameters of the looming stimulus may also help further test the paradigm presented here. For instance, recent results have shown that looming stimuli with linear rates of angular expansion produce escape responses in flies with some latency from the onset of expansion von Reyn et al. (2017). We would expect the time of maximum η to coincide with or occur near the time of the escape response. However, for linearly expanding stimuli, $\eta(t)$ reaches its maximum value at the onset of expansion since, in this case, the expansion rate $\dot{\theta}(t)$ is a constant and the term $e^{-\alpha\theta(t)}$ decreases monotonically with time (Eq. 4.2). This inconsistency can potentially be resolved by the paradigm presented here since we propose that $\eta(t)$ is computed from smooth Kalman-filtered estimates of the expansion rate. Therefore, from the onset of linear expansion, the estimate of the expansion rate would change smoothly until it reached the true constant value making the maximum of $\eta(t)$ occur some time after stimulus onset. While one study has shown that larval zebrafish respond to linearly expanding looming stimuli Dunn et al.

(2016), differences in the timing of responses to different rates of linear expansion have not been studied systematically.

The results presented here propose a mechanism to explain the variability in the timing of responses to the same looming rate as described by $\frac{L}{V}$. Not just larval zebrafish, but also flies, locusts, and crabs are known to escape at different times in response to repeated presentations of the same $\frac{L}{V}$ looming rate von Reyn et al. (2014); Fotowat and Gabbiani (2007); Oliva and Tomsic (2012). This suggests that our results regarding the variability in the timing of $\eta(t)$ extends to these animals as well. The evidence for variability in time of maximum η is also found in studies investigating the pigeon brain where the firing frequency of neurons that are hypothesized to encode $\eta(t)$ reach their peak firing rate at different times in response to the same looming stimuli Sun and Frost (1998); Wu et al. (2005).

Furthermore, we propose a mechanism for the differential recruitment of the M-cell, the giant neuron in fish, in response to different looming stimuli. Escapes that are generated without the recruitment of giant neurons have been found to be more variable in their timing and kinematics Edwards et al. (1999); Domenici et al. (2011a); Eaton and Emberley (1991); Gahtan and Baier (2004); von Reyn et al. (2014); Bhattacharyya et al. (2017). This ability to generate variable escape maneuvers is thought to confer a selective advantage since it diminishes a predator's ability to predict the response of the prey Driver and Humphries (1970). However, there may be trade-offs between performance and variability in escapes due to the biomechanical constraints on high velocities and accelerations Hitchcock et al. (2015). Therefore, the changing probability of giant neuron recruitment with predator approach rate can be interpreted as a changing escape strategy to different predator speeds Meager et al. (2006). Here, by replicating the graded recruitment of a giant neuron, we present a possible mechanism for deploying different escape strategies stochastically.

More broadly, the Mauthner cell and other giant neurons have been studied as neurobiological models of decision-making and action selection Edwards et al. (1999); Korn and Faber (2005); Herberholz and Marquart (2012); von Reyn et al. (2014); Roberts et al. (2019). Consequently, our computational framework demonstrates how noise and uncertainty in the sensory input might influence decision-making and the selection of motor programs. Through this approach, we argue that the sensory noise, the methods of compensating for it, and the neural computations combine to produce functional behavior composed of variable and graded responses to stimuli. Not only do these findings apply to looming-evoked responses but likely extend to other behaviors since noise is inescapable and, beyond being a nuisance, may be useful to the nervous system Traynelis and Jaramillo (1998); Faisal et al. (2008). Since the neural substrate subserving the mechanisms of decision-making evolved under the constraints imposed by noise, noise may have been incorporated as an essential element into the sensorimotor architecture of the animal.

CHAPTER 5

Deciding under duress

The main objective of this thesis was to investigate the escape decisions of larval zebrafish in order to understand how they are implemented by the sensorimotor system and shaped by the selection pressures of predation. These escape decisions included whether, when, and how to perform an escape maneuver given a predatory attack. To this end, over the course of this thesis, I studied the timing, kinematics, and neurobiology of the escape movements in response to both real and simulated predators through experimental and computational approaches.

5.1. Summary of primary results

- Larval zebrafish perform a graded assessment of the threat posed by a looming predator based on the looming rate and stochastically deploy different escape strategies.
- These escape strategies include 1) freezing, 2) performing an escape with Mauthner cell recruitment (Mauthner-active), or 3) performing an escape without Mauther cell recruitment (Mauthner-silent).
- Mauthner-active and Mauthner-silent escapes have distinct kinematics and patterns of neural recruitment for spinal projecting neurons in the hindbrain of larval zebrafish. These patterns correspond to the role of specific nuclei in producing motor aspects of the escape maneuver.

- When escaping from the predator's strike, the time remaining at escape is a critical determinant of survival since it limits the motor volume of the prey.
- The non-overlapping regions of predator and prey motor volumes within the time remaining at escape determines the utility of escape movements and the recruitment of corresponding neural circuits, including the Mauthner cell.
- Incorporating the uncertainty due to the limit of visual acuity into the hypothesized neural computations for looming-evoked responses explains the increasing variability in the timing of escape responses with slower looming rates and the patterns of Mauthner cell recruitment.

Overall, I examine how the balance between Mauthner-active and Mauthner-silent escapes is modulated by the percept of the attack, is executed through the spinal projecting neurons in the hindbrain, and produces graded responses with distinct kinematics. Furthermore, I develop an approach that models predator-prey interactions to explore the implications for survival due to the differential recruitment of the Mauthner cell. Finally, I propose a mechanism that explains how graded and variable responses may be initiated in response to a predator by considering the influence of sensory noise on the neural computations subserving the escape response.

5.2. Recommendations for future work

In Chapter 2, I found that Mauthern-active and Mauthner-silent responses have characteristic signatures of neural recruitment in the hindbrain and, in Chapter 4, I propose a mechanism for how the Mauthner cell may be recruited differentially based on the looming stimulus. However, the mechanism of graded recruitment for the other reticulospinal neurons is still unclear. Existing work suggests that additional reticulospinal neurons may be recruited by the Mauthner cell once it is recruited Neki et al. (2014). While this may be the case, I also find that fish escape directionally away from the looming stimulus indicating that motor circuits which perform graded initial bends are recruited in parallel. Therefore, based on the azimuthal location of the approaching predator, there may be biased visual input from the optic tectum into the reticulospinal nuclei contributing to turning. Since specific reticulospinal nuclei of the larval zebrafish have been identified to contribute to turning movements Orger et al. (2008); Huang et al. (2013), the excitatory drive to these nuclei could be tested in response to looming stimuli approaching from different azimuthal angles. This would also investigate whether the spinal projecting neurons in the hindbrain contributing to turning have patterns of recruitment relating to the retinotopic map found in the optic tectum of larval zebrafish Niell and Smith (2005).

Beyond turning, I also find changes in the frequency of propulsive swimming movements in response to different predator approach speeds. This suggests that there is modulation of the excitatory drive to the reticulospinal nuclei contributing to forward swimming. The drive to these nuclei Huang et al. (2013); Severi et al. (2014); Wang and McLean (2014) could be tested in response to different predator approach speeds to see how recruitment changes. Furthermore, due to the shifts in the subset of spinal interneurons McLean et al. (2008), motoneurons Kishore et al. (2014), and musculature Buss and Drapeau (2002) of larval zebrafish related to different frequencies of swimming, the consequences of this graded excitatory drive may be tested downstream of the reticulospinal neurons. These experiments will also help clarify how the time-limited motor volume of larval zebrafish, presented in Chapter 3, is shaped by and corresponds to the sensorimotor architecture of the animal.

Additionally, in Chapter 3, I argue that larval zebrafish differentially recruit the Mauthner cell in response to fluid perturbations due to the dragonfly nymph strike. Furthermore, using a computational approach, I estimate the utility of Mauthner cell recruitment for increasing the survival probability. However, it is not known whether the actual recruitment of the Mauthner cell corresponds to the estimated utility. This can be tested by performing calcium imaging of the Mauthner cell of partially-restrained larval zebrafish while presenting flow stimuli of different magnitudes to track the probability of Mauthner cell recruitment. Beyond testing the recruitment of the Mauthner cell, its influence on survival can be measured through Mauthner cell ablation experiments Liu and Fetcho (1999); Burgess and Granato (2007). The escape success rate of larval zebrafish with ablated Mauthner cells in response to dragonfly nymph attacks should be lower. However, the results in this thesis would suggest that this difference would be highest for a specific range of attacks that left more than 7 ms but less than 35 ms of time remaining at escape.

Furthermore, the relevance of the time remaining at escape in driving the decision to recruit the Mauthner cell can also be tested. While animals are known to estimate the time remaining to capture for visual stimuli Rind and Simmons (1999); Santer et al. (2006); Liu et al. (2011b), proof of this estimation has not been shown from flow stimuli. Similar experiments to Preuss et al. (2006) could be carried out, except using ramping flow stimuli. The excitatory drive to the Mauthner cell in response to increasing profiles of flow velocities—like those found for dragonfly nymph attacks—could provide insight into whether an estimation of the time remaining at escape is driving the recruitment of the Mauthner cell.

The findings in the Chapter 4 suggest that noise, the methods of compensating for it, and neural computations influence the recruitment of the Mauthner cell and together generate the patterns of recruitment observed in response to looming stimuli. This computational work can be subject to further experimental verification in adult zebrafish which have 3-fold better visual acuity than their larval counterparts. The timing and kinematics of looming-evoked responses of adult zebrafish to varying looming rates should be less variable and the patterns of Mauthner cell recruitment should be distinct from larval fish. In addition to experiments with adult zebrafish, further experiments testing the responses of larval zebrafish to linearly expanding stimuli can also clarify if the assumptions in the computational work hold across different experimental scenarios. Finally, accounting for the noise due to visual acuity on the looming-evoked responses of other animals with giant neurons, especially flies, could verify whether the findings apply across animals. This would also require performing additional experiments with other animals to determine the specific patterns of giant neuron recruitment with changing looming rates.

5.3. Concluding remarks

Evidence from this thesis and previous work suggests that motor decisions of larval zebrafish are executed by reticulospinal and spinal microcircuits organized into modules for efficient control and coordination of movement. Researchers have found similar spinal microcircuits in limbed vertebrates for modular control of the joints, limbs, and trunk of the animal Hägglund et al. (2013). Furthermore, comparative experiments of development across vertebrate animals have found that the axial expression boundaries of *Hox* genes specifies the identity and morphology of individual vertebrae Kessel and Gruss (1990); Burke et al. (1995). This specification of segmental identity extends beyond the spinal cord and into the hindbrain Tümpel et al. (2009) where the structural patterning of neurons crosses segment boundaries Kinkhabwala et al. (2011). In combination, these results about the homology of regional differentiation and functional organization in the vertebrate nervous system suggest that the findings in this thesis about the selection and execution of motor decisions by larval zebrafish and the ecological pressures shaping those decisions extend to other vertebrate animals.

References

Ache, J. M., Polsky, J., Alghailani, S., Parekh, R., Breads, P., Peek, M. Y., Bock, D. D., von Reyn, C. R., and Card, G. M. (2019). Neural basis for looming size and velocity encoding in the drosophila giant fiber escape pathway. *Current Biology*.

Ahrens, M. B., Li, J. M., Orger, M. B., Robson, D. N., Schier, A. F., Engert, F., and Portugues, R. (2012). Brain-wide neuronal dynamics during motor adaptation in zebrafish. *Nature*, 485(7399):471.

Aitchison, L. and Lengyel, M. (2017). With or without you: predictive coding and bayesian inference in the brain. *Current opinion in neurobiology*, 46:219–227.

Bandyopadhyay, P. R., Castano, J. M., Rice, J. Q., Philips, R. B., Nedderman, W. H., and Macy, W. (1997). Low-speed maneuvering hydrodynamics of fish and small underwater vehicles. *Journal of Fluids Engineering*, 119(1):136–44.

Bar-Shalom, Y., Li, X. R., and Kirubarajan, T. (2004). *Estimation with applications to tracking and navigation: theory algorithms and software*. John Wiley & Sons.

Bay, J. S. (1991). A fully autonomous active sensor-based exploration concept for shape-sensing robots. *IEEE Transactions on Systems Man and Cybernetics*, 21(4):850–860.

Beat, M., Trtik, P., Marone, F., and Stampanoni, M. (2009). Stripe and ring artifact removal with combined wavelet-fourier filtering. *Optics Express*, (10):8567–8591.

Bhatt, D. H., McLean, D. L., Hale, M. E., and Fetcho, J. R. (2007). Grading movement strength by changes in firing intensity versus recruitment of spinal interneurons. *Neuron*, 53(1):91–102.

Bhattacharyya, K., McLean, D. L., and MacIver, M. A. (2017). Visual Threat Assessment and Reticulospinal Encoding of Calibrated Responses in Larval Zebrafish. *Curr. Biol.*, 27(18):2751–2762.

Bierman, H. S., Zottoli, S. J., and Hale, M. E. (2009). Evolution of the Mauthner Axon Cap. *BRAIN BEHAVIOR AND EVOLUTION*, 73(3):174–187.

Blanchard, D. C. and Blanchard, R. J. (1988). Ethoexperimental approaches to the biology of emotion. *Annu Rev Psychol*, 39:43–68.

Blanke, A., Busse, S., and Machida, R. (2015). Coding characters from different life stages for phylogenetic reconstruction: a case study on dragonfly adults and larvae, including a description of the larval head anatomy of epiophlebia superstes (odonata: Epiophlebiidae). *Zoological Journal of the Linnean Society*, 174(4):718–732.

Broxton, M., Grosenick, L., Yang, S., Cohen, N., Andelman, A., Deisseroth, K., and Levoy, M. (2013). Wave optics theory and 3-d deconvolution for the light field microscope. *Optics Express*, 21(21):25418–25439.

Budick, S. A. and O'Malley, D. M. (2000). Locomotor repertoire of the larval zebrafish: swimming, turning and prey capture. *J Exp Biol*, 203(Pt 17):2565–79.

Burgess, H. A. and Granato, M. (2007). Sensorimotor gating in larval zebrafish. *Journal of Neuroscience*, 27(18):4984–4994.

Burke, A. C., Nelson, C. E., Morgan, B. A., and Tabin, C. (1995). Hox genes and the evolution of vertebrate axial morphology. *Development*, 121(2):333–346.

Burkitt, A. N. (2006). A review of the integrate-and-fire neuron model: I. homogeneous synaptic input. *Biological cybernetics*, 95(1):1–19.

Buss, R. R. and Drapeau, P. (2002). Activation of embryonic red and white muscle fibers during fictive swimming in the developing zebrafish. *Journal of Neurophysiology*, 87(3):1244–1251.

Busse, S. and Gorb, S. N. (2018). Material composition of the mouthpart cuticle in a damselfly larva (insecta: Odonata) and its biomechanical significance. *Royal Society Open Science*, 5(6).

Card, G. M. (2012). Escape behaviors in insects. *Curr Opin Neurobiol*, 22(2):180–6.

Carew, T. J. (2000). *Behavioral neurobiology: the cellular organization of natural behavior*. Sinauer Associates, Sunderland, Massachusetts.

Casagrand, J. L., Guzik, A. L., and Eaton, R. C. (1999). Mauthner and reticulospinal responses to the onset of acoustic pressure and acceleration stimuli. *Journal of Neurophysiology*, 82(3):1422–1437.

Catania, K. C. (2009). Tentacled snakes turn c-starts to their advantage and predict future prey behavior. *Proc Natl Acad Sci U S A*, 106(27):11183–7.

Catania, K. C. (2010). Born knowing: tentacled snakes innately predict future prey behavior. *PLoS One*, 5(6):e10953.

Chang, Y. T., Lin, J. W., and Faber, D. S. (1987). Spinal inputs to the ventral dendrite of the teleost Mauthner cell. *Brain Research*, 417(2):205–213.

Chelini, M. C., Willemart, R. H., and Hebets, E. A. (2009). Costs and benefits of freezing behaviour in the harvestman eumesosoma roeweri (arachnida, opiliones). *Behav Processes*, 82(2):153–9.

Corcoran, A. J. and Conner, W. E. (2016). How moths escape bats: predicting outcomes of predator–prey interactions. *Journal of Experimental Biology*, 219(17):2704–2715.

Curti, S. and Pereda, A. E. (2004). Voltage-dependent enhancement of electrical coupling by a subthreshold sodium current. *Journal of Neuroscience*, 24(16):3999–4010.

Dangles, O., Ory, N., Steinmann, T., Christides, J. P., and Casas, J. (2006). Spider's attack versus cricket's escape: velocity modes determine success. *Animal Behaviour*, 72:603–610.

Danos, N. and Lauder, G. V. (2012). Challenging zebrafish escape responses by increasing water viscosity. *J Exp Biol*, 215(Pt 11):1854–62.

de Vries, S. E. J. and Clandinin, T. R. (2012). Loom sensitive neurons link computation to action in the drosophila visual system. *Curr Biol*, 22(5):353–362.

deVries, M. S., Murphy, E. A. K., and Patek, S. N. (2012). Strike mechanics of an ambush predator: the spearing mantis shrimp. *Journal of Experimental Biology*, 215(24):4374–4384.

Domenici, P. (2002). The visually mediated escape response in fish: Predicting prey responsiveness and the locomotor behaviour of predators and prey. *Marine and Freshwater Behaviour and Physiology*, 35(1-2):87–110.

Domenici, P., Blagburn, J. M., and Bacon, J. P. (2011a). Animal escapology I: theoretical issues and emerging trends in escape trajectories. *J Exp Biol*, 214(Pt 15):2463–73.

Domenici, P., Blagburn, J. M., and Bacon, J. P. (2011b). Animal escapology II: escape trajectory case studies. *J Exp Biol*, 214(Pt 15):2474–94.

Doya, K., Ishii, S., Pouget, A., and Rao, R. P. (2007). *Bayesian brain: Probabilistic approaches to neural coding*. MIT press.

Driver, P. M. and Humphries, D. A. (1970). Protean displays as inducers of conflict. *Nature*, 226(5249):968–9.

Dunn, T. W., Gebhardt, C., Naumann, E. A., Riegler, C., Ahrens, M. B., Engert, F., and Del Bene, F. (2016). Neural Circuits Underlying Visually Evoked Escapes in Larval Zebrafish. *Neuron*, 89(3):613–628.

Eaton, R. C., DiDomenico, R., and Nissanov, J. (1988). Flexible body dynamics of the goldfish c-start: implications for reticulospinal command mechanisms. *J Neurosci*, 8(8):2758–68.

Eaton, R. C., DiDomenico, R., and Nissanov, J. (1991). Role of the Mauthner cell in sensorimotor integration by the brain stem escape network. *Brain Behav Evol*, 37(5):272–85.

Eaton, R. C. and Emberley, D. S. (1991). How stimulus direction determines the trajectory of the Mauthner-initiated escape response in a teleost fish. *J Exp Biol*, 161:469–87.

Eaton, R. C., Lavender, W. A., and Wieland, C. M. (1981). Identification of Mauthner-initiated response patterns in goldfish - evidence from simultaneous cinematography and electrophysiology. *Journal of Comparative Physiology*, 144(4):521–531.

Eaton, R. C., Lee, R. K., and Foreman, M. B. (2001). The Mauthner cell and other identified neurons of the brainstem escape network of fish. *Prog Neurobiol*, 63(4):467–85.

Eaton, R. C., Nissanov, J., and Wieland, C. M. (1984). Differential activation of mauthner and non-mauthner startle circuits in the zebrafish: implications for functional substitution. *Journal of Comparative Physiology A*, 155(6):813–820.

Edelstein, A. D., Tsuchida, M. A., Amodaj, N., Pinkard, H., Vale, R. D., and Stuurman, N. (2014). Advanced methods of micrsocope control using micromanager software. *Journal of Biological Methods*, 1:doi:10.14440/jbm.2014.36.

Edut, S. and Eilam, D. (2004). Protean behavior under barn-owl attack: voles alternate between freezing and fleeing and spiny mice flee in alternating patterns. *Behavioural Brain Research*, 155(2):207–216.

Edwards, D. H., Heitler, W. J., and Krasne, F. B. (1999). Fifty years of a command neuron: the neurobiology of escape behavior in the crayfish. *Trends Neurosci*, 22(4):153–61.

Egan, R. J., Bergner, C. L., Hart, P. C., Cachat, J. M., Canavello, P. R., Elegante, M. F., Elkhayat, S. I., Bartels, B. K., Tien, A. K., Tien, D. H., Mohnot, S., Beeson, E., Glasgow, E., Amri, H., Zukowska, Z., and Kalueff, A. V. (2009). Understanding behavioral and physiological phenotypes of stress and anxiety in zebrafish. *Behav Brain Res*, 205(1):38–44.

Faber, D. S., Fetcho, J. R., and Korn, H. (1989). Neuronal networks underlying the escape response in goldfish. general implications for motor control. *Ann N Y Acad Sci*, 563:11–33.

Faisal, A. A., Selen, L. P., and Wolpert, D. M. (2008). Noise in the nervous system. *Nat Rev Neurosci*, 9(4):292–303.

Feder, H. J. S., Leonard, J. J., and Smith, C. M. (1999). Adaptive mobile robot navigation and mapping. *International Journal of Robotics Research*, 18(7):650–668.

Fetcho, J. R. (1991). Spinal network of the Mauthner cell. *Brain Behav Evol*, 37(5):298–316.

Fitzpatrick, R. (2017). *Theoretical Fluid Mechanics*. IOP Publishing.

Fotowat, H. and Gabbiani, F. (2007). Relationship between the phases of sensory and motor activity during a looming-evoked multistage escape behavior. *J Neurosci*, 27(37):10047–59.

Fotowat, H. and Gabbiani, F. (2011). Collision detection as a model for sensory-motor integration. *Annu Rev Neurosci*, 34:1–19.

Fuiman, L. A., Rose, K. A., Cowan, J. H., and Smith, E. P. (2006). Survival skills required for predator evasion by fish larvae and their relation to laboratory measures of performance. *Animal Behaviour*, 71:1389–1399.

Fukami, Y., Furukawa, T., and Asada, Y. (1965). Excitability changes of the Mauthner cell during collateral inhibition. *J Gen Physiol*, 48:581–600.

Furshpan, E. J. and Furukawa, T. (1962). Intracellular and extracellular responses of the several regions of the Mauthner cell of the goldfish. *J Neurophysiol*, 25:732–71.

Gabbiani, F., Krapp, H. G., and Laurent, G. (1999). Computation of object approach by a wide-field, motion-sensitive neuron. *J Neurosci*, 19(3):1122–41.

Gahtan, E. and Baier, H. (2004). Of lasers, mutants, and see-through brains: functional neuroanatomy in zebrafish. *J Neurobiol*, 59(1):147–61.

Gahtan, E. and O'Malley, D. M. (2003). Visually guided injection of identified reticulospinal neurons in zebrafish: a survey of spinal arborization patterns. *Journal of Comparative Neurology*, 459(2):186–200.

Gahtan, E., Sankrithi, N., Campos, J. B., and O'Malley, D. M. (2002). Evidence for a widespread brain stem escape network in larval zebrafish. *J Neurophysiol*, 87(1):608–14.

Hägglund, M., Dougherty, K. J., Borgius, L., Itohara, S., Iwasato, T., and Kiehn, O. (2013). Optogenetic dissection reveals multiple rhythmogenic modules underlying locomotion. *Proceedings of the National Academy of Sciences*, 110(28):11589–11594.

Harris, J. A., Cheng, A. G., Cunningham, L. L., MacDonald, G., Raible, D. W., and Rubel, E. W. (2003). Neomycin-induced hair cell death and rapid regeneration in the lateral line of zebrafish (danio rerio). *J Assoc Res Otolaryngol*, 4(2):219–34.

Hatsopoulos, N., Gabbiani, F., and Laurent, G. (1995). Elementary computation of object approach by wide-field visual neuron. *Science*, 270(5238):1000–3.

Hatta, K. and Korn, H. (1998). Physiological properties of the Mauthner system in the adult zebrafish. *J Comp Neurol*, 395(4):493–509.

Haug, M. F., Biehlmaier, O., Mueller, K. P., and Neuhauss, S. C. (2010). Visual acuity in larval zebrafish: behavior and histology. *Front Zool*, 7:8.

Herberholz, J. and Marquart, G. D. (2012). Decision making and behavioral choice during predator avoidance. *Front Neurosci*, 6:125.

Higham, T. E., Day, S. W., and Wainwright, P. C. (2006). Multidimensional analysis of suction feeding performance in fishes: fluid speed, acceleration, strike accuracy and the ingested volume of water. *J Exp Biol*, 209(Pt 14):2713–25.

Hitchcock, A. C., Chen, T., Connolly, E., Darakananda, K., Jeong, J., Quist, A., Robbins, A., and Ellerby, D. J. (2015). Trade-offs between performance and variability in the escape responses of bluegill sunfish (lepomis macrochirus). *Biol Open*, 4(6):743–51.

Howland, H. C. (1974). Optimal strategies for predator avoidance - relative importance of speed and maneuverability. *Journal of Theoretical Biology*, 47(2):333–350.

Huang, K.-H., Ahrens, M. B., Dunn, T. W., and Engert, F. (2013). Spinal projection neurons control turning behaviors in zebrafish. *Current Biology*, 23(316):1566–1573.

Jones, K. A., Jackson, A. L., and Ruxton, G. D. (2011). Prey jitters; protean behaviour in grouped prey. *Behavioral Ecology*, 22(4):831–836.

Katzir, G. (1993). Escape response of black mollies (poecilia-shenops) to predatory dives of a pied kingfisher (ceryle-rudis). *Copeia*, (2):549–553.

Kelsh, R. N., Brand, M., Jiang, Y. J., Heisenberg, C. P., Lin, S., Haffter, P., Odenthal, J., Mullins, M. C., van Eeden, F. J., Furutani-Seiki, M., Granato, M., Hammerschmidt, M., Kane, D. A., Warga, R. M., Beuchle, D., Vogelsang, L., and Nusslein-Volhard, C. (1996). Zebrafish pigmentation mutations and the processes of neural crest development. *Development*, 123:369–89.

Kessel, M. and Gruss, P. (1990). Murine developmental control genes. *Science*, 249(4967):374–379.

Kimura, Y., Satou, C., Fujioka, S., Shoji, W., Umeda, K., Ishizuka, T., Yawo, H., and Higashijima, S. (2013). Hindbrain v2a neurons in the excitation of spinal locomotor circuits during zebrafish swimming. *Current Biology*, 23(10):843–849.

Kinkhabwala, A., Riley, M., Koyama, M., Monen, J., Satou, C., Kimura, Y., Higashijima, S., and Fetcho, J. (2011). A structural and functional ground plan for neurons in the hindbrain of zebrafish. *Proceedings of the National Academy of Sciences*, 108(3):1164–1169.

Kishore, S., Bagnall, M. W., and McLean, D. L. (2014). Systematic shifts in the balance of excitation and inhibition coordinate the activity of axial motor pools at different speeds of locomotion. *Journal of Neuroscience*, 34.

Kleiner, M., Brainerd, D. H., Pelli, D. G., Ingling, A., Murray, R., and Broussard, C. (2007). What's new in psychtoolbox-3. *Perception*, 36:1.

Knill, D. C. and Pouget, A. (2004). The Bayesian brain: the role of uncertainty in neural coding and computation. *Trends in Neurosciences*, 27(12):712–719.

Kohashi, T. and Oda, Y. (2008). Initiation of Mauthner- or non-Mauthner-mediated fast escape evoked by different modes of sensory input. *J Neurosci*, 28(42):10641–53.

Kording, K. (2007). Decision theory: What "should" the nervous system do? *Science*, 318(5850):606–610.

Korn, H. and Faber, D. S. (2005). The Mauthner cell half a century later: a neurobiological model for decision-making? *Neuron*, 47(1):13–28.

Kovvali, N., Banavar, M., and Spanias, A. (2013). An introduction to kalman filtering with matlab examples. *Synthesis Lectures on Signal Processing*, 6(2):1–81.

Koyama, M., Minale, F., Shum, J., Nishimura, N., Schaffer, C. B., and Fetcho, J. R. (2016). A circuit motif in the zebrafish hindbrain for a two alternative behavioral choice to turn left or right. *Elife*, 5.

Lebastard, V., Boyer, F., Chevallereau, C., and Servagent, N. (2012). Underwater electro-navigation in the dark. In *2012 IEEE International Conference on Robotics and Automation (ICRA)*, pages 1155–1160. IEEE.

Libersat, F. (1994). The dorsal giant interneurons mediate evasive behavior in flying cockroaches. *J Exp Biol*, 197:405–11.

Lieschke, G. J. and Currie, P. D. (2007). Animal models of human disease: zebrafish swim into view. *Nature Reviews Genetics*, 8(5):353.

Liu, D.-Y., Gibaru, O., and Perruquetti, W. (2011a). Error analysis of jacobi derivative estimators for noisy signals. *Numerical Algorithms*, 58(1):53–83.

Liu, K. S. and Fetcho, J. R. (1999). Laser ablations reveal functional relationships of segmental hindbrain neurons in zebrafish. *Neuron*, 23(2):325–35.

Liu, Y. J., Wang, Q., and Li, B. (2011b). Neuronal responses to looming objects in the superior colliculus of the cat. *Brain Behav Evol*, 77(3):193–205.

MacIver, M. A., Fontaine, E., and Burdick, J. W. (2004). Designing future underwater vehicles: principles and mechanisms of the weakly electric fish. *IEEE J. Ocean. Eng.*, 29(3):651–659.

MacIver, M. A., Schmitz, L., Mugan, U., Murphey, T. D., and Mobley, C. D. (2017). Massive increase in visual range preceded the origin of terrestrial vertebrates. *Proceedings of the National Academy of Sciences*, 114(12):E2375–E2384.

McHenry, M. J., Feitl, K. E., Strother, J. A., and Van Trump, W. J. (2009). Larval zebrafish rapidly sense the water flow of a predator's strike. *Biol Lett*, 5(4):477–9.

McLean, D. L. and Fetcho, J. R. (2009). Spinal interneurons differentiate sequentially from those driving the fastest swimming movements in larval zebrafish to those driving the slowest ones. *Journal of Neuroscience*, 29(43):13566–13577.

McLean, D. L., Masino, M. A., Koh, I. Y., Lindquist, W. B., and Fetcho, J. R. (2008). Continuous shifts in the active set of spinal interneurons during changes in locomotor speed. *Nature neuroscience*, 11(12):1419–1429.

Meager, J. J., Domenici, P., Shingles, A., and Utne-Palm, A. C. (2006). Escape responses in juvenile atlantic cod gadus morhua l.: the effects of turbidity and predator speed. *Journal of Experimental Biology*, 209(20):4174–4184.

Medan, V. and Preuss, T. (2014). The Mauthner-cell circuit of fish as a model system for startle plasticity. *J Physiol Paris*, 108(2-3):129–40.

Metcalfe, W. K., Mendelson, B., and Kimmel, C. B. (1986). Segmental homologies among reticulospinal neurons in the hindbrain of the zebrafish larva. *Journal of Comparative Neurology*, 251(2):147–159.

Meyniel, F., Sigman, M., and Mainen, Z. F. (2015). Confidence as bayesian probability: From neural origins to behavior. *Neuron*, 88(1):78–92.

Mirjany, M., Preuss, T., and Faber, D. S. (2011). Role of the lateral line mechanosensory system in directionality of goldfish auditory evoked escape response. *J Exp Biol*, 214(Pt 20):3358–67.

Misslin, R. (2003). The defense system of fear: behavior and neurocircuitry. *Neurophysiol Clin*, 33(2):55–66.

Moore, T. Y. and Biewener, A. A. (2015). Outrun or outmaneuver: Predator-prey interactions as a model system for integrating biomechanical studies in a broader ecological and evolutionary context. *Integr Comp Biol*, 55(6):1188–97.

Nair, A., Azatian, G., and McHenry, M. J. (2015). The kinematics of directional control in the fast start of zebrafish larvae. *J Exp Biol*, 218(Pt 24):3996–4004.

Nair, A., Nguyen, C., and McHenry, M. J. (2017). A faster escape does not enhance survival in zebrafish larvae. *Proc Biol Sci*, 284(1852).

Nakayama, H. and Oda, Y. (2004). Common sensory inputs and differential excitability of segmentally homologous reticulospinal neurons in the hindbrain. *J Neurosci*, 24(13):3199–209.

Neki, D., Nakayama, H., Fujii, T., Matsui-Furusho, H., and Oda, Y. (2014). Functional motifs composed of morphologically homologous neurons repeated in the hindbrain segments. *Journal of Neuroscience*, 34(9):3291–3302.

Niell, C. M. and Smith, S. J. (2005). Functional imaging reveals rapid development of visual response properties in the zebrafish tectum. *Neuron*, 45(6):941–951.

Nissanov, J., Eaton, R. C., and DiDomenico, R. (1990). The motor output of the Mauthner cell, a reticulospinal command neuron. *Brain Res*, 517(1-2):88–98.

Olesen, J. (1972). Hydraulic mechanism of labial extension and jet propulsion in dragonfly nymphs. *Journal of Comparative Physiology*, 81(1):53.

Olesen, J. (1978). Prey capture in dragonfly nymphs (odonata, insecta): Labial protraction by means of a multi-purpose abdominal pump. *Videnskabelige Meddelelser fra dansk naturhistorisk Forening*, Vidensk. Meddr dansk naturh. Foren.

Oliva, D., Medan, V., and Tomsic, D. (2007). Escape behavior and neuronal responses to looming stimuli in the crab chasmagnathus granulatus (decapoda: Grapsidae). *J Exp Biol*, 210(Pt 5):865–80.

Oliva, D. and Tomsic, D. (2012). Visuo-motor transformations involved in the escape response to looming stimuli in the crab neohelice (= chasmagnathus) granulata. *Journal of Experimental Biology*, 215(19):3488–3500.

O'Malley, D. M., Kao, Y. H., and Fetcho, J. R. (1996). Imaging the functional organization of zebrafish hindbrain segments during escape behaviors. *Neuron*, 17(6):1145–55.

Orger, M. B., Kampff, A. R., Severi, K. E., Bollman, J. H., and Engert, F. (2008). Control of visually guided behavior by distinct populations of spinal projection neurons. *Nature Neuroscience*, 11(3):327–333.

Parry, D. A. (1983). Labial extension in the dragonfly larva anax-imperator. *Journal of Experimental Biology*, 107(Nov).

Patterson, B., Abraham, A., MacIver, M. A., and McLean, D. (2013). Visually guided gradation of prey capture movements in larval zebrafish. *The Journal of Experimental*

Biology, 16:3071–3083.

Petzschner, F. H., Glasauer, S., and Stephan, K. E. (2015). A bayesian perspective on magnitude estimation. *Trends in cognitive sciences*, 19(5):285–293.

Preuss, T., Osei-Bonsu, P. E., Weiss, S. A., Wang, C., and Faber, D. S. (2006). Neural representation of object approach in a decision-making motor circuit. *The Journal of Neuroscience*, 26(13):3454–3464.

Prevedel, R., Yoon, Y.-G., Hoffmann, M., Pak, N., Wetzstein, G., Kato, s., Schroedel, T., Rasker, R., Zimmer, M., Boyden, E. S., and Vaziri, A. (2014). Simultaneous whole-animal 3d imaging of neuronal activity using light-field microscopy. *Nature Methods*, 11(7):727–730.

Pritchard, G. (1965). Prey capture by dragonfly larvae (odonata - anisoptera). *Canadian Journal of Zoology - Back Year Project*, 43(2):271–+.

Riechert, S. E. (1978). Games spiders play - behavioral variability in territorial disputes. *Behavioral Ecology and Sociobiology*, 3(2):135–162.

Rind, F. C. and Simmons, P. J. (1999). Seeing what is coming: building collision-sensitive neurones. *Trends Neurosci*, 22(5):215–20.

Roberts, A., Borisyuk, R., Buhl, E., Ferrario, A., Koutsikou, S., Li, W.-C., and Soffe, S. R. (2019). The decision to move: response times, neuronal circuits and sensory memory in a simple vertebrate. *Proceedings of the Royal Society B*, 286(1899):20190297.

Santer, R. D. (2013). Motion dazzle: a locust's eye view. *Biol Lett*, 9(6):20130811.

Santer, R. D., Rind, F. C., Stafford, R., and Simmons, P. J. (2006). Role of an identified looming-sensitive neuron in triggering a flying locust's escape. *Journal of Neurosphysiology*, 95(6):3391–3400.

Särkkä, S. (2013). *Bayesian filtering and smoothing*, volume 3. Cambridge University Press.

Schiff, S. J. and Sauer, T. (2008). Kalman filter control of a model of spatiotemporal cortical dynamics. *BMC Neuroscience*, 9(1):O1.

Seeliger, M. W., Rilk, A., and Neuhauss, S. C. (2002). Ganzfeld erg in zebrafish larvae. *Doc Ophthalmol*, 104(1):57–68.

Severi, K. E., Portugues, R., Marques, J. C., O'Malley, D. M., Orger, M. B., and Engert, F. (2014). Neural control and modulation of swimming speed in the larval zebrafish. *Neuron*, 83(3):692–707.

Shang, C., Chen, Z., Liu, A., Li, Y., Zhang, J., Qu, B., Yan, F., Zhang, Y., Liu, W., Liu, Z., et al. (2018). Divergent midbrain circuits orchestrate escape and freezing responses to looming stimuli in mice. *Nature communications*, 9(1):1232.

Sherk, T. E. (1978). Development of the compound eyes of dragonflies (odonata). ii. development of the larval compound eyes. *J Exp Zool*, 203(1):47–60.

Shimazaki, T., Tanimoto, M., Oda, Y., and Higashijima, S.-i. (2019). Behavioral role of the reciprocal inhibition between a pair of mauthner cells during fast escapes in zebrafish. *Journal of Neuroscience*, 39(7):1182–1194.

Sillar, K. T., Picton, L. D., and Heitler, W. J. (2016). *The Neuroethology of Predation and Escape*. Wiley.

Snodgrass, R. E. (1954). *The dragonfly larva.* Smithsonian miscellaneous collections,. Smithsonian Institution, Washington.

Snyder, J. B., Nelson, M. E., Burdick, J. W., and MacIver, M. A. (2007). Omnidirectional sensory and motor volumes in an electric fish. *PLoS Biology*, 5(11):2671–2683.

Soto, A., Stewart, W. J., and McHenry, M. J. (2015). When optimal strategy matters to prey fish. *Integrative and Comparative Biology*, 55(1):110–20.

Sperling, E. A., Frieder, C. A., Raman, A. V., Girguis, P. R., Levin, L. A., and Knoll, A. H. (2013). Oxygen, ecology, and the Cambrian radiation of animals. *Proc. Natl. Acad. Sci. U.S.A.*, 110(33):13446–13451.

Stewart, W. J., Cardenas, G. S., and McHenry, M. J. (2013). Zebrafish larvae evade predators by sensing water flow. *J Exp Biol*, 216(Pt 3):388–98.

Stewart, W. J. and McHenry, M. J. (2010). Sensing the strike of a predator fish depends on the specific gravity of a prey fish. *J Exp Biol*, 213(Pt 22):3769–77.

Stewart, W. J., Nair, A., Jiang, H., and McHenry, M. J. (2014). Prey fish escape by sensing the bow wave of a predator. *J Exp Biol*, 217(Pt 24):4328–36.

Sun, H. and Frost, B. J. (1998). Computation of different optical variables of looming objects in pigeon nucleus rotundus neurons. *Nat Neurosci*, 1(4):296–303.

Tabor, K. M., Bergeron, S. A., Horstick, E. J., Jordan, D. C., Aho, V., Porkka-Heiskanen, T., Haspel, G., and Burgess, H. A. (2014). Direct activation of the Mauthner cell by electric field pulses drives ultrarapid escape responses. *J Neurophysiol*, 112(4):834–44.

Tanaka, Y. and Hisada, M. (1980). The hydraulic mechanism of the predatory strike in dragonfly larvae. *Journal of Experimental Biology*, 88(Oct).

Tanouye, M. A. and Wyman, R. J. (1980). Motor outputs of giant nerve fiber in drosophila. *J Neurophysiol*, 44(2):405–21.

Tappeiner, C., Gerber, S., Enzmann, V., Balmer, J., Jazwinska, A., and Tschopp, M. (2012). Visual acuity and contrast sensitivity of adult zebrafish. *Frontiers in zoology*, 9(1):10.

Temizer, I., Donovan, J. C., Baier, H., and Semmelhack, J. L. (2015). A Visual Pathway for Looming-Evoked Escape in Larval Zebrafish. *Curr. Biol.*, 25(14):1823–1834.

Traynelis, S. F. and Jaramillo, F. (1998). Getting the most out of noise in the central nervous system. *Trends in neurosciences*, 21(4):137–145.

Trivedi, C. A. and Bollmann, J. H. (2013). Visually driven chaining of elementary swim patterns into a goal-directed motor sequence: a virtual reality study of zebrafish prey capture. *Frontiers in Neural Circuits*, 7(86).

Tümpel, S., Wiedemann, L. M., and Krumlauf, R. (2009). Hox genes and segmentation of the vertebrate hindbrain. *Current topics in developmental biology*, 88:103–137.

von Reyn, C. R., Breads, P., Peek, M. Y., Zheng, G. Z., Williamson, W. R., Yee, A. L., Leonardo, A., and Card, G. M. (2014). A spike-timing mechanism for action selection. *Nat Neurosci*, 17(7):962–70.

von Reyn, C. R., Nern, A., Williamson, W. R., Breads, P., Wu, M., Namiki, S., and Card, G. M. (2017). Feature integration drives probabilistic behavior in the drosophila escape response. *Neuron*, 94(6):1190–1204.

Wainwright, P., Carroll, A. M., Collar, D. C., Day, S. W., Higham, T. E., and Holzman, R. A. (2007). Suction feeding mechanics, performance, and diversity in fishes. *Integr Comp Biol*, 47(1):96–106.

Walker, J. A., Ghalambor, C. K., Griset, O. L., McKenney, D., and Reznick, D. N. (2005). Do faster starts increase the probability of evading predators? *Functional Ecology*, 19(5):808–815.

Wang, W. C. and McLean, D. L. (2014). Selective responses to tonic descending commands by temporal summation in a spinal motor pool. *Neuron*, 83(3):708–21.

Webb, P. W. (1986). Effect of body form and response threshold on the vulnerability of 4 species of teleost prey attacked by largemouth bass (micropterus-salmoides). *Canadian Journal of Fisheries and Aquatic Sciences*, 43(4):763–771.

Weihs, D. and Webb, P. W. (1984). Optimal avoidance and evasion tactics in predator-prey interactions. *Journal of Theoretical Biology*, 106(2):189–206.

Will, U. (1991). Amphibian mauthner cells (part 1 of 2). *Brain, Behavior and Evolution*, 37(5):317–324.

Wilson, R. and Finkel, L. (2009). A neural implementation of the kalman filter. In *Advances in neural information processing systems*, pages 2062–2070.

Wolpert, D. M. and Ghahramani, Z. (2000). Computational principles of movement neuroscience. *Nature neuroscience*, 3(11s):1212.

Wu, L. Q., Niu, Y. Q., Yang, J., and Wang, S. R. (2005). Tectal neurons signal impending collision of looming objects in the pigeon. *Eur J Neurosci*, 22(9):2325–31.

Wu, W., Gao, Y., Bienenstock, E., Donoghue, J. P., and Black, M. J. (2006). Bayesian population decoding of motor cortical activity using a kalman filter. *Neural computation*, 18(1):80–118.

Yager, D. D. (2012). Predator detection and evasion by flying insects. *Curr Opin Neurobiol*, 22(2):201–7.

Yamamoto, K., Nakata, M., and Nakagawa, H. (2003). Input and output characteristics of collision avoidance behavior in the frog rana catesbeiana. *Brain, behavior and evolution*, 62(4):201–211.

Ydenberg, R. C. and Dill, L. M. (1986). The economics of fleeing from predators. *Advances in the Study of Behavior*, 16:229–249.

Zemel, R. S., Dayan, P., and Pouget, A. (1998). Probabilistic interpretation of population codes. *Neural computation*, 10(2):403–430.

Zottoli, S. J. (1977). Correlation of startle reflex and Mauthner cell auditory responses in unrestrained goldfish. *Journal of Experimental Biology*, 66(Feb):243.

APPENDIX A

Visual threat assessment and reticulospinal encoding of calibrated responses in larval zebrafish

A.1. Free swimming looming stimulus assay

Larval zebrafish were placed in a smaller dish filled with system water within a larger dish (Figure 2.1) and allowed to acclimate for 15 min before any experiments were performed. A cap made from a microscope coverslip (United Scope, Irvine, CA) was placed on the smaller dish to contain the fish and the larger dish was also filled with system water. A diffusive filter (Anchor Optics, Barrington, NJ) was affixed to the wall on one-half of the larger dish to create a projection screen. Looming stimuli were generated with Psychtoolbox Kleiner et al. (2007) within MATLAB and projected onto the diffusive filter with a 500 lumen portable LED projector (Optoma USA, Freemont, CA, USA) placed 40 cm from the dish. The actual looming object was always projected onto the center of the projection screen. However, the relative azimuthal angle of the stimulus depended upon the orientation of the freely swimming fish within the smaller dish (Figure A.1). Any deviations in the percept of the subtended angle of the looming stimulus from the intended due to fish position and orientation were found to be ≤ 10% for the large majority of cases (Figure A.2).

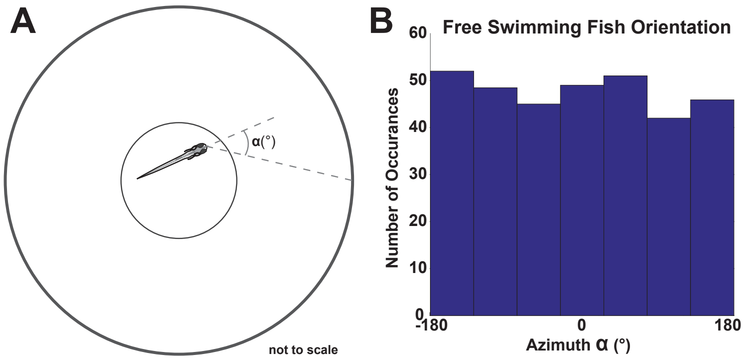

Figure A.1. Fish were equally likely to be oriented ±180° from stimulus.

Figure A.1 details: Related to Figure 2.1. A) After an acclimation period, the azimuth was measured for 15 different instances of stasis during free swimming for 21 fish. Not to scale. B) The azimuth is effectively distributed uniformly from ±180°.

We verified that the fish were equally likely to be oriented in any direction ±180° from the center of the screen. To do so we placed a larval fish in the smaller dish of the dish-within-dish design while projecting uniform illumination onto the curved screen and allowed the fish to acclimate for 15 min. After this period, the large majority of larval fish would perform free swimming at a rate of about 1 swim bout every 1 – 2 s. During this time, a single image was taken approximately every 1 min when the fish was stationary and repeated 15 times. This was repeated with 21 fish to acquire a total of 315 images.

The relative azimuthal angle to the center of the screen was measured (Figure A.1A) from these 315 images. The distribution of relative azimuthal angle between ±180° was not significantly different from a uniform distribution (Figure A.1B, Kolmogorov-Smirnov test, $p = 0.8$). The fish orientation and therefore, this relative azimuthal angle was hand-tracked with the aid of MATLAB for all looming evoked-responses.

The fish was placed within a smaller dish since the looming stimulus was quantified with respect to the center of the larger dish (Figure 2.1B). As seen in Figure A.2A, based on the position of the larval fish within the smaller dish, there can be a small error in determining the angular size of the looming stimulus. This error was quantified for the geometry of the specific case used in this study of a smaller 10 mm dish within a larger 65 mm dish.

$$\text{PE} = 100 \times \frac{\theta\prime - \theta}{\theta} \tag{A.1}$$

We used MATLAB to generate 1000 random positions within the smaller dish with uniform likelihood. Then we used basic trigonometry to determine $\theta\prime$ for those positions for specific fixed θs. Therefore, for each θ, we did Monte Carlo sampling of 1000 $\theta\prime$s. We can define a term called percent error (PE) using Equation A.1 which is a measure of percent difference from the actual intended angular size.

As can be inferred from Figure A.2B the mean percent error for all object sizes was nearly zero. The distribution of percent error was very similar for objects of different angular sizes. From these distributions, we found that the angular estimation percent error was within ±10% for 95% of all positions randomly generated within the smaller dish. Additionally, the standard deviation of percent error can provide insight into the extent of the estimation error due to fish position (Figure A.2C). The largest standard deviation of 6.13% in percent error was for the smallest object simulated with angular width of 3°. Figure A.2B shows that the standard deviation in percent error reduces slightly but obviously with increasing angular size indicating a small overall reduction in angular estimation error with larger objects.

The looming object was a black expanding square on a blue background of stationary, low-contrast rectangles. The position and size of the low contrast rectangles in the background were randomly generated for each trial. A blue background was used instead of a white

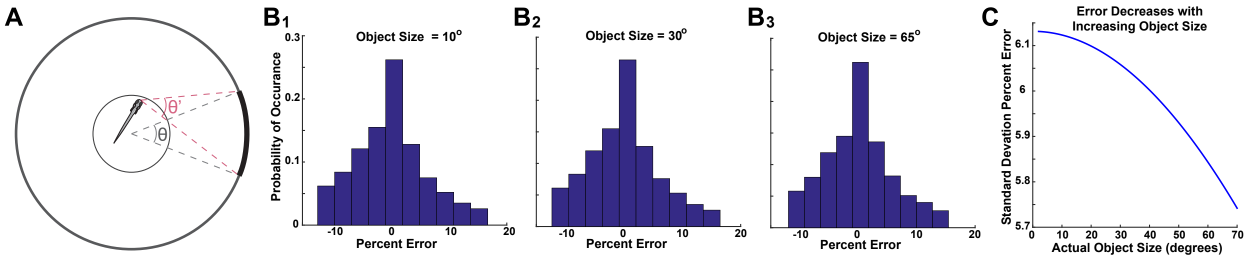

Figure A.2. Error in determining angular size of the stimulus.

background, since a white background would introduce ambient green light creating an issue when similar stimuli were used later during fluorescence imaging of Calcium Green Dextran in the Mauthner cell (M-cell). Therefore, all virtual looming stimuli presented in this study were black expanding squares on a blue background for the sake of consistency.

Figure A.2 details: Related to Figure 2.1. A) The looming stimulus (θ), on the walls of the larger dish, expands at a rate determined by the looming stimulus parameters with respect to the center of both dishes. However, the position of the fish within the smaller dish (dashed circle) can alter angular size estimation ($\theta\prime$). Not to scale. B1 - 3) Histograms demonstrating the distribution of PE for objects of different angular sizes. The distributions are very similar. C) Plot showing that the standard deviation of percent error reduces slightly with increasing angular size with the largest being less than 6.15%.

After 15 min of acclimation in the free swimming assay, a leftward moving grating and a rightward moving grating were each presented for 12 s to elicit visually-evoked turning behavior to ensure that the fish was performing visuo-motor behaviors. If a fish did not respond to these gratings with leftward and rightward turns, then it was not used for further experimentation. After successful preliminary testing with the moving grating, each fish was shown 10 randomly generated looming stimuli with at least 2 min intervals between each stimulus presentation during which a static dot-field was projected onto the screen. During a given stimulus, a static black square appeared on a blue background of low-contrast rectangles and started expanding after 2 s. Fish rarely swam during the 2 s of static black square presentation; if they did, that trial of the looming stimulus was discarded. The relevant ranges for looming stimulus parameters were determined from prior work by other researchers Stewart et al. (2014) who performed high-speed imaging of juvenile and adult zebrafish hunting larval zebrafish (see text for details). Since L (Figure 2.1B) was pseudorandomly selected to be between 10 – 25 mm, this determined the initial size of the projection of the black square on the dish surface. For instance, a 10 mm virtual looming stimulus which is at a virtual distance of 50 mm would be a 6.5 mm projection on the dish surface that is 32.5 mm away. After 2 s to static presentation, this square then expanded to simulate the percept of the virtual looming object.

To observe the looming-evoked behavior of zebrafish larvae in our assay, videos were recorded using a high-speed camera (FASTCAM 1024 PCI; Photron, San Diego, CA, USA) attached to a dissection microscope (Stemi-2000; Carl Zeiss Microscopy, Thornwood, NY, USA). Images were collected at 250 fps at 2X magnification. Even though we were limited to 250 fps as the fastest sampling rate due to the size of our imaging buffer, the tail angle velocities (Figure 2.3F) suggest that the 3 ms of missing kinematics data in-between frames could produce at most a 12 – 18 degree error in measuring heading direction. This upper bound of error is well within the spread of the heading directions observed to looming stimuli (Figure 2.2C) and produces a binning effect on the data which does not influence the main conclusions of the study. Illumination was provided from above with 850 nm infrared light from two LED arrays each composed of 30 LEDs with each LED at a brightness of 50 mcd (SparkFun, Niwot, CO, USA). At the start of the looming stimulus expansion, MATLAB

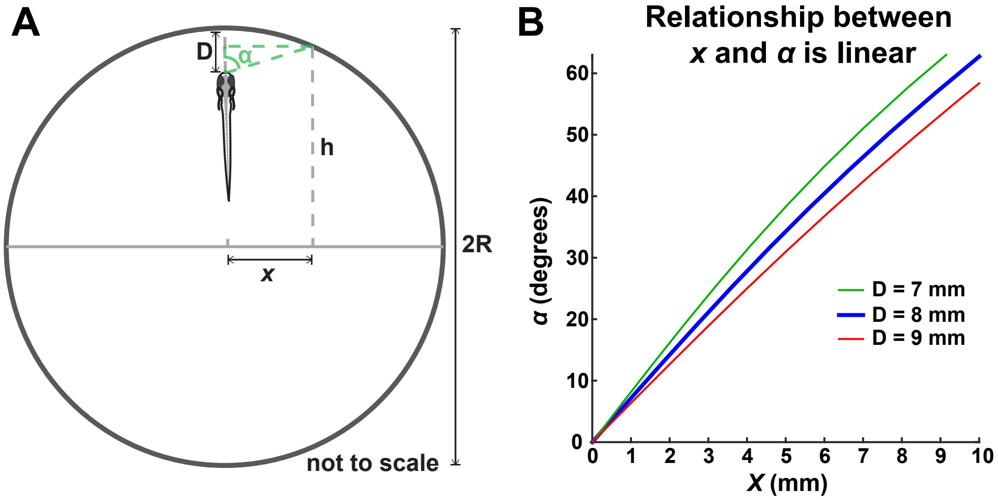

Figure A.3. Stimulus correction for uncentered fish under partial restraint.

triggered the start of acquisition by the high-speed imaging system. Total head yaw during the initial bend was measured by hand-tracking heading vectors with the aid of MATLAB for all looming-evoked responses. The head yaw velocity was computed by dividing the total change in angular orientation of the fish head during the initial bend by the duration of the initial bend.

A.2. Partially-restrained looming stimulus assay

Figure A.3 details: Related to Figure 2.3. A) Demonstrates the parameters relevant to make corrections for the uncentered fish in the partially restrained looming stimulus set up. Not to scale. B) Plots the relationship between x and α for the specific geometry in this study. Note that it is near linear.

Larval fish at 5–6 dpf were restrained by embedding them in ~2% low melting point agarose (Invitrogen, Carlsbad, CA, USA). Larvae were mounted in a 38 mm Petri dish with their anterior-posterior axis aligned to the radius of the dish and the center of their head 8 mm from the wall. Once the agarose had set, it was covered with system water and a scalpel was used to dissect sections of the agar away so as to permit free movement of the eyes and the tail. The only part of the larvae that remained embedded in agarose was from the otic vesicle to the posterior end of the swim bladder. Larvae were acclimated in the agarose for 24 hr at 28.5°C and tested at 5 – 7 dpf. A diffusive filter (Anchor Optics, Barrington, NJ, USA) was affixed to the wall of the Petri dish to produce a projection screen directly in front of the fish. The dish was placed on a microscope stage and illuminated from below with 850 nm infrared light from two LED arrays mentioned earlier (SparkFun, Niwot, CO, USA). Larvae were imaged from below through a lowpass infrared filter (>720 nm, FM03, Thorlabs, Newton, NJ, USA) and 4 × microscope objective (AmScope, Irvine, CA, USA) at 1000 fps using a high-speed camera (FASTCAM 1024 PCI; Photron, San Diego, CA, USA).

Looming stimuli were generated with Psychtoolbox Kleiner et al. (2007) within MATLAB and projected onto the diffusive filter with a 500 lumen portable LED projector (Optoma USA, Freemont, CA, USA) placed 15 cm from the dish. Since the fish was placed 8 mm from the dish wall, the azimuthal angle of the looming stimuli and its angular size were not as would be expected for a fish placed at the center of the dish (19 mm from the dish wall). This was corrected for computationally when generating the looming stimuli by deriving a formula to make the azimuthal angle and looming rate comparable to the free swimming assay (Figure A.3).

In the partially restrained assay, the fish was placed ~8 mm (D in Figure A.3A) from the screen — the edge of the 38 mm (2R in Figure A.3A) dish — since this greatly increased the likelihood of responding to visual stimuli as opposed to being at the center (19 mm away).

Due to this placement closer to the screen, the azimuthal angle of the looming stimuli and its angular size were not as would be expected for fish placed at the center of the dish.

We found the mathematical relationship between α, the azimuthal angle of the stimulus, and x, its radial position along the centerline (Figure A.3A). Looming stimuli generated at a certain x position would then have a known azimuthal position from the perspective of the fish. This calculation was completed with simple trigonometry by determining the dimensions of the green triangle in Figure A.3A. One of the legs of that right-angled triangle is already known to be x but the other leg, hereafter referred to as k, can also be determined. h can be rewritten as -

$$h = \sqrt{R^2 - x^2}$$

D is composed of k, the unknown leg of the green triangle, and a smaller piece, u

$$D = k + u$$

where,

$$u = R - h$$

restated,

$$u = (R - \sqrt{R^2 - x^2})$$

k can be written as

$$k = D - u$$

restated,

$$k = D - (R - \sqrt{R^2 - x^2})$$

Therefore, the azimuthal angle α can be stated as

$$\alpha = \arctan\frac{x}{k}$$

restated,

$$\alpha = \arctan\frac{x}{D-(R-\sqrt{R^2-x^2})}$$

Figure A.3B, plots the relationship between α and x as stated in the previous equation for the specific geometry in this study of $R = 19$ mm and $D = 8$ mm. Fish were only shown stimuli with azimuthal angle between ±60°. This relationship is very well explained by simple linear relationship between where $\alpha = 6.27x$ ($R^2 = 0.99$). Additionally, the plots for $D = 7$ mm and 9 mm are also shown to demonstrate that the changes with errors in fish placement are not large. The existence of a linear relationship between x and α significantly simplified the azimuthal angle positioning of looming stimuli. The looming expansion rate was also corrected for the partially restrained assay using this linear relationship between x and α.

Partially restrained fish were shown randomly generated looming stimuli within the same parameter ranges as used for freely swimming fish. This was done to compare the statistics of stimuli effective in producing looming-evoked responses and the time remaining to collision. Only responses to rostrally-approaching looming stimuli (within ±45°) from the freely swimming case were used since this was the range within which virtual stimuli were presented.

MANOVA (multivariate analysis of variance) testing of L/V, L, azimuth of approach, and time remaining to collision from the partially restrained ($n = 143$) and freely swimming ($n = 85$) groups produced $p = 0.43$ indicating that the two groups are not significantly different.

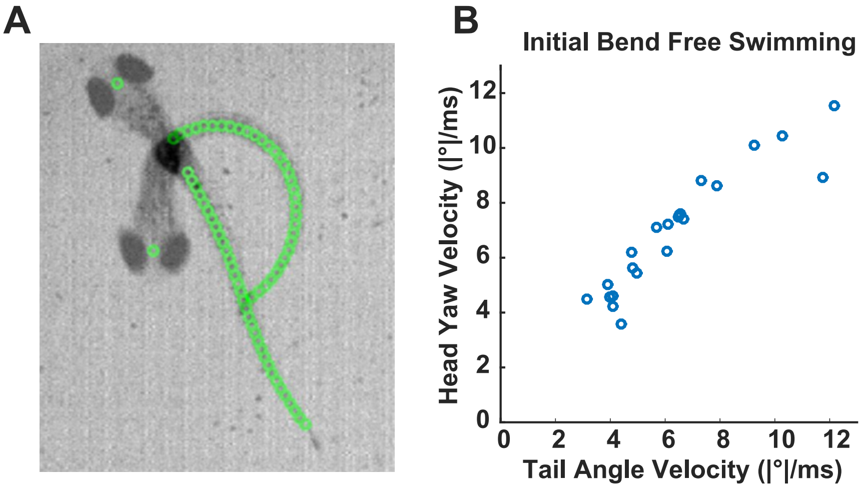

Figure A.4. Initial bend tail angle velocity and head yaw velocity are highly correlated.

Therefore, partial restraint does not significantly change the effective looming stimuli, the timing of the looming-evoked response, or the correlations between the different variables.

Since MANOVA assumes normality, the univariate non-parametric two sample Kolmogorov-Smirnov (KS) test was also used to test each variable separately from the partially restrained and freely swimming categories. As seen in the list below, the KS tests of individual variables did not produce significant results either. All of these non-significant p-values seem to suggest that the partially restrained fish are performing a naturalistic looming-evoked response.

KS Test Results Comparing Free Swimming and Partially Restrained Fish

- Time Remaining to Collision: $p = 0.53$
- Azimuth of Approach: $p = 0.17$
- L/V: $p = 0.5586$
- L: $p = 0.84$

Figure A.4 details: Related to Figure 2.3. A) Overlay of the fish body at the start of the escape response and at the end of the initial bend. B) Demonstrates the linear correlation between the tail angle velocity and the average head yaw velocity during the initial bend.

The correlation between head yaw velocity and tail angle velocity was verified in free-swimming fish by performing automated body tracking with a MATLAB image processing code of 19 free swimming escape responses of larval zebrafish out of the 246 collected. Not all escape responses could be successfully tracked in entirety since the fast moving tail would sometimes be blurred in the videos recorded at 250 fps. From these 19 fully tracked responses, the tail angle was measured and the average tail angle velocity during the initial bend was computed. The average head yaw velocity of the free swimming fish during the initial bend was also computed. As seen in Figure A.4B, the average tail angle velocity is highly correlated with average head yaw velocity during the initial bend ($R = 0.94$, $p \lll 0.001$). Furthermore, the tail angle velocities measured for partially restrained fish were within the range of tail angle velocities found in free swimming fish indicating a congruency in the kinematics of the response.

Fish were similarly tested with a leftward and then rightward moving grating to ensure they were performing visuomotor behaviors before any presentations of looming stimuli. After successful preliminary testing with moving gratings, fish were shown 10 randomly generated looming stimuli with at least 2 min between each stimulus presentation. The specific stimulus parameters were randomly chosen to be within the same range as in the free swimming case. We noted that partially-restrained fish were half as likely to respond to looming stimuli than free swimming fish. However, the range of looming stimulus parameters effective in producing a response and the timing of the response were not significantly different from the free swimming case, as shown above.

MATLAB triggered the start of high-speed imaging acquisition at the start of looming stimulus expansion. A custom MATLAB program was used to track 22 points along the fih body. Of the 22 points, 1 point was positioned between the two eyes and 21 points ranged from the caudal end of the swim bladder to the end of the tail. These points were then used to determine the tail angle. The absolute average tail angle velocity was also computed which is the absolute value of the total change in the tail angle over the course of the initial bend divided by the duration of the initial bend. The average tail angle velocity during the initial bend was measured since it was found to be highly correlated to head yaw velocity in freely swimming fish (Figure A.4).

Features from the propulsive stage were also extracted for the partially restrained fish. Average tail beat frequencies were computed by measuring the duration of each tail cycle in the propulsive stage, calculating the frequency for each cycle, and taking the average for each response. The average absolute tail angle velocity was computed by measuring the absolute total change in tail angle for each tail beat (half of a tail cycle) in the propulsive stage, dividing by the duration of the tail beat, and taking the average for each response.

A.3. Calcium imaging in the Mauthner cell

Figure A.5 details: Related to Figure 2.4. Overlaid histograms of DF/F values from fluorescence traces of M-cells from all looming-evoked responses separated into the portion of the trace before the time-of-response and the portion after. The arrow points at the decision threshold used in this study.

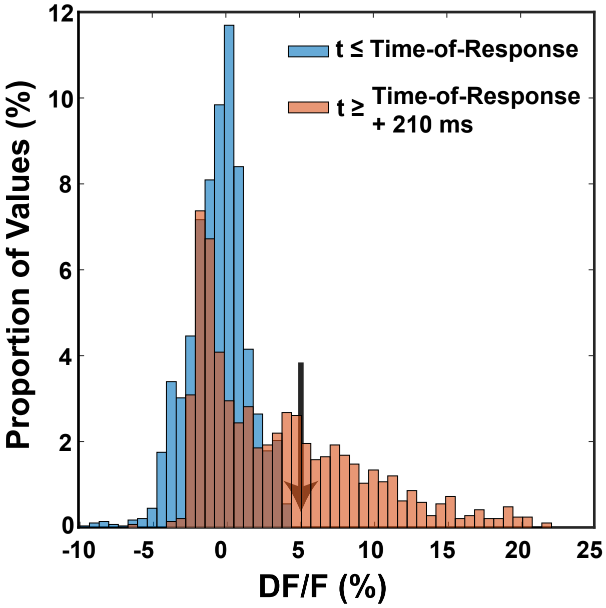

Figure A.5. ΔF/F threshold for neuron recruitment.

Four-day-old larval zebrafish were anesthetized with 0.02% 3-aminobenzoic acid ethyl ester (Sigma Aldrich, St. Louis, MO). The M-cell was retrogradely labeled by pressure injection via a glass microelectrode of a 10% solution of Calcium Green Dextran (10,000 MW; Molecular Probes, Eugene, OR) dissolved in intracellular patch solution into the spinal cord O'Malley et al. (1996). Injections were targeted to the ventral cord to selectively label the M-cell without disrupting more dorsal sensory pathways. Since any injection would disrupt local circuits, injections were also targeted to the section of the spinal cord just caudal of the anus. After injection, the fish were allowed to recover in system water maintained at 28.5°C for 24–36 hr. The cell labeling was verified under a SteREO Discovery.V20 fluorescent stereo microscope (Carl Zeiss, Dublin, CA, USA). The best-labeled animals were retained in system water and used for behavioral trials. Before embedding in agar, the animals were examined to ensure they performed free swimming movements and tested with tactile stimuli to the head and to the end of the tail to ensure they had fully recovered from spinal injection.

Fish were partially restrained in agar and tested with looming stimuli as described previously at 5 – 7 dpf. However, during these experiments fluorescence imaging of the M-cell was performed simultaneously through a 40 × water immersion objective from above with a 4 mm working distance (Olympus, Lombard, IL, USA). Fluorescence excitation was provided by an Xcite Series 120Q lamp (Quebec City, QC, Canada) and sent through a GFP fluorescence filter (Olympus, Lombard, IL, USA). A limited aperture was used to restrict fluorescent excitation to a region around the M-cell to reduce the background fluorescence signal from adjacent areas. The fluorescence image was captured with a Q-imaging Rolera Bolt camera (Surry, BC, Canada) controlled with the μManager software Edelstein et al. (2014).

Each fish (N = 15) was shown 10 slowly approaching looming stimuli, 10 rapidly approaching looming stimuli, 5 rightward moving gratings, and 5 leftward moving gratings ordered randomly. The grating stimuli were not used for analysis but were presented only to make sure fish were responding appropriately to visual stimuli. The tail was tracked from the high-speed imaging as described earlier. A custom MATLAB program was used to track the mean pixel value of the fluorescence signal from the M-cell. A threshold was determined to classify M-cell active and M-cell inactive traces (Figure A.5).

M-cell fluorescence traces from all responses were pooled and broken into two sections – the portion of the trace before the time-of-response ($t \leq$ Time-of-Response) and the portion of the trace 210 ms after the time-of- response ($t \geq$ Time-of-Response + 210 ms). A 200 ms window during the response was left out to avoid including motion artifacts in the following analysis. The histograms of ΔF/F for these two portions for all traces are shown in Figure S5.

Since the M-cell was sometimes recruited for the response and sometimes not, the histogram of ΔF/F values after the time-of-response has values from M-cell active and inactive traces. The long tail extending to the right of larger ΔF/F values in the "$t \geq$ Time-of-Response + 210 ms" histogram is due to increased calcium activity in the M-cell active traces. The decision threshold used in this study is marked with an arrow in Figure A.5. This value was visually determined since there are no occurrences of ΔF/F values above this threshold for the "$t \leq$ Time-of-Response," when the M-cell is assumed to be inactive. This threshold provided a quantitative method of selecting M-cell active and silent responses.

The likelihood of recruiting the M-cell based on stimulus paradigm was computed by measuring the proportion of M-cell active responses from each fish ($N = 15$) according to fast or slow approach and averaging across all fish.

A.4. Light field microscopy of reticulospinal neurons

Figure A.6 details: Related to Figure 2.5. A) microlens array fixed to a flip mount was placed at the imaging plane of the microscope camera port and a CMOS camera imaged the back focal plane of the array. The flip mount allowed switching between light field and epifluorescence imaging. B1) Example of a light field image acquired through the system demonstrating the image of microlenses. B2) Volume reconstruction was performed by computing multiple focal planes using the lightfield reconstruction algorithm. B3) Striping artifacts were removed from the planes near the center of the reconstructed volume using an established algorithm. B4) Time-varying light field volumes were registered to a single epifluorescence volume collected before the start of the experiments. B5) Segmentation and blob detection via thresholding was used to

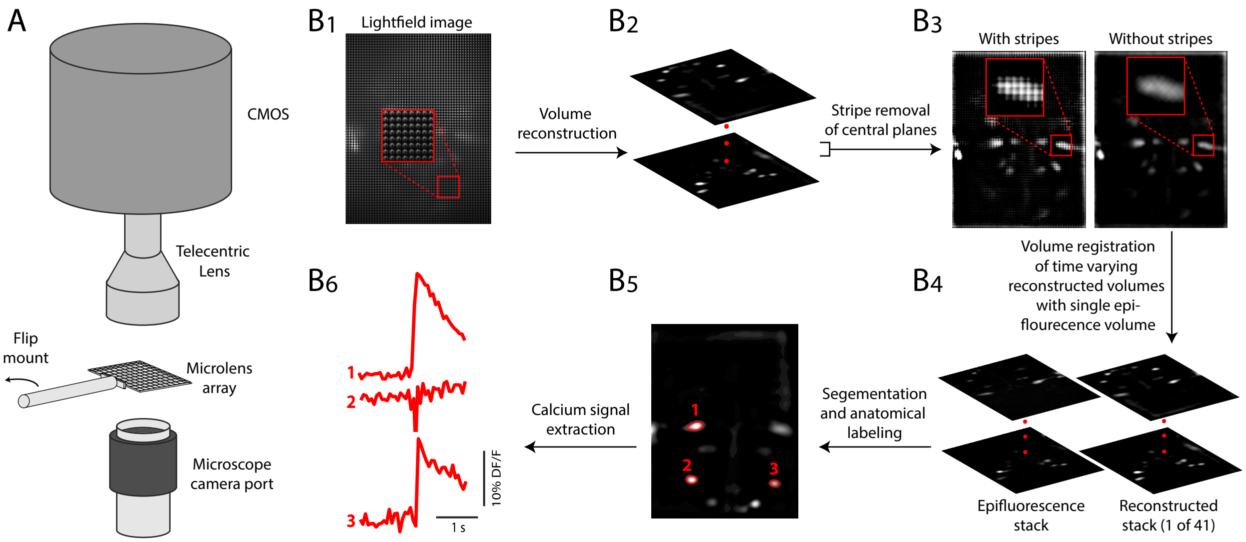

Figure A.6. Light field microscopy of reticulospinal neurons.

identify cellular regions within specific focal planes. These regions were anatomically labeled by hand. B6) The mean pixel value within these regions were calculated over time and normalized to arrive at the time-varying calcium signals from each cell.

Fish larvae were injected with Calcium Green Dextran and partially restrained in agar as previously described. The same microscope objective, fluorescence excitation lamp, and camera were used but a microlens array (RPC Photonics, Rochester, NY) with 125 μm pitch, f/25, and a focal length of 3040 μm was placed in the imaging plane of the camera port (Figure S6). The back focal plane of the microlens array was then imaged with the camera through a 0.5X telecentric lens (Edmund Optics, Barrington, NJ). This is the standard construction of the light field microscope as described in previous literature Broxton et al. (2013); Prevedel et al. (2014).

A light field microscope allows for the computational reconstruction of entire volumes from an image taken at a single plane (Figure A.6), making it possible to perform volumetric imaging at the frame rate of the camera. This comes at a loss in spatial resolution over standard epifluorescence microscopy. The spatial resolution of a light field microscope can be estimated by dividing the microlens pitch diameter with the magnification of the microscope objective, 3.125 μm in our case. A full discussion of the limitations and possibilities of the light field microscope is outside of the scope of this study but can be found in existing literature Prevedel et al. (2014).

In the design used in this study, the microlens array was fixed to a flip mount allowing for simple alternation between light field and standard epifluorescence imaging. This made it possible to take a higher spatial resolution epifluorescence focal stack of the volume of interest before collecting light field movies during behavior. A single epifluorescence focal stack was taken of the reticulospinal array at 2 μm steps for a total of a 100 μm depth (51 images total) before the start of every experiment.

Light field movies were collected at 15 fps at the center of the volume of interest during the looming-evoked response. Already existing post-processing software developed by other researchers Prevedel et al. (2014) was modified to automate reconstruction of full volumes from light field movies (Figure A.6). Computational volume reconstruction was also performed at 2 μm steps for a total of a 100 μm depth (51 total reconstructed planes). Volume reconstructions were only computed for light field images collected ±1 s around the looming-evoked response due to the computationally expensive nature of the reconstruction method.

Light field reconstruction of volumes produces striping artifacts in the planes near the center of the volume where the light field is collected Broxton et al. (2013). We addressed this by not using the central reconstructed plane of the volume for any analysis. Furthermore, we used a highly effective and previously established combined wavelet and Fourier filtering method for stripe removal in images Beat et al. (2009) for the other reconstructed planes ±14 μm around the center of the volume (Figure A.6).

These lower spatial resolution time-varying volumes were then registered with the single higher spatial resolution epifluorescence focal stack taken before the start of the experiment (Figure A.6). This volume registration was performed with MATLAB code and volume registration functions native to MATLAB. Results of the volume registration were verified by comparing locations of reticulospinal nuclei in the planes of the epifluorescence focal stack as determined from image segmentation via thresholding with the locations of the same nuclei in the planes of the reconstructed volume from light field imaging.

Segmented regions representing reticulospinal nuclei in the planes of the reconstructed volume were identified and labeled by hand (Figure A.6). The mean pixel value of the fluorescence signal in these segmented regions was calculated over time (Figure A.6). One threshold was determined to classify active versus inactive traces for all nuclei in the same way as previously described just for Mauthner cells. Calcium signal traces from all nuclei were grouped together and split into regions before and after the timing of the looming evoked response. The histograms of ΔF/F for these two portions were used to determine the activity threshold. The Mauthner cell activity dependent probability of recruiting a given reticulospinal nucleus was computed by measuring the proportion of responses for which the ΔF/F reached above threshold for each fish, grouping them according to Mauthner-active and Mauthner-silent looming-evoked escapes, and then averaging across fish.

Due to the large number of samples and different categories for Figure 2.5, the sample number for each group is listed in the tables below.

	N_{trials} for Figure 2.5B and C			
	M-cell silent		M-cell active	
Nucleus name	Ipsilateral	Contralateral	Ipsilateral	Contralateral
M-cell	35	35	50	50
MiD2	30	30	41	41
MiD3	32	33	44	46
RoV3	25	25	34	34
MiR1	28	31	36	38
MiM1	33	31	47	43
MiV1	27	27	39	39
MiR2	26	26	35	35
MiV2	33	32	45	42

	N_{fish} for Figure 2.5D			
	M-cell silent		M-cell active	
Nucleus name	Ipsilateral	Contralateral	Ipsilateral	Contralateral
M-cell	17	17	17	17
MiD2	13	13	13	13
MiD3	14	15	14	15
RoV3	8	5	8	5
MiR1	10	11	10	11
MiM1	16	15	16	15
MiV1	14	14	14	14
MiR2	9	9	9	9
MiV2	16	15	16	15

APPENDIX B

Intersection of motor volumes determines outcome of predator-prey interactions

B.1. Behavior recordings

All recordings of behavior were performed at room temperature (24°C) system water. Five dragonfly nymphs of approximately the same size were selected (nymph body length mean ± std = 14.5 mm ± 1.3 mm) for all experiments since dramatic differences in size could change the size of the mask and the locomotor performance of the strike. For each experiment, a single dragonfly nymph was selected and placed into an arena within a square plastic dish (25 mm width, 100 mm length, 15 mm height, Thomas Scientific, Swedesboro, NJ, USA) with room temperature system water and allowed to acclimate for 15 minutes. The arena constrained the dragonfly nymph to move within the field of view of the dissection microscope (Stemi-2000; Carl Zeiss Microscopy, Thornwood, NY, USA). After acclimation, 1–5 larval zebrafish were introduced into the arena. To observe the strikes and fish escape responses in our assay, videos were recorded using a high-speed camera (FASTCAM 1024 PCI; Photron, San Diego, CA, USA) attached to the microscope. Images were collected at 250 fps at 1X magnification. A 100 mm long equilateral acrylic prism (Carolina Biological Supply Company, Burlington, NC) was placed at the edge of square petri dish to provide a side view perspective into the dish within the same image (Figure B.1). The orientation of the nymph and the position of the mask in top and side view were hand-tracked with the aid of MATLAB. The orientation and total head yaw for the fish during the initial bend was

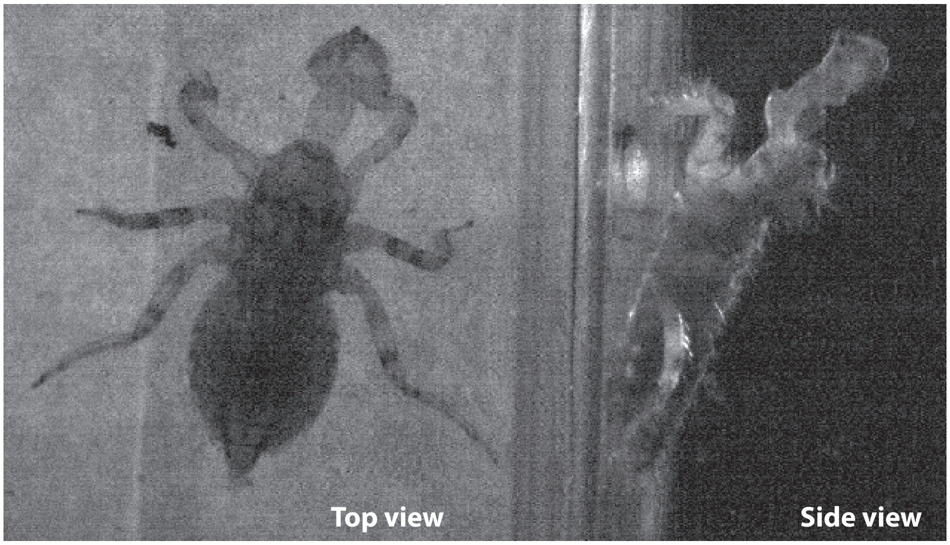

Figure B.1. Top and side view of strikes.

also hand-tracked in both top and side view with the aid of MATLAB. The fish was tracked during the propulsive stage with an automated tracker to estimate swimming velocity for the subset of escape responses that remained within the field of view. Combining corresponding points in the top and side views into a single 3D point was trivial since both top and side views were in the same image and shared a spatial axis.

B.2. Mask motor volume model

The relative 3D position of each strike to the orientation of the dragonfly nymph body was computed with vector mathematics. Each point in the 3D point cloud of strike positions was associated with a mask extension time. Native functions in MATLAB (Mathworks, Natick, MA) were used to train a k-nearest neighbor model to predict the mask extension time given a 3D position. We performed 10-fold cross validation of integer values for k neighbors ranging from 1 to 10 using 90% of the dataset for training and 10% for testing to

Tactile Delay

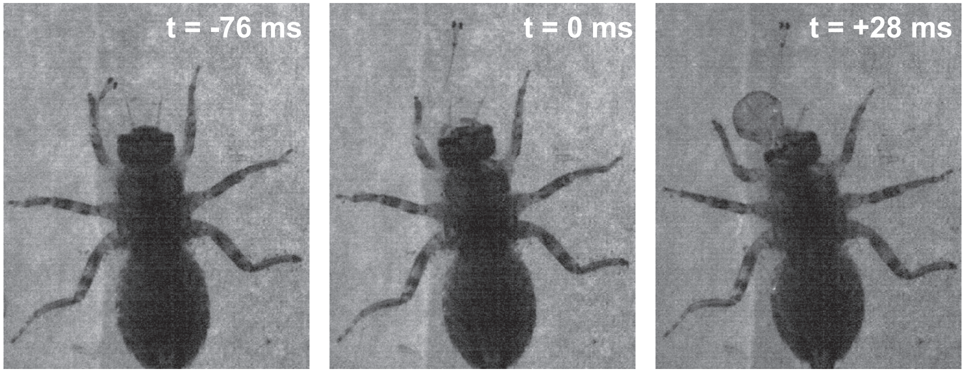

Visual delay

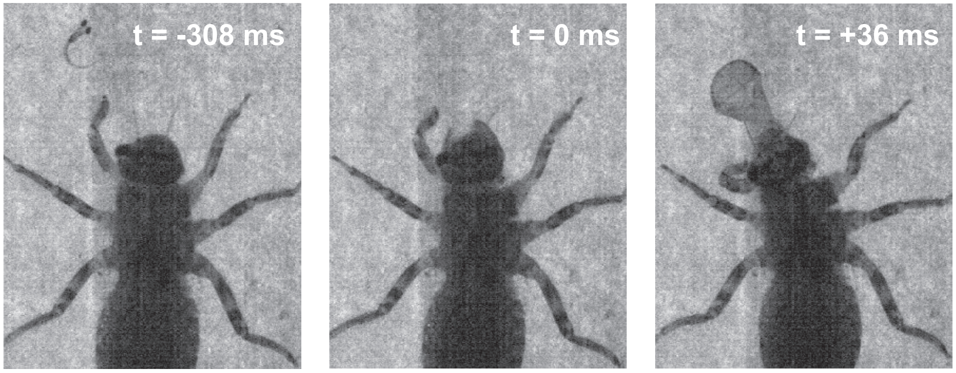

Figure B.2. Dragonfly nymphs do not intercept larval zebrafish.

find that k = 5 provided the best overall accuracy in prediction. This model trained with 5 nearest neighbors was used to generate the mask motor volume seen in Figure 3.1C.

B.3. Dragonfly nymphs do not intercept larval zebrafish

For cases where the fish was already swimming before the initiation of a strike, the nymph would strike at positions where the fish was no longer present. This was true for attacks initiated due to tactile and visual stimuli produced by swimming fish. Each case allowed for a measurement of the sensorimotor delays of the nymph by measuring the time from when the fish last inhabited the targeted position to the initiation of the strike. Sensorimotor

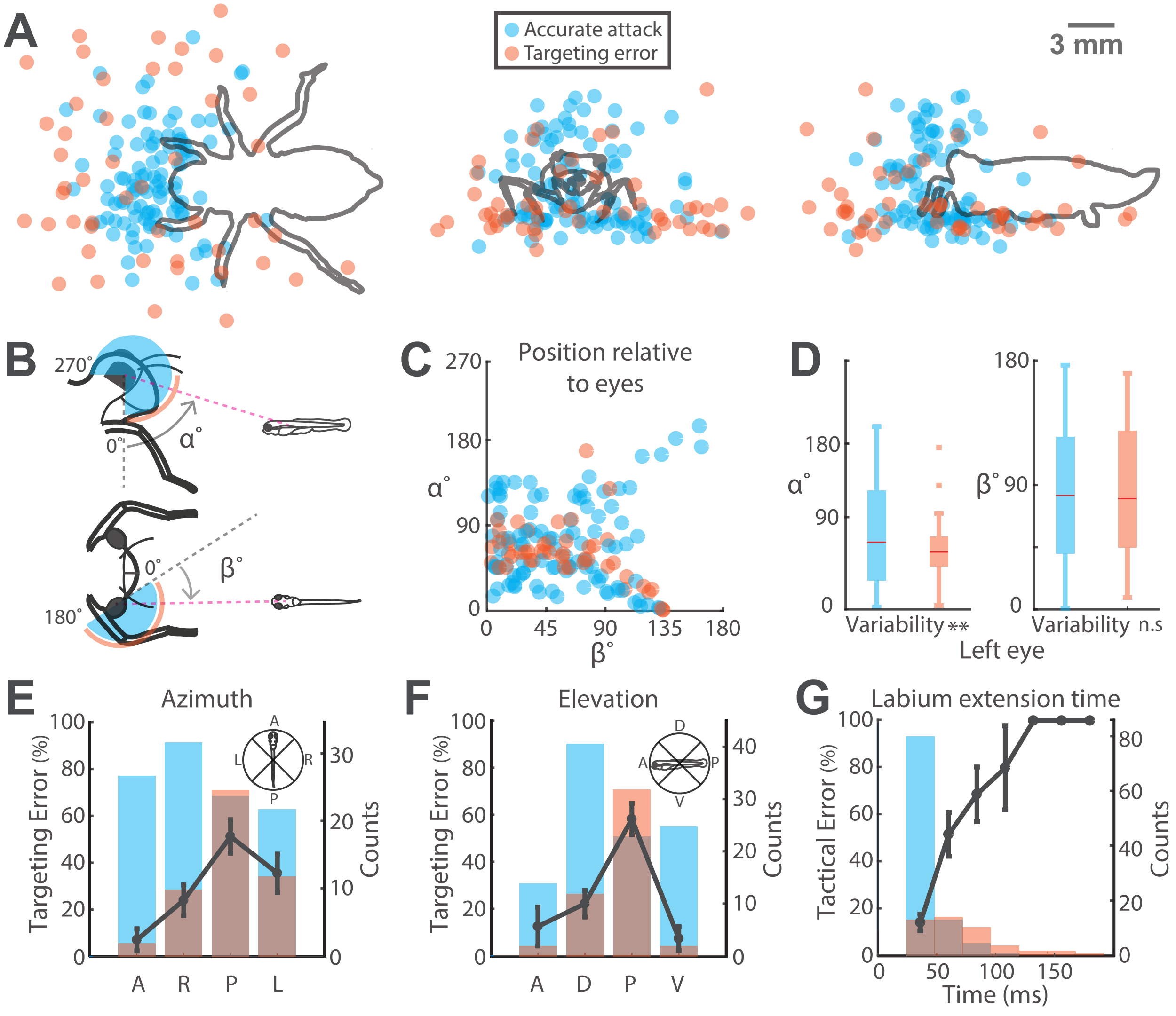

Figure B.3. Targeting errors of the dragonfly nymph

delays of the nymph for tactile stimuli: 75.5 ± 30 ms (n = 16), visual stimuli: 278 ± 110 ms (n = 5).

B.4. Targeting errors by the dragonfly nymph

A) Top (x-y), front (y-z), and side (x-z) view orthographic projections of 3D initial fish positions before the start of the strike with points colored to represent an accurate attack or a targeting error by the nymph. Legend provided in the figure. B) Diagram describing angles α and β measuring the fish swim bladder position with respect to the nymph eye. C) Scatter plots of α and β on both eyes for fish positions not in physical contact with the nymph (number of nymphs = 5, accurate attack n = 65, targeting error n = 28). D) Box-and-whisker plots demonstrating the distribution of α and β values for accurate attacks and targeting errors just for both eyes. Accurate attacks and targeting errors have significantly different variability of α values (Levene's test $p = 0.01$) but no significant difference in the medians. There is no significant difference in β values for accurate attacks and targeting errors. E) Targeting error probability based on the azimuthal position of the nymph head with respect to the fish. Azimuthal positions of the nymph were grouped by quadrants shown in the panel. Heights of each bar represent the count of strikes within that quadrant (right y-axis) and the color represents accurate attacks or targeting errors. The line plot shows the mean ± sem targeting error probability for each quadrant (left y-axis, number of nymphs = 5 for all quadrants). Nymphs are significantly more likely to make a targeting error when in azimuthal quadrant P and significantly less likely to make a targeting error when in azimuthal quadrant A (one-way anova: $p < 0.001$, pairwise Mann-Whitney U tests with Bonferroni correction: all $p < 0.01$). F) Targeting error probability based on the elevation of the nymph head with respect to the fish. Elevation positions of the nymph were grouped by quadrants shown in the panel. Heights of each bar represent the count of strikes within that quadrant (right y-axis) and the color represents accurate attacks or targeting errors. The line plot shows the mean ± sem targeting error probability for each quadrant (left y-axis, number of nymphs = 5 for all quadrants). Nymphs are significantly more likely to make a targeting error when in elevation quadrant P (one-way anova: $p < 0.001$, pairwise Mann-Whitney U tests with Bonferroni correct: all $p < 0.001$). G) Histogram demonstrating the probability of the nymph making a targeting error based on the mask extension time to the fish position. Measured mask extension times are shown for accurate attacks but mask extension times for targeting errors were estimated with the mask motor volume model. Heights of each bar represent the count of strikes within that bin (right y-axis) and the color represents accurate attacks or targeting errors. The line plot shows the mean ± sem targeting error probability for each bin (left y-axis, number of nymphs = 5 for all points with error bars). Nymphs are significantly more likely to make a targeting error for strikes longer than 44ms (one-way anova: $p < 0.001$, pairwise Mann-Whitney U tests with Bonferroni correction: all $p < 0.01$).

Analysis of targeting errors provided insight into the sensory performance of the nymph. While dragonfly nymphs are reported to have foveal ommatidia Sherk (1978), our results do not clearly show evidence of a foveal region. However, there are regions in the field of view that have very few or no fish positions (Figure B.3C) suggesting that the location density of fish positions encountered may itself be a characterization of the foveal region. We do identify a specific region in the ventral portion of the field of view that is more likely to produce targeting errors (Figure B.3C-D).

Moreover, the increased likelihood of making a targeting error when in the posterior azimuthal and elevation quadrant with respect to the fish (Figure B.3E-F) suggests that looking at the tail of the fish was more likely to cause a targeting error. We speculate that this disadvantage of looking at the tail is due to the reduced view of the eyes of the larval fish which contain high concentrations of melanin Kelsh et al. (1996) and provide contrast. The probability of targeting errors also mapped to the mask motor volume since increased mask extension times were more likely to produce errors (Figure B.3G). However, nymphs were also less likely to strike where they were more likely to make an error (Figure B.3G) suggesting an internal model of sensorimotor coordination.

B.5. Neomycin treatment of larval zebrafish

We tested the role of flow sensing in fish escape responses by compromising the lateral line in a group of larvae by exposure to a 250 μmol solution of neomycin sulphate (Sigma Aldrich, St.Louis, MO) for a 30 min period, followed by a 3 h recovery prior to experiments. This technique was developed in previous studies Harris et al. (2003); McHenry et al. (2009), where it was shown to induce cell death in lateral line hair cells while leaving inner ear hair cells intact. After recovery, larval fish were monitored to ensure they performed spontaneous swimming behaviors and responded to touch stimuli delivered with a tungsten filament. These larvae were then introduced into the dish with the dragonfly nymph.

B.6. Approximating fluid velocity at the fish due to mask extension

To gain further insight into the role of the perturbed fluid in generating the escape response, we used a potential flow approximation to estimate the fluid velocity at the fish due to mask extension. Mask velocity alone was not a good proxy for the perturbed fluid flow at the fish position since it does not take into account the distance of the fish from the mask.

We started with an established analytical solution to the flow velocity field expressed in spherical coordinates around a sphere of radius a moving through an incompressible, inviscid fluid at a time dependent velocity $V(t)$ Fitzpatrick (2017).

$$v_r(r,\theta,t) = V(t)\frac{a^3}{r^3}cos\theta \tag{B.1}$$

$$v_\theta(r,\theta,t) = \frac{1}{2}V(t)\frac{a^3}{r^3}sin\theta \tag{B.2}$$

$$v^2 = v_r^2 + v_\theta^2 \tag{B.3}$$

Where v is the flow velocity expressed in terms of the radial and angular components—v_r and v_θ—for a position at some distance $r \geq a$ and angle θ from the sphere with respect to its velocity vector at some time t. We expect the flow pattern around the sphere to be axisymmetric around the velocity vector (i.e. independent of ϕ). In this set of equations, we can verify that when $r \to \infty$ then $v \to 0$, as we would expect. We used these equations with the velocity of the tracked mask as the value for $V(t)$ to estimate the flow velocity v at the fish which was some distance $r \geq a$ and angle θ. The value of a was set to 1.6 mm which approximated the radius of the mask (average diameter of 3.2 mm from all specimen).

We used this potential flow approximation to estimate the flow velocity at the fish over other methods, like computational fluid dynamics, due to its simplicity. Our intention was not to compute exact magnitudes of flow velocities but rather to have relative estimates for scenarios so we could investigate how higher and lower flow velocities may have influenced the fish escape response differently.

B.7. Predicting escape outcome with each parameter

To determine which parameter had the most influence on the fish escape outcome, we trained random forest classifiers using the native TreeBagger function within MATLAB on each of the following parameters to predict the binary outcome of escape failure (0) or success (1).

(1) Attack azimuth
(2) Attack elevation
(3) Mask extension time

(4) Bend duration

(5) Bend velocity

(6) Response latency

(7) Time remaining at escape

Ten different classifiers were trained for each parameter by pseudo-randomly selecting 85% of the dataset each time for training and testing accuracy with the remaining 15% of the dataset allowing for an estimate of the mean ± sem of accuracy for a classifier.

The parameter importance was computed with a flag within the native TreeBagger MATLAB function which calculates the out-of-bag estimates of variable importance by permuting the values of one of the variables to see how dramatically it changes the model predictions. For more information on the implementation and use of random forest classifiers, please refer to the MATLAB documentation for TreeBagger. Random forest classifiers were chosen over other classifiers due to their simplicity, their ability to perform non-linear classification while reducing variance through bagging/bootstrapping models and provide importance values for each predictor.

B.8. Larval zebrafish motor volume

During an escape response, larval zebrafish reorient with an initial bend with little or no movement of their center of mass and swim away with undulatory swimming during a propulsive stage Nair et al. (2015); Bhattacharyya et al. (2017). In this study, the fish motor volume was computationally generated to mimic this movement using a bend velocity (in $\frac{\circ}{\text{sec}}$) and a propulsive velocity (in $\frac{\text{mm}}{\text{ms}}$). The bend velocity was first used to compute the time needed for reorientation and then the propulsive velocity was used to compute the distance traveled. In this manner, the bend velocity and propulsive velocity together could define the positions in 3D space that the center of mass of the larval zebrafish could reach given a certain amount of time.

For all simulations of fish motor volumes, the propulsive velocity used was 0.12 $\frac{\text{mm}}{\text{ms}}$ which is supported by our own measurements and existing literature Dunn et al. (2016); Budick and O'Malley (2000). We assumed that the fish could reorient in any direction by changing pitch and yaw as necessary, which is supported by our own data (Figure 3.5E and H) and existing literature Nair et al. (2015). For Figures 3.7A and B, the fish motor volume was generated using the average bend velocity of 14 $\frac{\circ}{\text{sec}}$ found in this study.

For Figure 3.7C, fifty fish motor volumes were generated by pseudo-randomly sampling with replacement the initial bend velocities measured in this study (Figure 3.4K) for 6 increments of time remaining at escape (7, 15, 20, 25, 35, and 50 ms). These volumes were then used to compute the proportion not engulfed by the swept volume of the prehensile mask. The swept volume of the mask was represented by a hemi-ellipsoid (major axis: 3.2 mm and minor axis 2.8 mm) attached to the end of a half-cylinder (diameter: 3.2 mm and length: 6 mm, Figure 3.7B) whose dimensions were determined by measuring the prehensile masks of specimens in this study. To intersect the mask swept volume with the fish motor volume, the center of the hemi-ellipsoid of the mask swept volume was placed at the starting position of the fish motor volume. We simulated attacks from different directions with combinations of attack azimuths (front, side, and behind) and elevations (in-plane, above, and below) by moving the mask swept volume with respect to the fish motor volume. Ten thousand points were pseudo-randomly generated within the fish motor volume and the proportion of points not within the mask swept volume provided a measure of the proportion of the fish motor volume not engulfed. This was carried out for each fish motor volume for each increment of time remaining at escape to find the mean ± std proportion not engulfed for Figure 3.7C.

There seem to be some differences between the non-engulfed fraction of the motor volume and the measured proportion of successful escapes for small values of time remaining at escape below 10 ms (Figure 3.7C). This difference at small times remaining at escape may be because the propulsive velocity of fish is fastest at the beginning of the escape Danos and Lauder (2012); Dunn et al. (2016). However, we use a constant average propulsive velocity to generate the fish motor volume which may underestimate the size of the motor volume for small times remaining at escape.

Fish motor volumes representing Mauthner active and silent responses were generated by pseudo-randomly sampling different uniform distributions of initial bend velocities. The range of bend velocities for Mauthner silent motor volumes was $10 \pm 5 \ \frac{\circ}{\text{sec}}$ and Mauthner active motor volumes was $18 \pm 5 \ \frac{\circ}{\text{sec}}$. These ranges are supported by previous studies that investigate bend velocities of free swimming larval zebrafish before and after Mauthner ablation Liu and Fetcho (1999); Burgess and Granato (2007). The ranges were also constructed to have some overlap since studies have found that Mauthner active and silent responses can on occasion produce similar kinematics Kohashi and Oda (2008); Bhattacharyya et al. (2017). Furthermore, the initial bend velocities measured in this study (Figure 3.4K) are well described by the combination of these two ranges. Even though there is some evidence that Mauthner cell recruitment leads to faster propulsive velocities, the simulated propulsive velocity was not changed for Mauthner active motor volumes since this influence is not clear Nissanov et al. (1990); Eaton and Emberley (1991); Neki et al. (2014); Dunn et al. (2016). Intersections of the Mauthner active and silent motor volumes with the prehensile mask swept volume was carried out in the way described above.

The MATLAB code used to generate and visualize larval zebrafish motor volumes and the mask swept volume can be found in the GitHub repository associated with this study.

APPENDIX C

The consequences of visual acuity on the looming-evoked response

C.1. Fitting α with experimental data

The parameter α in Equation 4.2 determines when $\eta(t)$ reaches its maximum value. Notably, $\eta(t)$ reaches its maximum value at the same angular size regardless of the expansion rate $\frac{L}{V}$. We fit the parameter α such that $\eta(t)$ reached its maximum value corresponding the critical angular size of 35° for larval zebrafish looming-evoked responses Bhattacharyya et al. (2017).

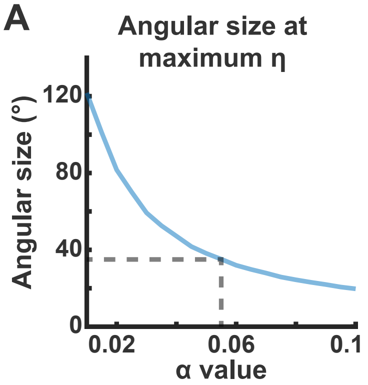

Figure C.1. Angular size at the maximum of $\eta(t)$.

Figure C.1 details: A) As α changes the angular size at the maximum of $\eta(t)$ as computed from Equation 4.2 changes. We chose the α that corresponded to the angular size of 35° (dashed lines).

As seen in Figure C.1, increasing values of α produce the maximum of $\eta(t)$ at at decreasing values of angular sizes. We chose an α value of 0.055 which corresponded to the angular size of 35° (dashed lines Figure C.1). While using a different value for α would change the angular size at maximum η, it would not change the general findings in this study.

C.2. Generating the noisy measured angular size

The sensory information available to the larval zebrafish about the angular size of the looming object was approximated by a sequence of noisy measurements of the true angular size. This sequence of measurements was created by sampling Equation 4.1 for each $\frac{L}{V}$ value at 25 Hz—every 0.04 seconds—to find the true angular size of the object at the time and then adding Gaussian noise with ±3.1°.

We tested the following looming rates: $\frac{L}{V} = 0.2$ s, $\frac{L}{V} = 0.4$ s, $\frac{L}{V} = 0.6$ s, $\frac{L}{V} = 0.8$ s, $\frac{L}{V} = 1.0$ s, $\frac{L}{V} = 1.2$ s. These rates fall within an ethologically relevant range Stewart et al. (2013); Dunn et al. (2016); Bhattacharyya et al. (2017). All simulated looming objects started out at 10° and stayed at the that size for 5 seconds before starting angular expansion at the specified rate. This was done to imitate similar experimental practices commonly followed in behavioral studies of the looming-evoked responses von Reyn et al. (2014); Bhattacharyya et al. (2017); Fotowat and Gabbiani (2007). Therefore, all generated sequences of noisy measured angular size in this study included an initial 5 seconds when the object was stationary and then expanded according the specified $\frac{L}{V}$ until it was less than 0.04 seconds from collision. This sequence of measurements was then used by the Kalman filter to estimate the angular size and expansion rate in real-time.

C.3. Basic design and specific implementation of the Kalman filter

The Kalman filter is a Bayes optimal recursive estimator for sequentially estimating the state of a linear Gaussian dynamical system Kovvali et al. (2013). The recursive algorithm of the Kalman filter has low computational complexity and memory requirements making it ideal for real-time applications of target and object tracking Bay (1991); Feder et al. (1999); Lebastard et al. (2012); Bar-Shalom et al. (2004). Moreover, Kalman filtering has found broad application in motor and computational neuroscience Wolpert and Ghahramani (2000); Wu et al. (2006); Schiff and Sauer (2008); Wilson and Finkel (2009). While a full derivation and review of the Kalman filter is outside the scope of this manuscript, here we present the basic design and our implementation of the Kalman filter for estimating angular size and expansion rate.

Consider the state evolution and measurement process of a linear and Gaussian dynamical system of the form

$$\begin{aligned} x_n &= F_n x_{n-1} + v_n \\ y_n &= H_n x_n + w_n \end{aligned} \tag{C.1}$$

The first line of Equation C.1 defines the state evolution where x_n is a D×1 dimensional vector representing the state of the system at time step n, F_n is the D×D state-transition matrix, x_{n-1} is the state of the system at the previous time step, and v_n is a D×1 Gaussian random state noise vector with zero mean and covariance Q_n. The second line defines the measurement process where y_n is a M×1 dimensional vector representing the current measurement, H_n is the M×D measurement matrix, and w_n is the M×1 Gaussian random measurement noise vector with zero mean and covariance matrix R_n.

Since the dynamical system is both linear and Gaussian, the conditional probability density functions (pdfs) of $p(x_n|x_{n-1})$ and $p(y_n|x_n)$ are given by Gaussian pdfs

$$\begin{aligned} p(x_n|x_{n-1}) &= N(x_n; F_n x_{n-1}, Q_n) \\ p(y_n|x_n) &= N(y_n; H_n x_n, R_n) \end{aligned} \tag{C.2}$$

Where $N(\cdot; m, P)$ denotes a Gaussian pdf with mean m and covariance P. Under these stated conditions, the posterior pdf of $p(x_n|Y_n)$ where Y_n is the set of all measurements up to the time step n can also be shown to be Gaussian, as represented below.

$$p(x_n|Y_n) = N(x_n; m_{n|n}, P_{n|n}) \tag{C.3}$$

In this notation, $m_{n|n}$ and $P_{n|n}$ denote the Gaussian posterior mean and covariance at time step n computed using measurements up to time step n. To explain the subscripts further, the notation of $m_{n|n-1}$ and $P_{n|n-1}$ would indicate the mean and covariance of the Gaussian pdf describing x_n computed with measurements up to time step $n-1$ and then predicted to time step n with the state evolution as described in Equation C.1.

Using this notation, the Kalman filter equations are given by Kovvali et al. (2013)

$$\begin{aligned} m_{n|n-1} &= F_n m_{n-1|n-1} \\ P_{n|n-1} &= F_n P_{n-1|n-1} F_n^T + Q_n \\ S_n &= H_n P_{n|n-1} H_n^T + R_n \\ K_n &= P_{n|n-1} H_n^T S_n^{-1} \\ m_{n|n} &= m_{n|n-1} + K_n (y_n - H_n m_{n|n-1}) \\ P_{n|n} &= P_{n|n-1} - K_n H_n P_{n|n-1} \end{aligned} \tag{C.4}$$

Here the first two lines of Equation C.4 compromise the prediction step and the last four lines compromise the update step. The Kalman filter equations must be computed for each time step to obtain new pdfs of the state variables.

To perform the computations above, we must specify values of $m_{0|0}$ and $P_{0|0}$ which are the mean and covariance describing the initial estimates of the state of the system before any measurements. Along with these initial estimates, we must define F_n, H_n, Q_n, and R_n which are constants parameterizing the system. Finally, with each iteration we will provide y_n which is the measurement at time step n. We used $m_{n|n}$ as our estimate for x_n which was a 2×1 vector containing the angular size and expansion rate as each element.

In this study, we were estimating angular size θ_n and expansion rate $\dot{\theta}_n$ from a measurement of angular size y_n. The relationship between the state variables can be linearly approximated by the following state evolution.

$$\begin{aligned} \theta_n &= \theta_{n-1} + \dot{\theta}_{n-1} + v_{n,1} \\ \dot{\theta}_n &= \dot{\theta}_{n-1} + v_{n,2} \end{aligned} \tag{C.5}$$

restated in matrix form

$$\begin{pmatrix} \theta_n \\ \dot{\theta}_n \end{pmatrix} = \begin{pmatrix} 1 & 1 \\ 0 & 1 \end{pmatrix} \begin{pmatrix} \theta_{n-1} \\ \dot{\theta}_{n-1} \end{pmatrix} + \begin{pmatrix} v_{n,1} \\ v_{n,2} \end{pmatrix} \tag{C.6}$$

In this situation, since we only have a measurement for angular size, the measurement process is of the following form

$$y_n = \begin{pmatrix} 1 & 0 \end{pmatrix} \begin{pmatrix} \theta_n \\ \dot{\theta}_n \end{pmatrix} + w_n \tag{C.7}$$

Therefore,

$$
\begin{aligned}
H_n &= \begin{pmatrix} 1 & 0 \end{pmatrix} \\
w_n &= N(0, R_n)
\end{aligned}
\tag{C.8}
$$

where R_n is the angular visual acuity squared (3.1^2) to represent the variance in measurement noise. However, it can be set to values 3–4× larger than this without changing the conclusions of this study. For the state evolution,

$$
\begin{aligned}
F_n &= \begin{pmatrix} 1 & 1 \\ 0 & 1 \end{pmatrix} \\
\begin{pmatrix} v_{n,1} \\ v_{n,2} \end{pmatrix} &= N\left(\begin{pmatrix} 0 \\ 0 \end{pmatrix}, Q_n \right)
\end{aligned}
\tag{C.9}
$$

For the dynamical system in Equation C.5, Q_n can be shown to be of the form Kovvali et al. (2013)

$$
Q_n = \sigma_\theta^2 \begin{pmatrix} \frac{1}{3} & \frac{1}{2} \\ \frac{1}{2} & 1 \end{pmatrix}
\tag{C.10}
$$

In Q_n, the term σ_θ^2 represents the variance of the process noise in angular size. After testing a range of values, we set this value at 0.008. An order of magnitude difference in either direction from this value did not change the general results of this study regarding the timing of maximum $\eta(t)$. However, setting this value beyond this range produced 1) very noisy estimates of angular size and expansion rate when the value was large or 2) very smooth estimates that poorly approximated the true angular size and expansion rate when the value was small.

Finally, we specified the values of the mean and covariance describing the initial estimates of the state of the system, $m_{0|0}$ and $P_{0|0}$. The initial estimate of the mean for both angular size and expansion rate were set to 0. The covariance matrix of the state was a diagonal matrix with large variances (10000) for both angular size and expansion rate to allow the system to take on any values once measurements were considered.

When producing smooth estimates, the Kalman-filtered expansion rate consistently underestimated the true expansion rate. This happened because the state evolution as defined by Equation C.5 assumes that the expansion rate—first time derivative of θ—persists through each time-step with some error $v_{n,2}$. However, the time-varying angular size of the looming stimulus as described by Equation 4.1 is infinitely differentiable with respect to time. This suggests that including higher-order derivatives in the state evolution would improve the estimate of the first derivative. However, it is unclear whether these higher-order derivatives are used by or represented in the nervous systems of animals for computations relevant to the looming stimulus. Therefore, they were excluded from the state evolution. Notably, the error term $v_{n,2}$ in Equation C.5 is used to represent some of the dynamics of the higher-order derivatives by allowing the expansion rate to change with each time-step. However, allowing this error-term to be large, as discussed earlier, produced highly unstable estimates of expansion rate. A complete discussion of this issue is outside the scope of this manuscript but has been covered in detail in other literature Liu et al. (2011a). Critically, for our purposes, $\eta(t)$ computed from the the Kalman-filtered estimates of $\theta(t)$ and $\dot{\theta}(t)$ still produced maxima near the maximum of the true $\eta(t)$ (Fig. 4.3).

The Kalman-filtered estimates of angular size and expansion rate were used to calculate $\eta(t)$ using Equation 4.2. Since the noisy measured angular size was created by adding zero-centered Gaussian noise to the true angular size, estimates of angular size and expansion rate were different for multiple simulations of the same looming rate. To create Figure 4.3B and D, the maximum value of $\eta(t)$ was identified during the looming stimulus and the distribution of times at maximum was fit using the default setting of a kernel density estimator native to Matlab called '*ksdensity*'.

C.4. The leaky-integrate-and-fire Mauthner cell model

The leaky-integrate-and-fire model of a neuron is parameterized by the current injection $I_e(t)$, the membrane voltage $V_m(t)$, the membrane time constant τ_m, the membrane capacitance C_m, and the membrane resistance R_m Burkitt (2006).

$$\begin{aligned} I_e(t) &= \tau_m \frac{dV_m(t)}{dt} + V_m(t) \\ \tau_m &= R_m C_m \end{aligned} \tag{C.11}$$

The differential equation defined in Equation C.11 can be solved numerically in discrete time for membrane voltage where $I_e(t)$ is the time-varying current injection into the model Burkitt (2006).

$$V_m(t+1) = V_m(t) + \frac{\Delta t}{\tau_m}(-(V_m(t) - V_e) + I_e(t)R_m) \tag{C.12}$$

In Equation C.12, t is now discrete and represents the immediate time step, $V_m(t)$ and $I_e(t)$ represent the membrane voltage and current input at the immediate time step while $V_m(t+1)$ represents the membrane voltage at the next time step. The constants Δt and V_e represent the time step size and the resting membrane voltage, respectively. In our implementation of this solution, when $V_m(t)$ reaches a value above a threshold voltage V_{th}, it is set to a spike voltage V_s and $V_m(t+1)$ is not solved for with the equation but rather set to a reset voltage V_r. Since a single Mauthner cell (M-cell) spike produces the escape response,

Constant	Value
τ_m	23 ms
R_m	10 MOhms
V_e	-75 mV
V_{th}	-61 mV
V_r	-79 mV
V_s	20 mV
Δt	0.5 ms

we were only concerned about the timing of the first spike when providing the time-varying current injection.

The values for the membrane time constant τ_m, the membrane resistance R_m, the resting membrane voltage V_e, the threshold voltage V_{th}, and the reset voltage V_r were all chosen from an established leaky-integrate-and-fire model of the M-cell Koyama et al. (2016). The remainder of the constants which include the time step size Δt and the spike voltage V_s were chosen so the model produced reasonable results. The values of all constants are provided in the table.

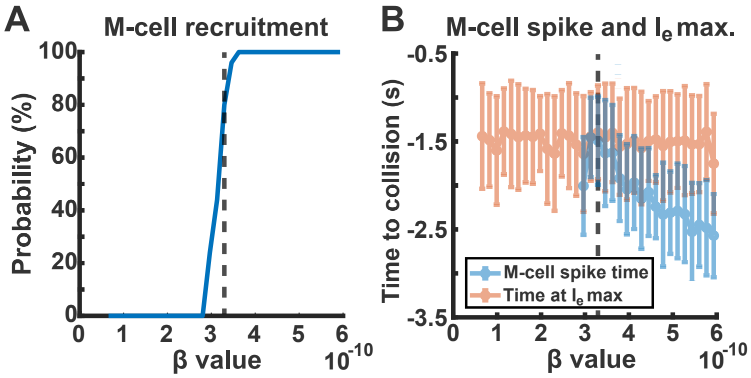

Figure C.2. M-cell recruitment for $\frac{L}{V} = 0.8$ s varies with β.

Figure C.2 details: A) As the value of β in Equation 4.3 is changed, the probability of recruiting the M-cell for $\frac{L}{V} = 0.8$ s changes. Dashed vertical line marks the β value 3.18×10^{-10} chosen for simulations.

B) As the value of β is changed, the correspondence of the time of the first M-cell spike and the time at maximum I_e changes.

We multiplied $\eta(t)$ by a constant β to provide the time-varying current injection $I_e(t)$ into the neuron model (Eq. 4.3). This constant had to be much smaller than 1 since the values of η ranged from 2–6 (Fig. 4.3) while the current injection values needed to be on the order of 10^{-9} Amperes. The β value we used was 3.18×10^{-10}. To determine this constant, we first interpolated $\eta(t)$ so it was resolved at the time step size (0.5 ms) needed for the numerical solution (Eq. C.12). Then we tested a range of values for β to see how M-cell recruitment varied for $\frac{L}{V} = 0.8$ s.

We found that values of β that were smaller than 3.18×10^{-10} did not recruit the M-cell at all and values that were larger recruited the M-cell with 100% likelihood for $\frac{L}{V} = 0.8$ s (Fig. C.2A). Furthermore, we chose the value of β for which the time of the first M-cell spike and the time of maximum I_e coincided (Fig. C.2B). Values of β that were larger recruited the M-cell soon after the onset of the current injection and before it reached its maximum value. This would produce many M-cell spikes through the duration of the looming stimulus which is not encountered experimentally. Critically, the β value of 3.18×10^{-10} that we chose also reproduced the experimentally observed timing of M-cell spikes for $\frac{L}{V} = 0.4$ s and $\frac{L}{V} = 1.0$ s.

C.5. Finding the boundary between M-cell active and silent cases

The linear boundary between M-cell active and silent cases seen in Figure 4.5F was found using a native Matlab function called '*fitcdiscr*' which fits a discriminant analysis classifier to data with binary labels. In our case, the data labels were M-cell active or M-cell silent and the data points had two attributes: I_e max. and Time at I_e max. We fit this boundary to determine if the time of maximum I_e and the value of maximum I_e interacted to produce M-cell active and M-cell silent cases or if one attribute was far more determinative of M-cell activity than the other.

We chose a linear boundary over other more complex boundaries since it's easier to interpret the linear result. We also used 10-fold cross-validation to verify that higher-order polynomial boundaries (second thru fifth order) were not significantly more accurate in classifying M-cell active versus M-cell silent cases than the linear boundary.

The equation of the linear boundary in Figure 4.5F is:

I_e max. $= -0.023\frac{\text{nA}}{\text{sec}}\times$Time at I_e max. + 1.4 nA